IMPROVED CONTROL STRATEGIES

FOR DROOP-CONTROLLED

INVERTER-BASED MICROGRID

Submitted by Walid R. M. Issa to the University of Exeter

as a thesis for the degree of

Doctor of Philosophy in Renewable Energy by Research

in March 2015

I certify that all material in this thesis which is not my own work has been identified and that no material has previously been submitted and approved for the award of a degree by this or any other University.

Signature: ……..

Abstract

The main focus of this PhD thesis is fundamental investigations into control techniques of inverter-based microgrids. It aims to develop new and improved control techniques to enhance performance and reliability. It focuses on the modelling, stability analysis and control design of parallel inverters in a microgrid.

In inverter-based microgrids, the paralleled inverters need to work in both grid-connected mode and stand-alone mode and should be able to transfer seamlessly between the two modes. In grid-connected mode, the inverters control the amount of power injected into the grid. In stand-alone mode, however, the inverters control the island voltage while the output power is dictated by the load. This can be achieved using droop control. Inverters can have different power set-points during grid-connected mode but in stand-alone mode they all need their power set-points to be adjusted according to their power ratings. However, during sudden unintentional islanding (due to loss of mains), transient power can flow from inverters with high power set-points to inverters with low power set-points, which can raise the DC link voltage of the inverters causing them to shut down. This thesis investigates the transient circulating power between paralleled inverters during unintentional islanding and proposes a controller to limit it. The controller monitors the DC link voltage and adjusts the power set-point in proportion to the rise in the voltage. A small signal model of an island microgrid has been developed and used to design the controller. The model and the controller design have been validated by simulation and practical experimentation. The results confirmed the

performance of the proposed controller for limiting the DC link voltage and supporting a seamless mode transfer.

The limitation of the droop controller, that is utilized to achieve load sharing between parallel-operated inverters in island mode, has also been addressed. Unequal output impedances among the distribution generation (DG) units lead to the droop control being inaccurate, particularly in terms of reactive power sharing. Many methods reported in the literature adopt low speed communications to achieve efficient sharing. However, the loss of this communication could lead to inaccuracy or even instability. An improved reactive power-sharing controller is proposed in this thesis. It uses the voltage at the point of common coupling (PCC) to estimate the inductance value of the output impedance including the impedance of the interconnecting power cables and to readjust the voltage droop controller gain accordingly.

In an island microgrid consisting of parallel-connected inverters, the interaction between an inverter's output impedance (dominated by the inverter's filter and voltage controller) and the impedance of the distribution network (dominated by the other paralleled inverters' output impedances and the interconnecting power cables) might lead to instability. This thesis studies this phenomenon using root locus analysis. A controller based on the second derivative of the output capacitor voltage is proposed to enhance the stability of the system. Matlab simulation results are presented to confirm the validity of the theoretical analysis and the robustness of the proposed controller.

A laboratory-scale microgrid consisting of two inverters and local load has been built for the experimental phase of the research work. A controller for a voltage source inverter is designed and implemented. A dSPACE unit has been used to

realize the controller and monitor the system in real time with the aid of a host computer. Experimental results of the two voltage source inverters outputs are presented.

Table of Contents

List of Figures

List of Tables

ACKNOWLEDGEMENTS

First and foremost, I would like to express my thanks to my parents, who have been a constant source of support, help and guidance through everything I have done. A special acknowledgement must also go to my family for being so supportive and encouraging throughout my studies.

I would also like to thank Exeter University, as without their funding this work would not have been carried out.

I would like to take this opportunity to express my sincere gratitude to my supervisor, Dr. Mohammad Abusara, for his guidance, advice and determination in giving valuable information and support throughout this research.

I would also send my thanks to Prof. Suleiman Sharkh from University of Southampton for his support and worthy feedback on each part of my work.

The support of the staff in renewable energy laboratory, Ian Faulks, in helping with the construction of the equipment enclosure, PCB board and electrical wiring, etc. is also greatly appreciated.

CHAPTER 1 INTRODUCTION

1.1. Microgrid: A new concept

The interest in distributed generation (DG) systems is rapidly increasing because larger power plants are becoming less feasible in many regions due to increasing fuel costs and stricter environmental regulations. In addition, recent technological advances in small generators, power electronics, and energy storage devices have provided a new opportunity for distributed energy resources at the distribution level. Traditional centralized power generation systems have many drawbacks: firstly, power generation plants depend heavily on fossil fuel, which increases CO_2 emission and the rejected heat is wasted; secondly, a large amount of power is produced in one place and delivered using expensive transformers and transmission lines; thirdly, transmission lines and transformers create the well-known problems of power losses and voltage drop; fourthly, traditional centralized power generation does not provide an economically feasible solution to supply power to poor and isolated communities.

DG based on renewable energy sources (such as solar, wind and tidal) integration contributes to reducing CO_2 emissions from fossil fuel based sources, reducing transmission losses, mitigating voltage variation, relieving peak loading, and enhancing supply reliability. However, an increased penetration of DG sources, particularly in the distribution network, may cause problems such as voltage rise, unstable voltage and frequency and protection

miss-coordination [1]-[4]. Such problems can be mitigated by aggregating a number of DG sources and loads into one controlled unit called a microgrid as shown in Figure 1.1. A microgrid has many advantages, such as increased reliability, more controllability, and better power quality. Like a traditional power grid, smart microgrids generate, distribute and regulate the flow of electricity to consumers, but do this locally. It can be seen as a modern, small-scale version of the centralized power generation system.

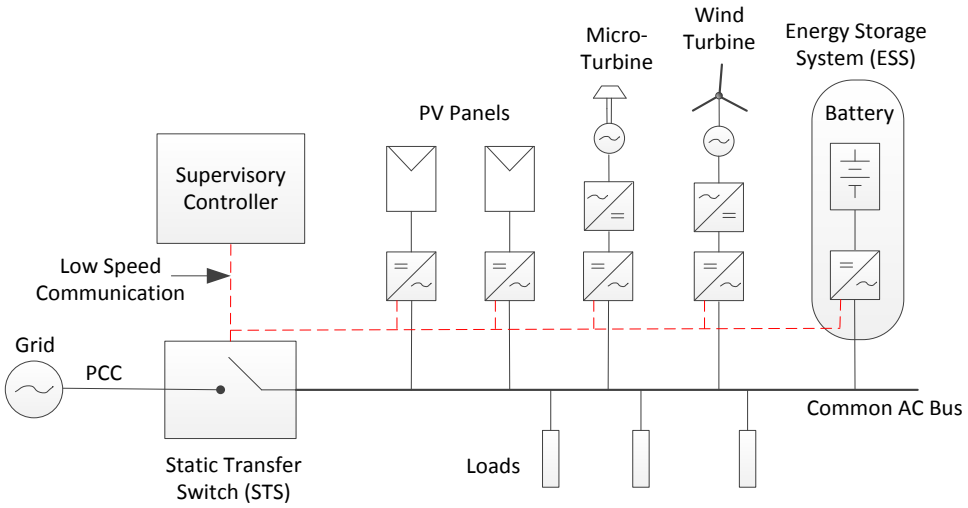

Figure 1.1 Microgrid structure of multi parallel DC/AC converters supplied by renewable energy sources [5]

A microgrid consists of DG sources such as Photovoltaic (PV) panels, wind turbines, gas micro-turbines, and storage systems such as batteries. These DG sources cannot be readily interfaced to the grid being DC (PV and batteries) or variable AC frequency (wind turbines and gas micro-turbines). Therefore, power electronic converters are required to interface the DG sources to the grid. The grid interface DC/AC power electronic inverters are paralleled together to form one AC bus which is connected to the grid via a Static Transfer Switch (STS). Local loads can be connected to the microgrid side of the STS. The microgrid

has two modes of operation: grid-connected mode and island mode. In grid-connected mode, the DC/AC inverters are connected in parallel with the grid and hence the output frequency and voltage are fixed by the stiff grid. In this mode, inverters can export power to the grid. If the STS opens, the microgrid operates in island mode. In this mode, the output voltage and frequency are controlled by the DC/AC inverters and the local load is supplied by the paralleled inverters which share the load equitably i.e., each unit shares power according to its rating. The microgrid can transfer from grid-connected mode to island mode. There are two kinds of islanding: intentional and unintentional. Intentional islanding happens due to a pre-planned decision and the STS opens at a predefined moment. Normally all precautions will be taken to make this intentional transition from grid-connected mode to island mode as smooth as possible. Unintentional islanding, however, can occur at any time, because of a sudden fault in the utility grid. This type of islanding might cause undesirable transients. The microgrid can also transfer from island mode to grid-connected mode. The STS senses the voltages at both of its terminals and only closes when these voltages are synchronised.

The DC/AC inverter is a critical part of any power-electronic based microgrid consisting of high switching frequency solid-state devices and a low pass filter as shown in Figure 1.2. The input of the inverter is DC, which is produced across the DC link capacitor, while the output is AC generated on the output of the inverter. The switching devices, i.e. IGBT (Insulated gate bipolar transistor), receive control signals from a voltage controller. The latter produces pulse width modulation (PWM) signals correlated to the reference voltage signal. The AC output of the switching devices contains many harmonic signals resulting from

switching. As a consequence, a filter, i.e. LCL filter, is used to attenuate these harmonics and produce a sine wave power signal.

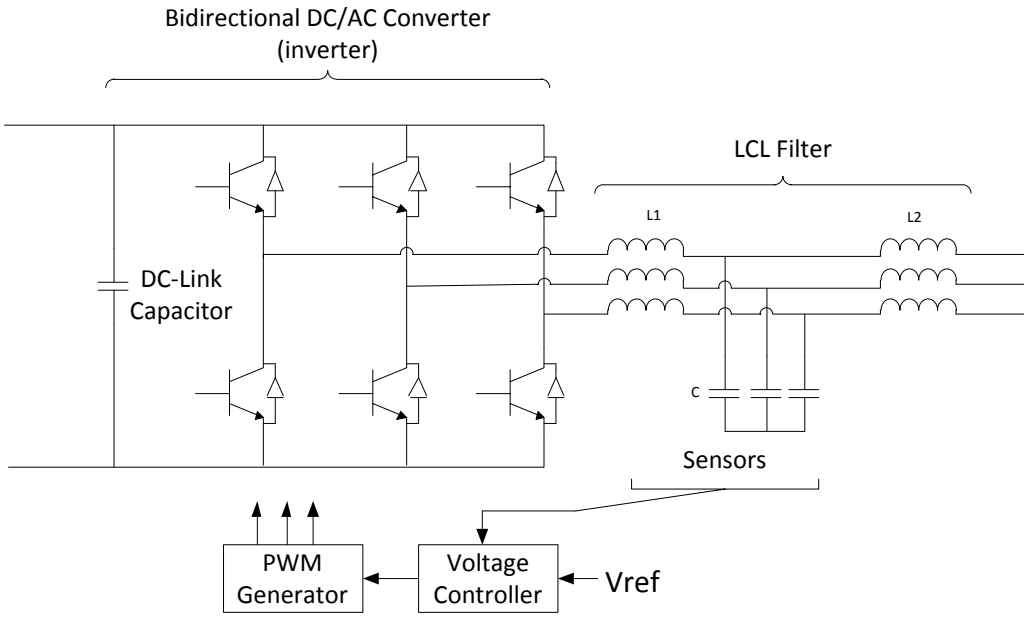

Figure 1.2 Inverter structure containing six IGBTs with LCL filter

The main focus of this thesis is to develop control strategies for droop-based inverters forming a microgrid in both island and grid-connected modes. The control system should provide high reliability, robustness and stability against all conditions of loads and network structure. Furthermore, it has to support a seamless transfer between the microgrid modes without interrupting the operation of any unit. The accuracy of power sharing between parallel inverters is also important. Therefore, the main aim of this thesis is to study the effect of unintentional islanding on the power sharing between parallel inverters. This could lead to an unreliable microgrid system and undesirable circulating power flow. This issue has not been addressed before in the literature. In addition, an analytical model for the mode transition of a microgrid has not been well-defined. Accurate active power sharing can easily be achieved using droop

control because the system frequency can be considered as a virtual communication link between the inverters. However, reactive power sharing in island mode depends on the output voltages which could vary from one point to another depending on the impedance of the interconnecting cables and the location of each inverter. Previous work showed that a communication link between the inverter and a supervisory controller can play an important role in maintaining accurate reactive power sharing by sensing some voltage nodes. However, a loss of this communication might lead to instability. The literature has addressed the impact of long cables between island inverters as well as the output impedance interaction with the rest of the microgrid network impedances and showed that this might create a resonance and cause instability. However, more work is still needed to propose robust controllers against cable impedances.

1.2. Aims and Objectives

This thesis is mainly concerned with fundamental investigations into control techniques of droop-controlled inverter-based island microgrids. The thesis presents a mathematical model of a microgrid and investigates transient response during unintentional islanding. Additionally, the thesis presents an investigation into reactive power sharing between inverters. Furthermore, the impedance interaction between the inverters and the distribution network on system stability is studied.

The objectives of the thesis are summarized as follows:

- To review various techniques used to control parallel inverters in a microgrid.

- To produce a model-based island microgrid to study and analyse the system responses and proposed controllers performance.
- To study the effect of unintentional islanding on circulating power between inverters using small signal mathematical modelling and computer simulation tools.
- To design a controller to limit circulating power during unintentional islanding and prevent the inverters from tripping.
- To design a controller for improved reactive power sharing between islanded inverters.
- To study the interaction between an inverter's output impedance and the impedance of the distribution network on system stability and to propose a controller to enhance the system stability.
- To build an experimental microgrid setup in the laboratory consisting of two parallel inverters to validate the mathematical modelling, computer simulation and the designed controllers.

1.3. Novel Contributions of the thesis

The contributions of the thesis are summarised as follows:

- Development of a small signal mathematical model of an island microgrid consisting of two parallel inverters that is used to investigate the transient response during unintentional islanding. The investigations have shown that different power set-points during grid-connected mode could lead to large circulating power between inverters if the grid was lost. This circulating power causes the DC link voltage to rise and, consequently, the inverter to trip.

- Validating the small signal model by the results obtained from Matlab/Simulink model and the practical model. This presents a design tool to select the parameters of a proposed controller and expects the behaviour of the states.
- Design of a novel controller that limits the circulating power by monitoring the DC link voltage and adjusts the power set-point in proportion to the rise in the voltage, which eventually supports a seamless transfer operation and increases the microgrid system reliability.
- Extending the model for a multi-inverter island microgrid. The model includes many inverters, loads and distribution lines. In addition, the states of the DC link voltages are incorporated to study and propose a new controller for more enhanced responses in limiting the DC link rise. This is also validated by Matlab/Simulink simulation.
- Design of a novel controller that enhances the reactive power sharing between parallel-connected inverters. This controller reduces the dependency on the communication and the risk of system instability if this communication link was lost.
- Investigations into the effect of the inductive virtual impedance and the network cables length on the stability of parallel-connected inverters. In addition, a study on the interaction between the inverter's output impedance with the rest of the network is developed. A controller based on the second derivative of the output capacitor voltage is proposed to enhance the stability of the system.

1.4. Published Papers

The outcomes of the research have been published in journals and conferences as follows, and attached in the Appendix.

1. *Issa, W.; Abusara, M.; Sharkh, S., "Control of Transient Power during Unintentional Islanding of Microgrids," IEEE Transactions on Power Electronics, vol.PP, no.99, pp.1,1*
2. *Issa, W.R.; Abusara, A.; Sharkh, S.M., "Impedance interaction between islanded parallel voltage source inverters and the distribution network," Machines and Drives (PEMD 2014), 7th IET International Conference on Power Electronics, vol., no., pp.1,6, 8-10 April 2014*
3. *Issa, W.; Abusara, M.; Sharkh, S.; Mallick Tapas, "*A small signal model of an inverter-based microgrid including DC link voltages,*" 17th European Conference on Power Electronics and Applications, EPE 2015, Geneva, Switzerland, 8-10 Sep 2015*

and a submitted paper,

4. *Issa, W.; Abusara, M.; Sharkh, S., "*Improved reactive power sharing for parallel-operated inverters in island mode,*" Journal of Power Electronics.*

1.5. Organisation of the Thesis

The thesis is organised as follows:

Chapter 2 presents a review of the literature on power sharing techniques, especially droop control. In addition, another concern about reactive power sharing and stability studies is presented. Chapter 3 introduces the practical

setup which is a small scale microgrid. Chapter 4 discusses the issue of the circulating power in an unintentional islanded microgrid. A modelling, stability locus and proposed solution are presented in this chapter. Chapter 5 illustrates the reactive power sharing inaccuracy and proposes a new controller to improve it in island mode. Chapter 6 studies the stability of islanded inverters when they are connected by long cables. Furthermore, a controller is proposed to increase the stability against such effects. Chapter 7 gives an overview of the future work and the research outcomes.

CHAPTER 2 CONTROL TECHNIQUES FOR INVERTER-BASED MICROGRID

2.1. Introduction

The fact that a microgrid includes many DG units that are able to work in both modes (grid-connected and island mode) raises many issues that could create technical challenges, particularly, during the transfer between the two modes. It is worth mentioning that DG includes synchronous generators as well but this thesis is concerned with inverter-based microgrid. In this chapter, the literature is reviewed to highlight the main challenges facing the development of microgrids and the recent related research outcome. The thesis concentrates on control strategies, particularly in island mode, in terms of voltage controllers, load sharing, modelling and stability issues.

Figure 2.1 illustrates a single-line diagram of a microgrid that includes a Photovoltaic (PV) system, wind turbine and a battery energy storage unit. The inverters have an interface with the point of common coupling (PCC) bus through power-electronic converters and cables. The microgrid is connected to the utility grid through a static transfer switch (STS) that can be monitored and controlled by the microgrid central controller (MGCC) and could alternatively be called a supervisory controller. The latter also sends all DG configurations and set-points of voltage, frequency and power through a low-bandwidth communication link. In addition, it has the ability to give the decision of mode transfer from grid-connected to island operation and vice-versa. Each unit's

controller has nested control loops that together guarantee the stability and accurate control of active and reactive power in both modes. It is worth mentioning here that the DC sources in all DGs are assumed to have a stable and regulated output, ready to be used by the DC/AC converters. The control of the DC sources will not be discussed in this thesis.

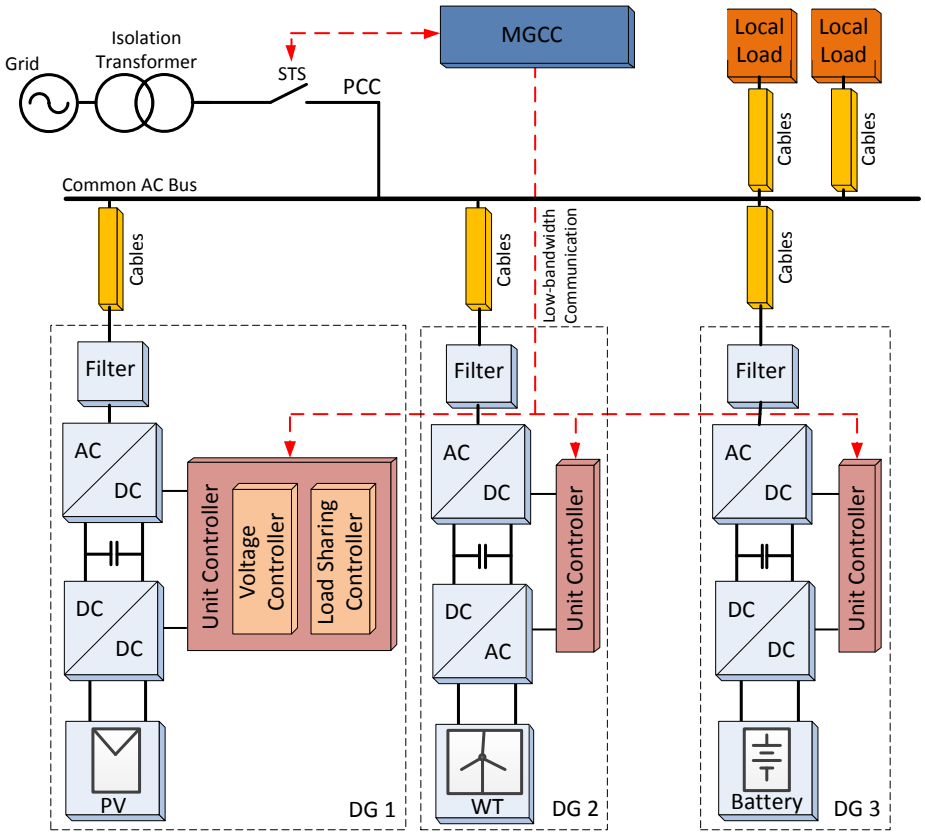

Figure 2.1 Microgrid control structure includes renewable energy sources with its DC/DC, AC/DC and DC/AC converters

2.2. Droop Control

The basic control objective in a microgrid operating in island mode is to achieve accurate power sharing while maintaining close regulation of the microgrid

voltage magnitude and frequency. Two control approaches can be followed to realize the abovementioned objectives:

1. Communication-based control (wired methods) such as master–slave control (MSC) system [6], [7]. These control schemes use high speed communications between inverters to achieve accurate power sharing by making one inverter take the master role of voltage control inverter (VCI) to control the frequency and voltage of the microgrid while the other inverters operate as current controlled inverters (CCI) as shown in Figure 2.2. The main disadvantages of this system are the dependence on high-speed communications which is costly and decreases the system reliability and expandability. Moreover, it does not provide seamless mode transition from grid-connected mode to island mode and vice-versa. During transition, the voltage across the load can become very low or very high [8].

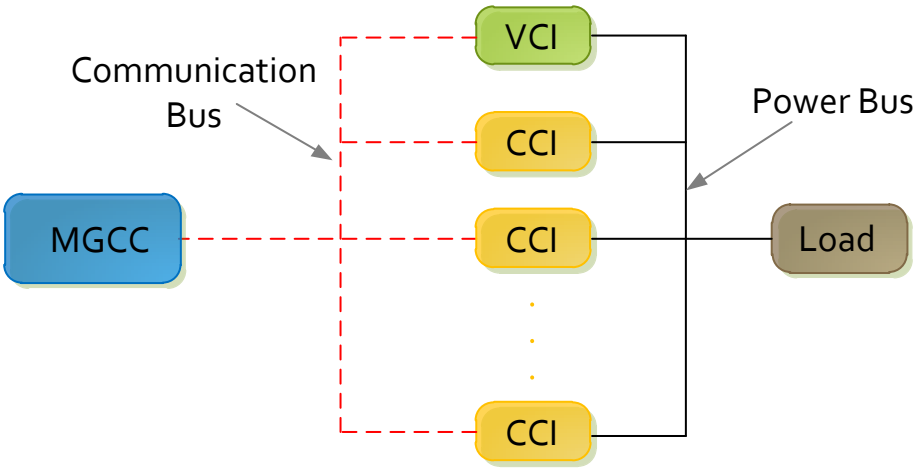

Figure 2.2 Master- Slave Control System

2. Non-communication-based control (wireless methods) that relies on droop control [9]-[11]. The name wireless comes up as this method does

not need communications between the inverters. The thesis will be concerned with this method.

2.2.1. Droop Control Concept

Wireless parallel structure relies on the ability of the inverter unit to regulate the output voltage and frequency while sharing the active and reactive power demands. A key for wireless technique is to use droop control [12], [13], [14], which is widely used in conventional power generation systems. The advantage is that no external communication mechanism is needed among the inverters. However, communication can still be used between each unit and a supervisory central controller, e.g. MGCC, for monitoring and management issues. This enables good sharing of linear and/or nonlinear loads. In addition, its ease of implementation, based merely on local voltage and current information, enables plug-and-play operation. Thus, it increases redundancy and simplicity of system expansion.

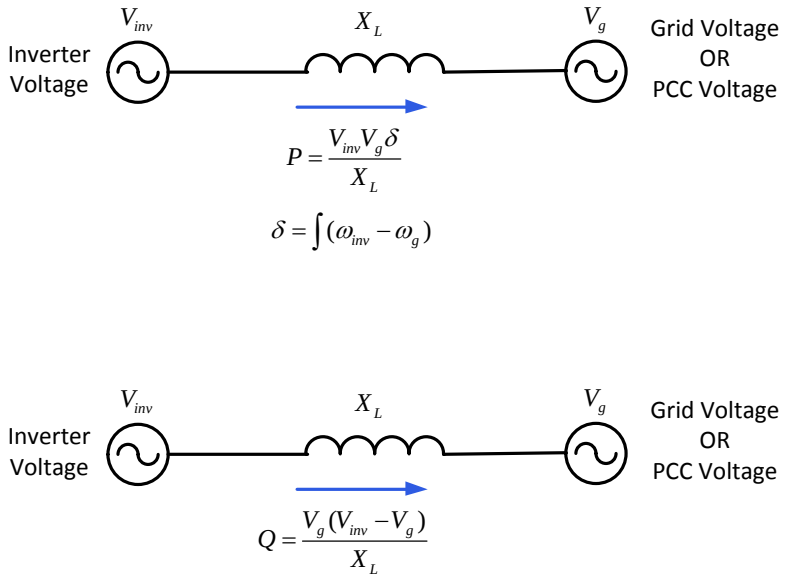

Figure 2.3 Power flow control between two voltage sources nodes

The droop control replaces the need of communication in particular in island mode. In grid-connected mode the control of power generated to the grid can be easily implemented using droop control or other controllers. However, the strength of droop control appears in island mode, when all units need to share power according to its rating without the need to communicate to other units. This supports the seamless transfer between the microgrid modes. Figure 2.3 illustrates the power system flow between two voltage sources separated by an inductor and how the active power can be controlled by the phase angle between the voltage signals of each source and the reactive power by changing the amplitude difference between these sources. In practical scenarios, the output impedance can't be purely inductive as a resistive value might affect its performance.

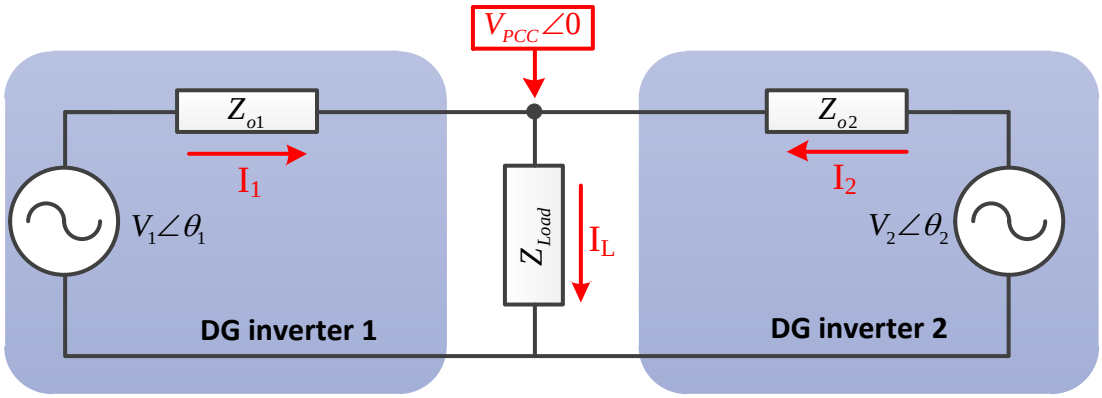

Figure 2.4 Two islanded inverters connected to a load

To make the droop control concept clearer, Figure 2.4 shows two inverters connected in parallel and supplying common load. Each inverter is connected via output impedance to the load bus. The active and reactive power that is

exported from each inverter is subject to one of two forms according to the kind of output impedance.

The output impedance can be dominantly inductive or resistive and this determines how the inverter would control the exported power. When the inverter's output impedance is pure inductive, the generated active power (*P*) depends on the phase difference (θ) between each inverter output voltage (*V)* and the PCC voltage (V_{PCC}) while the reactive power depends on the magnitude difference between the voltages (V-V_{PCC}). The situation is inverted if the system impedance is pure resistive as shown in Table 2.1.

System Impedance	Pure Inductive $\boldsymbol{Z_o = jX}$	Pure Resistive $\boldsymbol{Z_o = R}$
Active Power	$P \cong \frac{V_{PCC}\, V\, \theta}{Z_o}$	$P \cong \frac{V(V - V_{PCC})}{Z_o}$
Reactive Power	$Q \cong \frac{V(V - V_{PCC})}{Z_o}$	$Q \cong \frac{-V_{PCC}\, V\, \theta}{Z_o}$

Table 2.1 Active and reactive power of parallel inverters

The natural form for the output impedance is the inductive case. This is valid in three-phase lines that are mainly inductive and in single phase line when an extra grid inductor is adopted [15]. Thus, the active power will be controlled according to the phase angle while the reactive power will be controlled by the voltage difference as explained earlier. Figure 2.5 shows the relationship between *P*-ω and *Q*-*V*.

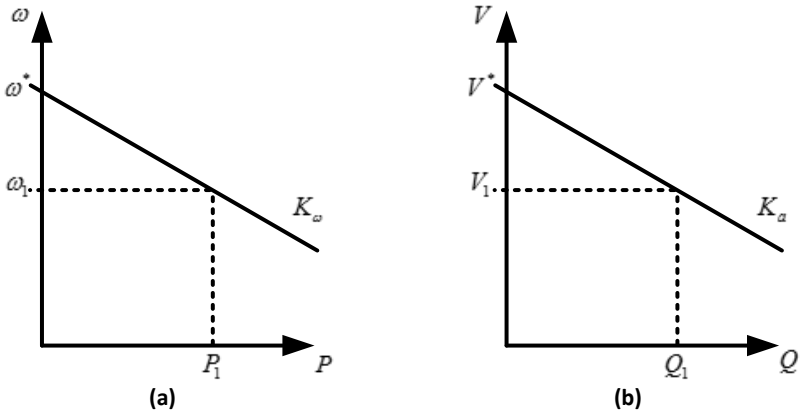

Figure 2.5 P-ω and Q-V droop control curves

The role of the droop control here is to govern the output power to make eventually a good power sharing between inverters in the case of islanding and accurate controlling of the injected power to the grid in the case of grid-connected mode.

For each case (grid-connected, island modes) the droop control equations are as follow,

In island mode,

$$\omega = \omega^* - K_\omega P \quad (1)$$

$$V = V^* - K_a Q \quad (2)$$

where K_ω, K_a are the droop coefficients and ω^*, V^* are the frequency and voltage at no load and P, Q are the measured active and reactive output powers, respectively.

In grid-connected mode,

$$\omega = \omega^* - K_\omega (P - P^*) \quad (3)$$

$$V = V^* - K_a(Q - Q^*) \quad (4)$$

where P^*, Q^* are the set-points of the required exported active and reactive power, respectively, and these settings are sent by the MGCC.

Active (P) and reactive (Q) power can be measured and averaged over one cycle of the fundamental frequency, so that the powers are evaluated at the fundamental frequency. This operation can be realized by means of low-pass filters (LPF) with a reduced bandwidth [16]. Figure 2.6 shows the block diagram of droop controller with measurement filters.

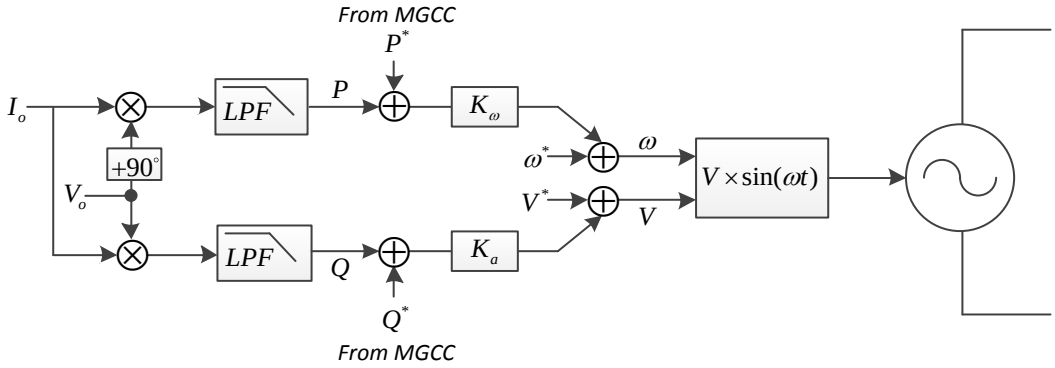

Figure 2.6 Diagram of droop control

Line Type	***R(Ω/Km)***	***X(Ω/Km)***	***R/X***
Low voltage line	0.642	0.083	7.7
Medium voltage line	0.161	0.19	0.85
High voltage line	0.06	0.191	0.31

Table 2.2 Typical line impedance values

2.2.2. Droop control limitations

Although the droop control introduces an intelligent automated method to control the power sharing/injection without communications between the inverters, its drawbacks limit its applications [17, 18]. The drawbacks include:

1. It has an inherent trade-off between load sharing accuracy and voltage regulation as it introduces frequency and voltage variations proportional to the active and reactive output power.
2. The dynamics of the power sharing does not only depend on the droop control coefficients but also on the method of power calculation as using the low pass filters creates new limits.
3. A restoration operation is needed before returning to grid-connected mode because of the drop in frequency and voltage caused by droop control, which reduces the seamless mode transfer.
4. Droop control uses an assumption of pure inductive or pure resistive output impedance which is practically not very accurate. The output impedance could be a combination of both as complex impedance. This weakens the decoupling between the active and reactive power control loops because each pure form of the output impedance gives another form of droop control as stated in equations (1) to (4) and a combination of the two forms makes, for instance, any change in the frequency leads to a change in both active and reactive output powers. This is related also to the nature of the distribution network as shown in Table 2.2 [19].
5. Droop Control is not effective when the units supplies non-linear loads because it does not support the harmonic signals sharing.

2.2.3. Enhancements on the droop control

The importance of the droop control in microgrids led many researchers to work toward enhancing it and introducing different solutions for the problems caused by its limitations. In what follow, the main research work on droop control will be reviewed.

A) Load Sharing:

This can be categorized into three points as,

1. **Dynamics of power sharing**:

   Many publications [20],[21],[22],[23] proposed solutions to enhance the transient responses of active and reactive power sharing in grid-connected mode and island mode. Guerrero et al. [16] proposed a PID controller instead of just a proportional controller to improve the dynamic response. For the same purpose, Avelar et al. [24] proposed an extra phase loop to mitigate the response transient peak and minimize the circulating currents between inverters.

2. **Power calculation**:

   The low pass filter is used commonly in many works [25],[24],[26],[27]. However, the slow response of it affects the overall transient of the power sharing and circulating currents, particularly, in island mode. Alternative methods are proposed in [8], [28] that have better dynamics, fast response and smaller ripple. In addition, a comparison of many methods is investigated in [29].

3. **Accuracy of load sharing**:

In grid-connected mode, the power control accuracy is achieved by the advantages of a PI controller [8],[30] that eliminates the steady state error of active and reactive power. However, this is difficult to implement in island microgrid. The difficulty is generated by the tradeoff between the accuracy of load sharing and the voltage/frequency regulation. If the droop gains are increased to obtain more accurate load sharing, this would degrade the regulation and may destabilize the system. Kang et al. [31] proposed a droop control with two droop coefficients to maintain the stability in island mode during low and high loads. Wei Yao et al. [32] adopted a new droop control that makes the droop relation to be nonlinear between P-ω and Q-V to decrease the drop of frequency and voltage during supplying heavy loads. In addition, an adaptive droop behaviour against small and large loads steps is proposed in [33]. A supplementary loop was proposed [22] to stabilize the system despite having high gains that are required for better load sharing. A decoupled control of virtual real and reactive power through frame transformation is proposed in [34]. Other authors introduced many solutions as in [35] which used second order generalized Integrator (SOGI), that generates the filtered in-phase and quadrature-phase versions of the grid voltage/current, to estimate the grid impedance to substitute it in the droop control and strength the decoupling between active and reactive power.

B) **Frequency and voltage regulation**:

In island mode, the PCC frequency and voltage do not match the set-points of the microgrid. Thus, a restoration and regulation process is required if the microgrid will be reconnected to the grid again. A secondary loop is proposed in [17],[36] adopting a PI controller to restore the required values. In [37],[38] a phase droop control is used that makes the frequency independent of the load so it is fixed over the time. In addition, authors in [39] allow the operator to tune the real power sharing controller without compromising frequency regulation by adding an integral gain into the real power control.

C) **Output impedance**:

Output impedance is quite essential for proper droop control. However, as mentioned earlier, the uncertainty of being pure inductive or resistive or in between has a negative impact on P and Q control decoupling.

1. Virtual output impedance:

The concept of the virtual impedance has been widely used to overcome the problem of power coupling caused by high R/X ratio in low voltage distribution networks [8, 40]. It increases the inductive reactance/resistance of the inverter's output impedance without using additional physical inductors/resistors that would increase size and cost. Thus, it mitigates the effect of the network and line impedances on the droop control. The literature illustrates the recent researches toward developing the virtual output impedance concept. A parallel-connected

virtual resistive impedance control method is proposed in [41] for current sharing in island mode. This gives the advantages of more damped system, in terms of resonance, and automatic harmonic sharing. In [16] an inductive virtual impedance is used. However, a concern for the virtual inductor control scheme is the inductor voltage drop calculation, which involves the differentiation of the line current. Differentiation can cause high frequency noise amplification, which in turn may destabilize the inverter voltage control scheme especially during transient. A common approach to avoid noise amplification is to replace the differentiator with a high-pass filter (HPF) to attenuate the high-frequency gain of the resulting transfer function as in [42]. The virtual impedance also supports the soft-start operation [27] by maintaining a high impedance at the beginning then reducing it to a nominal value at steady state, which minimizes the circulating current between the inverters.

2. **Sharing of current harmonics**:

Especially during supplying non-linear loads in island mode, to cope with the nonlinear load sharing, in [27], a method was proposed to share nonlinear loads by adjusting the output voltage bandwidth with the delivered harmonic power using a bank of band-pass filters. The later extract the harmonic components from the current signal then re-inject them into the grid. Resistive output impedance can be a good solution to share linear and nonlinear loads in applications such as uninterruptible-power-supply systems [43]. In [44] a novel fast control loop that adjusts the output impedance of the closed-loop inverters is used in order to

ensure resistive behaviour with the purpose to share the harmonic current content properly. Inductive output impedance seems to be the most natural output impedance [27]. However, it degrades the output-voltage total harmonics distortion (THD) too much when supplying nonlinear loads due to the large impedance value seen by the current harmonics. A complex output impedance is presented in [42] that suggested a new design of a virtual output impedance composed of a virtual resistor with a virtual inductor associated by HPF. Eventually, it behaves like an inductor at nominal frequency and represents a resistive behaviour against harmonics frequencies.

D) **Modelling**:

It is necessary to build the stability margins of a microgrid and analyse the controller's functions against the uncertainties in the system. In grid-connected mode, each unit could be dealt as a single unit as the grid stiffness decouples the interaction between the inverters. However, in island mode, the dynamics of each inverter is affected by other inverters. The commonly used method to build a microgrid model is the small signal technique. In [24],[25],[8] a grid-connected inverter model is developed and the responses have been analysed and compared to a practical setup results, while in [26], two island inverters are modelled to investigate the droop gains stability margins. In [45] a complete microgrid contains multi island units model is built in dq-frame and a comprehensive root plot is obtained for stability judgment. The outcome of reference [46] is that the stability deteriorates by long cables connecting each inverter to the load in

an island microgrid and a low bandwidth voltage controller is recommended. In addition, a feed-forward loop is added in [47] to stabilize the system against the resultant resonance. In [22],[48],[24] the number of parallel inverters also is investigated against the microgrid stability in terms of output impedance and resonance creation.

E) **Hierarchal control**

For developing a flexible microgrid, it is necessary to distribute the control tasks over levels. The latter decouples the control parameters and creates a management system for frequency and voltage restoration, reactive power compensation, mode transfer, power settings, voltage regulation and power sharing. The following is the hierarchical control required for an AC microgrid proposed in [17]:

- Primary control based on the droop method to allow the connection of different ac sources in parallel and to share the load wirelessly. In addition, it is responsible for the voltage and current regulation in terms of a particular reference.
- Secondary control avoids the amplitude and frequency deviation produced by the primary control. Only low-bandwidth communications are needed to perform this control level. A synchronization loop can be added in this level to transfer from islanding to grid-connected modes.
- Tertiary control allows import/export active and reactive power to the grid, estimates the grid impedance and non-planned islanding detection.

Reference [17] proposed a PI controller to implement the secondary and tertiary control after sensing the voltage, current and frequency at both sides of STS and sending them by low bandwidth communication.

By this sort of level distribution a seamless mode transition is achieved to reduce the initial circulating currents. Other works are proposed in [8], [49] and [5] for the sake of managing these tasks automatically as well.

2.3. Transient Power during Unintentional Islanding of Microgrids

A microgrid can operate in grid-connected mode and in stand-alone mode. In grid-connected mode, inverters can export power to the grid (when the price is advantageous for example) or import power and store it in energy storage systems (ESS) to be used later. In case of a power outage, the microgrid works autonomously and provides power to the local loads. In order to provide an uninterruptible power supply, it is necessary for the microgrid to be able to transfer seamlessly from grid-connected mode to island mode and vice-versa.

Using droop control it is possible for the inverter to transfer from the grid-connected to the stand-alone mode automatically. During, grid-connected mode, the frequency is stiff and maintained by the power grid. Hence, the power set-point of the droop controller can be used to control the power output of the inverter. This power set-point can be set by an energy management system implemented inside the supervisory controller, i.e. MGCC. In stand-alone mode, however, the frequency can deviate from its nominal value depending on the amount of power drawn by the local load and the power set-point can be used

to reduce this deviation. In the case of multiple inverters operating in stand-alone mode, each set-point has to be adjusted according to the power rating of the inverter, i.e. according to the droop gain. Therefore, the power set-point has two different purposes depending on the mode of operation: 1) in grid-connected mode, power set-point is set to control the output power. 2) In stand-alone mode, it is used to reduce the frequency deviation. Before changing from grid-connected to stand-alone mode the supervisory controller needs to bring all the power set-points of all paralleled inverters to their nominal values before disconnecting them from the grid. However, if unintentional islanding occurs, it is not possible instantaneously to adjust the power set-points to match the load demand and circulation power can flow from the inverters with higher power set-points to inverters with lower set-points. It is important to note that by using the anti-islanding strategy, the period from grid failure until the opening of the STS may vary depending on the mismatch between the power generated by the microgrid and the local distributed load. If the mismatch is large, the islanding detection will be quite quick. However, if the mismatch is small, it will take longer for the anti-islanding controller to detect the grid loss. In the worst case scenario of perfect match between the power generated and the load, the anti-islanding controller should not take more than 2 seconds according to the IEEE Standard 1547 [50]. If one inverter imports power during this period, the DC link voltage will rise and might exceed the maximum limit. This will cause the inverter to shut down to prevent any possible damage. Even though there has been a number of publications recently on seamless transfer of microgrids [8],[17], and [49], the effect of different power set-points on the transient power between inverters has not yet been discussed.

2.4. Reactive Power Sharing

A significant concern of the parallel-operated inverters is the load sharing issue. Many techniques use communication-based methods [51]-[56] to accomplish accurate load sharing. However, these techniques need a high-bandwidth communications infrastructure between all inverters, which increases cost and decreases reliability and the plug and play ability which makes it easy for any inverter to be connected to the microgrid without prerequisite tough requirements or configuration. Droop control which mimics the behaviour of synchronous generators [8]-[24] introduced the key for inverters to operate in parallel without any communication mechanism. For the droop controller to share reactive power accurately, the parallel-operated inverters must have the same output impedance, including the cable's impedance, as well as generating the same output voltage. This, however, cannot be guaranteed in practice due to parameter tolerance in inverters' LC output filters, different interconnecting cable length and inaccuracy in output voltage control. Therefore, traditional droop control has been known for its poor performance in reactive power sharing.

Many strategies have been proposed to enhance reactive power sharing. An algorithm has been proposed in [58] which is based on additional control signal injection. The proposed solution injects signals with other frequencies (90Hz, 130Hz) to send the information about the shared power between inverters through the same distribution lines. However, this could increase the control complexity and current distortion. Chia et al. [59] proposed a method to compensate for the line impedance mismatches in which the reactive power is controlled in proportion to the voltage derivative. Although this method

minimizes the reactive power sharing error, it does not achieve equal sharing and it adds more complexity to the system. In [60] a centralized controller has been proposed to compensate for the voltage drop caused by droop controller and line impedances. However, the whole process is executed in the microgrid central controller (MGCC) and all parameters are sent by a communication link and any loss in this link would lead to the traditional droop limitations.

Li et al. [30] proposed an online estimator of the voltage drop caused by the transmission lines to then refine the droop control gain to give an accurate Q sharing in island mode. However, the algorithm needs the inverters to operate in grid-connected mode initially to obtain a proper estimation to calculate the new droop gains. In addition, the controller complexity increases with the presence of local loads that affect the estimation process.

In [61], a novel controller that is robust against computational errors and component mismatches is proposed. The accuracy of the controller does not depend on the output impedance. It measures the load voltage continuously by a wired link and computes the difference between this measure and the local output voltage. This difference is an input to an integral controller to achieve accurate sharing of reactive power. However, this system only works accurately for local inverters near each other and local loads. For a far load point or large distances between the inverters, a wireless link could be used and any loss in this communication link even for a short period of time might lead to instability due to the existence of the integral controller. Furthermore, the controller does not take into account the cable's impedances that contribute to sharing inaccuracy if a local output voltage is fed back.

Jinwei et al. [62] proposed a synchronized algorithm guiding all units to share the reactive power accurately by incorporating the measured reactive power in the frequency droop equation. However, this disturbs intentionally the active power sharing accuracy. In addition, for any load variation after compensation, the accuracy of the sharing deteriorates and hence the algorithm needs to be executed again. The same authors in [63, 64] proposed an online estimation technique of the line impedance, using the harmonics of the line current and PCC voltage, to regulate the virtual impedance and enhance the reactive power sharing accuracy. However, the controller complexity increases as well as the dependency on harmonics calculations which assume the existence of non-linear loads during the estimation period.

2.5. Impedance Interaction between Island Parallel Voltage Source Inverters and the Distribution Network

When controlling a microgrid, it is important to ensure the stability of each unit as well as the microgrid as a whole under different loads and system conditions. In many practical scenarios, the inverters are located far away from each other and therefore they are connected to the network via cables with non-negligible impedance. This could cause the voltage controllers of DGs working in parallel to become unstable.

Each inverter is normally controlled by a core controller that regulates the inverter's output voltage, and an outer droop controller that sets the amplitude and frequency references for the inner core controller. The core controller has much higher bandwidth and hence faster response than that of the outer droop

controller and therefore the dynamic behaviour of the inner core controller is normally neglected in the design and analysis of the droop controller. Consequently, the interaction between the core voltage controller and the distribution network (consisting of cables, loads and other inverters) is often discarded. However, in practice, the DGs voltage controller can become unstable due to the interaction between the output impedance of each inverter and other inverters and cable impedances that can create parallel and/or series resonance. If the resonance frequency is within the bandwidth of the voltage controller, instability could occur. Thus, designing the inverter controller as a single isolated unit does not guarantee stability in all conditions.

Different types of controller including PI [24], repetitive [65], resonant [66], deadbeat [67] and many other controllers [68] have been used in grid-connected inverters. They usually utilize dual loop control to dampen output filter resonance -. However, the interaction between the inverter and the network is rarely considered or addressed when designing these controllers. In [46], the interaction between uninterruptible power supplies (UPS) was investigated. The study recommended reducing the voltage controller bandwidth by manipulating the voltage and current controllers' gain to keep the system stable. In [47], the controller bandwidth was reduced by using a feed-forward loop. Ref [47] also concluded that a resistive virtual impedance has no effect on the system stability. However, the effect of inductive virtual impedance associated with cable lengths was not addressed.

2.6. Conclusion

In inverter-based microgrids that adopt the droop control as a power sharing technique between the inverters, the seamless transfer between grid-connected mode and island mode and vice-versa is a significant issue. Furthermore, the accurate power sharing, particularly, the reactive power is necessary to remove the risk of loading any inverter more that its ratings besides ensuring the stability of each inverter when it is coupled with other inverters. The literature has not addressed the power flow between the inverters during unintentional islanding that could cause damage or fault trips. In this thesis, the latter issue is studied in detail through a research methodology of analysis, modelling and proposing a controller. A small signal model of two islanded inverters was developed to predict the system transients and give a sense for accurate controller design. In addition, the results have been validated by simulation and practice. For the reactive power sharing, the literature showed how the communications play an important role to maintain accurate sharing. However, the loss of this communication link has not been addressed as it might destabilize the system is some cases that need remote measurement points. The work in this thesis showed how this could be detrimental and proposed a solution that decreases the possibility of unstable system and the dependency on the communications. The literature addressed the impact of long cables between island inverters and the impedance interaction that might create a resonance and shift the entire microgrid system to instability. For that issue, a new proposed controller, in this thesis, is also developed and the stability margins have been analysed by the root locus and bodeplot figures.

Furthermore, a simulation using Matlab/Simulink is built to validate the theoretical results and calculations.

Finally, this thesis also exposed the analysis, structure and the steps of building a laboratory scale microgrid which was used to validate practically the research outcomes.

CHAPTER 3 BUILDING A LABORATORY-SCALE MICROGRID

3.1. Introduction

The research methodology used in this work in order to achieve the objectives of this thesis includes; firstly, reviewing the literature for the most recent work in this topic; secondly, using analytical methods such as small signal modelling; thirdly, conducting numerical modelling using simulation tools, namely. Matlab/SimPowerSystems toolbox; fourthly, verifying modelling and design by practical implementation. This chapter discusses the design and implementation of a laboratory-scale microgrid consisting of two inverters and local load for the experimental phase of the research work. A controller for the two voltage source inverters is designed and implemented. A detailed description of the system components and the controller platform are provided. A dSPACE unit has been used to realize the controller and monitor the system in real time with the aid of a host computer. Experimental results of the two voltage source inverters are presented.

3.2. Overview of experimental setup

A complete schematic diagram of the experimental setup is shown in Figure 3.1.

As shown, the setup consists of two parallel inverters. The inverters hardware used is the SEMIKRON SKAI module which is designed for three-phase systems. However, only two phases were used which were configured as a

single phase H-bridge inverter. The output of the inverter system is connected to a low pass LCL filter, and coupled to the grid through an autotransformer. Diodes are placed between the DC power supply and each inverter's DC link. This is to protect the DC power supply in case the dc current flows in the reverse direction. In addition, the diodes allow the DC link voltage to rise above the DC power supply voltage which is quite important to study the effect of circulating transient power on DC link voltage. This will be discussed in Chapter 4.

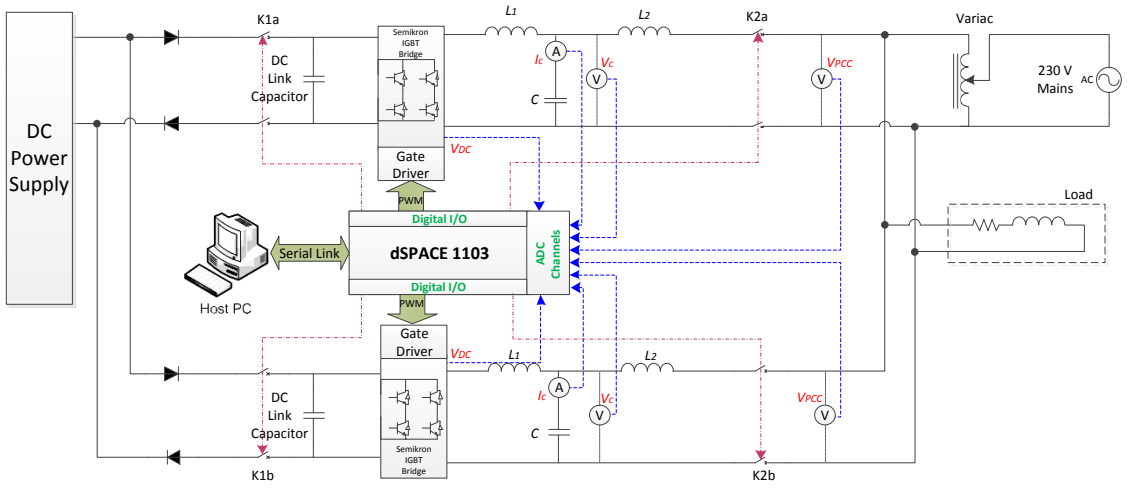

Figure 3.1. Schematic diagram of the experimental setup containing two inverters with LCL filters and controlled by dSPACE unit

Voltage and current signals are measured using LEM sensors and fed-back to the controller unit. Contactors K1, K2 are used to isolate the inverter from the DC source and the grid, respectively. Contactor K1 closes first to supply the inverter with DC power. Contactor K2 is then used to connect the inverter to the network. The controller algorithm is implemented using dSPACE 1103 unit which is a real time controller that can be configured and programmed using

Matlab/Simulink. In addition, it has the ability to acquire the signals from the sensors and produce the output signals to the power switches and contactors. A host personal computer (PC) is used to provide a graphical user interface platform which displays the results and gives the ability to change the controller parameters in real time. This platform is called ControlDesk.

A full description of the experimental components is presented in the following sections.

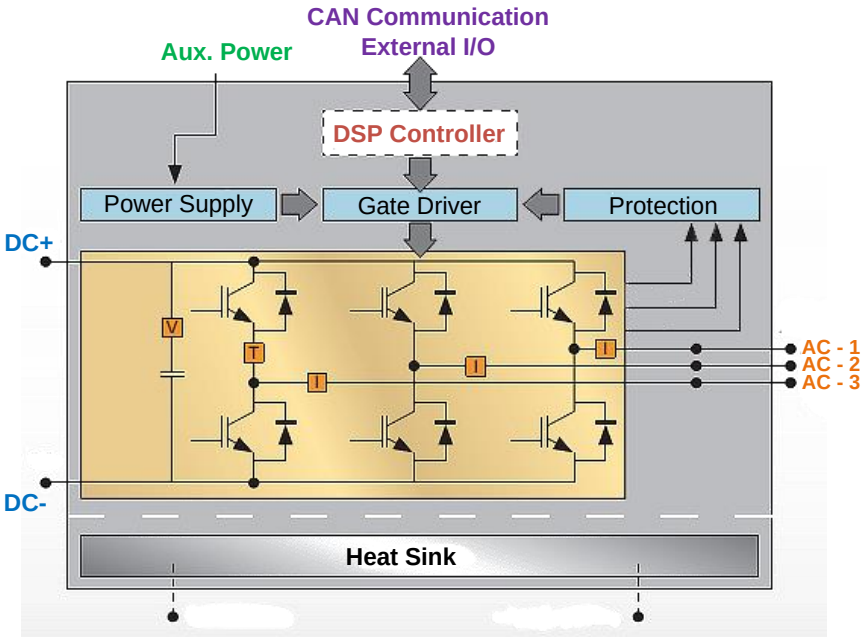

Figure 3.2 Block diagram of SKIA module

3.3. Inverter Module

Two SKAI inverter modules produced by SEMIKRON are used in this setup. SKAI is a highly integrated two level half-bridge 3-phase inverter which is primarily designed for driving 3 phase loads from a DC source. However, only two phases have been used as a single phase H-bridge inverter as mentioned

earlier. Figure 3.2 shows a block diagram of the SKAI module and Figure 3.3 shows a picture of it.

The SKAI module contains 6 IGBT switches with freewheeling diodes, DC link capacitor, integrated current sensors, temperature sensors and protection logic. Integrating the DC link capacitors in the design reduces the internal inductance and allows higher bus voltages to be used. Integrating the DC link capacitor also allows less capacitance to be externally used for a smaller and more reliable design. This compact construction is extremely rugged making it ideal for the experimental setup.

There are two subcategories of SKAI modules, Low Voltage (LV) and High Voltage (HV), depending on the rated voltage of the semiconductor switching devices. The HV module is used in our setup as this is the one that is available in the laboratory.

Figure 3.3 SKAI 3001GD12 Module [69]

The model number of the two modules used is SKAI 3001GD12-1452WI3 (see Figure 3.4 for explanation). The module specifications are listed in Table 3.1.

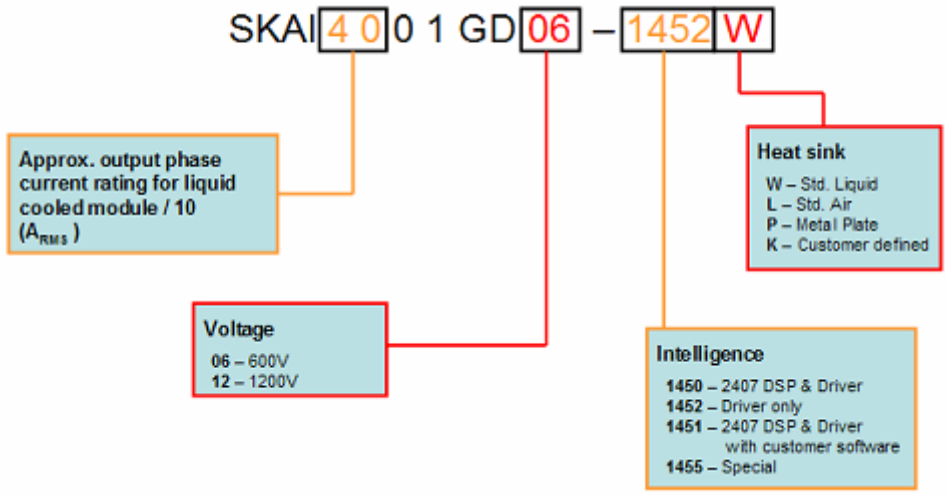

Figure 3.4 SKAI Model number explanation [69]

Module Rating	1200	Units
Silicon voltage	1200	V
IGBT breakdown voltage	1200	V
Maximum DC link voltage	900	V
Maximum continues AC output current	300	Arms
Peak current limit	1000	A
DC link trip voltage	917	V
DC link capacitance	1	mF

Table 3.1 Specifications of SKAI nodule

The rest of module's input and output signals and other properties are illustrated in the appendix A.

3.4. Voltage source inverter model

In a power-electronic based microgrid, DG units are based on voltage source inverters (VSI) which can operate in stand-alone and grid-connected modes of operation. Figure 3.5 shows a transfer function block diagram of an inverter and its voltage controller which consists of two feedback loops; an outer feedback loop of the capacitor voltage and an inner feedback loop of the capacitor current. The inner current loop is employed to provide active damping of the resonance created by the LCL filter. A feedforward loop of the reference voltage is also implemented to improve the controller response speed and to minimize the steady state error.

Note that the filter inductor current (I_f) or the filter capacitor current (I_c) can be used as the inner feedback loop. The filter inductor current feedback gives better performance in terms of LC resonance damping and overcurrent protection. The filter capacitor current feedback, however, gives better performance in terms of load current disturbance rejection [70] beside resonance damping as the capacitor current relates the control loop to the derivative term of the output capacitor voltage which gives rapid response action against the disturbances. Therefore it is used in this work.

From Figure 3.5, without considering the current feedback filter $H_f(s)$, the output voltage can be shown to be given by,

$$V_o = G(s)V_c^* - Z(s)I_o \qquad (5)$$

where $G(s)$ is the closed loop transfer function and $Z(s)$ is the system output impedance, and given as,

$$G(s)=\frac{k_v+1}{L_1Cs^2+k_cCs+k_v+1} \tag{6}$$

$$Z(s)=\frac{L_1s}{L_1Cs^2+k_cCs+k_v+1}+L_2s \tag{7}$$

where k_c is the current loop controller gain and k_v is the voltage loop controller gain. From (6), the natural frequency and damping ratio can be obtained as $\omega_n=\sqrt{(k_v+1)/L_1C}$ and $\zeta=k_c\sqrt{L_1C/(k_v+1)}/2L_1$, respectively.

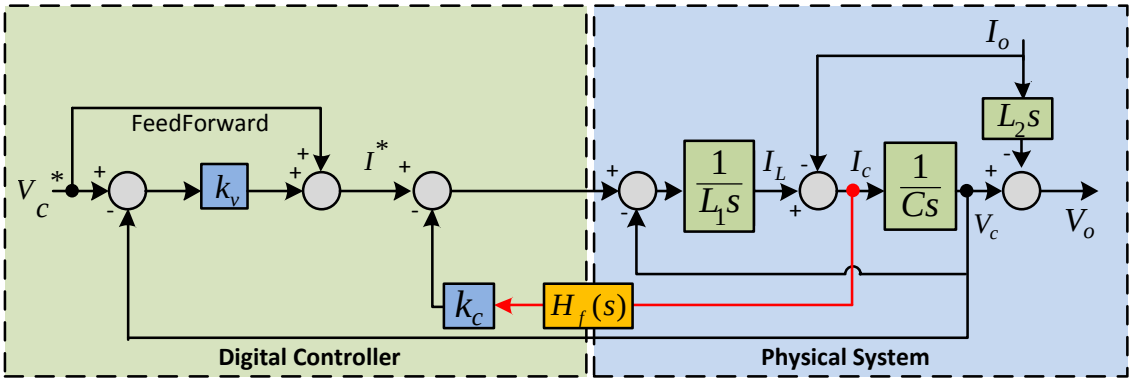

Figure 3.5. Double-loop feedback voltage controller

Inverter parameters		
Symbol	Description	Value
L_1	Inverter-side filter inductor	350μH
C	Filter capacitor	160μF
L_2	Grid-side filter inductor	250μH

Table 3.2 Inverter's filter parameters

The filter parameters are listed in Table 3.2. The system stability is studied using the root locus of the voltage controller as shown in Figure 3.6 as the gains are changing in the range $0<k_c<5$ and $1<k_v<10$. It is obvious that higher

k_c introduces more damping while k_v has a little impact. As a rule of thumb, the damping ratio ζ is chosen to be between 0.3 and 0.7. Therefore, the controller gain values are chosen such as $k_v = 2$ and $k_c = 2.2$. This gives a damping ratio $\zeta = 0.43$ and $\omega_n = 7319\, rad/sec$. The step response settling time for $G(s)$ is about 1 m sec.

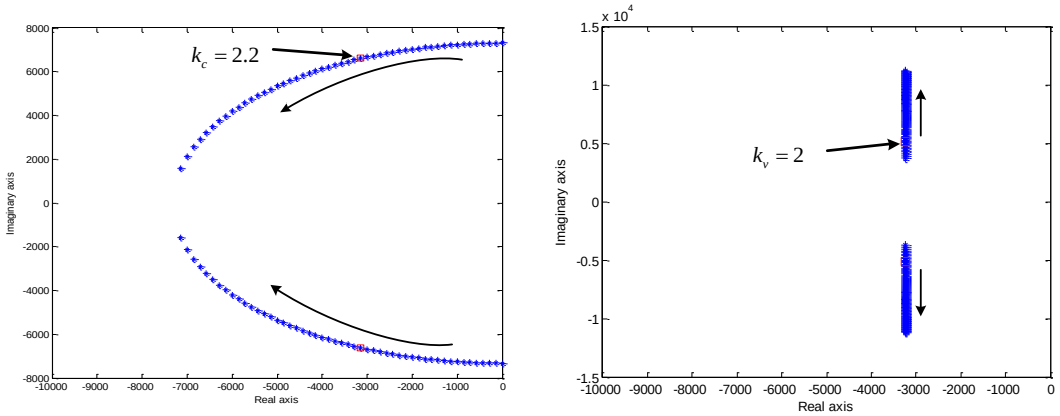

(a) (b)

Figure 3.6. Root locus of the voltage controller as (a) $0 < k_c < 5$ (b) $1 < k_v < 10$

By considering the current measurement filter, the closed loop transfer function is given by,

$$G(s) = \frac{k_v + 1}{L_1 C s^2 + k_c C s . \frac{\omega_f}{s + \omega_f} + k_v + 1} \tag{8}$$

where ω_f is the cutoff frequency of the measurement filter. It is clear that the filter adds new zero and pole to the system that could affect the system stability and response. Figure 3.7 shows the bode plot of $G(s)$ in (8) as ω_f changes. It is clear that lower ω_f introduces a resonance at around 1.37kHz. Higher values of ω_f can provide good damping for this resonance. In terms of phase shift, the phase shift around the fundamental frequency (50Hz) can affect the accuracy of

the power measurement required for the droop control. However, the phase shift at 50Hz is -2.4º and the effect of ω_f is minimal. Low cutoff frequency $\omega_f = 0.5kHz$ gives good noise rejection but it produces a low phase margin to the system compared with the high cutoff frequency ($\omega_f = 200kHz$). Thus, the filter cutoff frequency is set to equal 200kHz which gives a good compromise between stability and noise rejection.

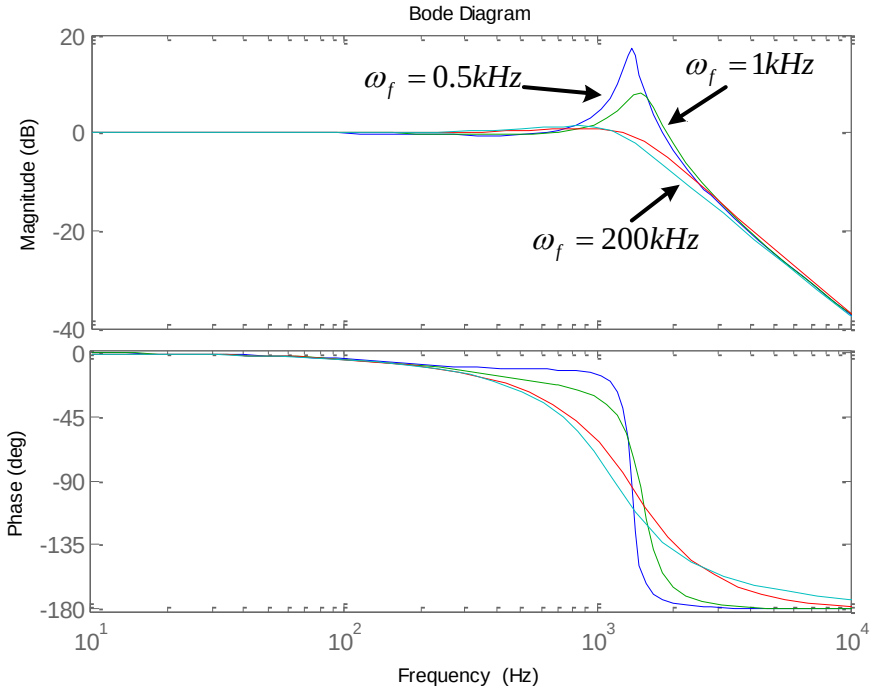

Figure 3.7. Bode plot of $G(s)$ as the filter cutoff frequency changes

From the transfer function of $Z_o(s)$, the output impedance has the same characteristic equation as that of $G(s)$ and they have the same poles. The bode plot of $Z_o(s)$ is shown in Figure 3.8. As seen, it has a predominant inductive behaviour in the vicinity of the fundamental frequency. This is important for proper droop control operation. Therefore, it is reasonable to assume

$$Z_o(s)\big|_{s=2.\pi.50} = s.L_o \tag{9}$$

where L_o is the inductance that is seen at the output of the inverter at the fundamental frequency.

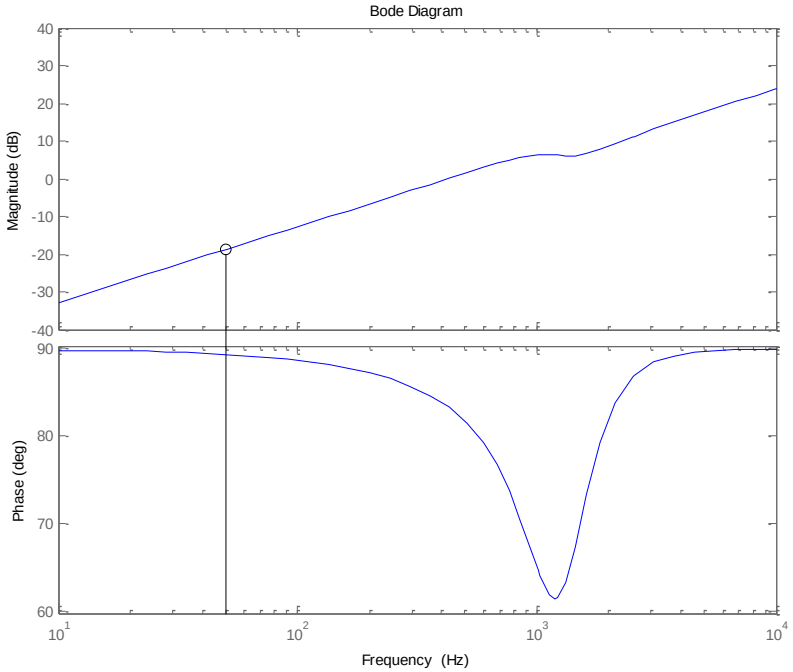

Figure 3.8. Bode plot of output impedance $Z_o(s)$

3.5. dSPACE Controller Platform

The dSPACE DS1103 real time controller consists of two parts; the main development board DS1103 and the connector panel CP1103 (see Figure 3.9). The DS1103 controller board is specifically designed for the development of high-speed multivariable digital controllers and real-time simulations in various fields. It is a complete real-time control system based on a PowerPC processor. For advanced I/O purposes, the board includes a slave-DSP subsystem based on the Texas Instruments TMS320F240 DSP microcontroller as shown in Figure 3.10.

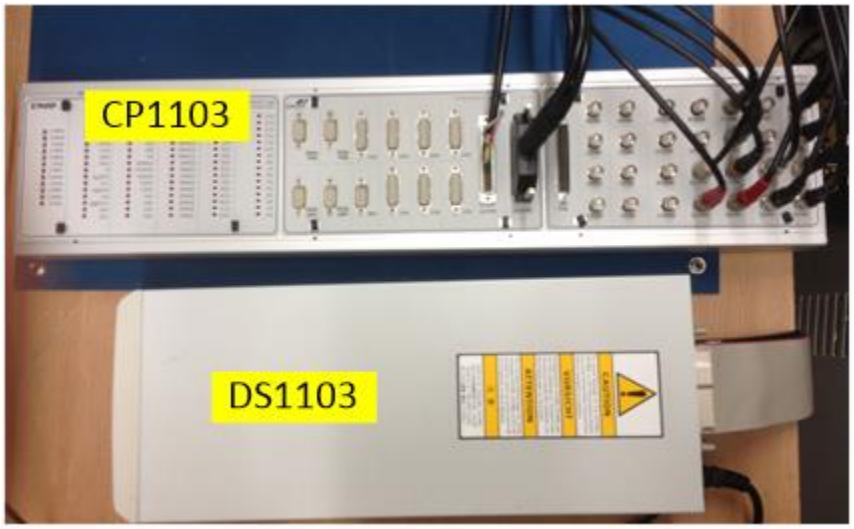

Figure 3.9 View of DS1103 and CP1103

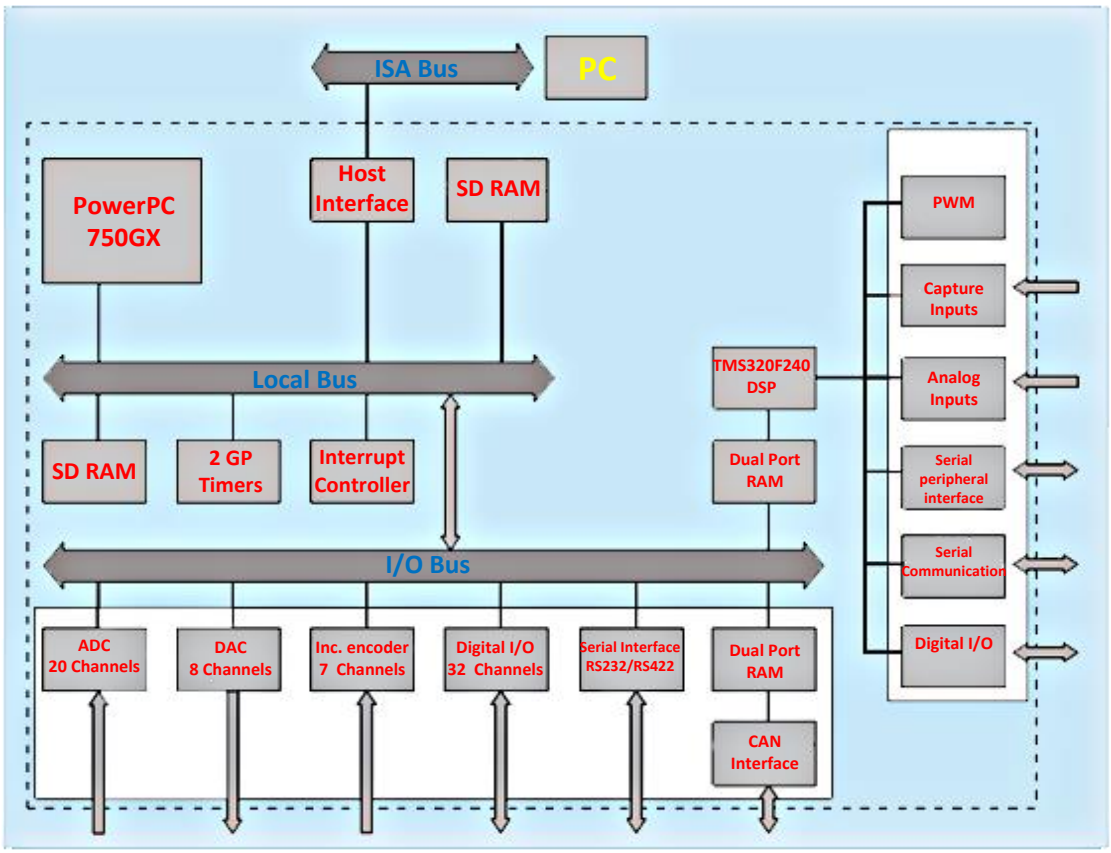

Figure 3.10 Internal structure of DS1103

The connector panel CP1103 serves as an interface between the DS1103 controller board and external devices. It provides easy access to all input and output signals of the DSP. Devices can be individually connected, disconnected or interchanged without soldering. This simplifies system construction, testing and troubleshooting.

The CP1103 contains connectors for 20 Analogue-to-Digital (ADC) converter inputs, 8 Digital-to-Analogue (DAC) converter outputs, several other connectors that can be used for Digital I/O, slave DSP I/O, incremental encoder interfaces, Controller Area Network (CAN) interface and serial interfaces. The electrical specifications of the ADCs and I/O pins are listed in Table 3.3.

The main control algorithm is implemented in DS1103 using the Real Time Workshop in Matlab/Simulink environment. This gives more flexibility and allows the integration of functions from the Simulink library. The interface with the host PC is realized via a Serial Communication Interface (SCI) that exchanges all data with the controller and can be manipulated and displayed using a graphical user interface.

The general connection between DS1103, CP1103 and the inverters inputs and outputs is shown in Figure 3.11. The analogue inputs of CP1103 are connected to the measurement sensors of each inverter to be used by the controller. The digital I/O is connected to the IGBT’s inputs and error outputs pins of each inverter module.

	Parameter	Value		
Analogue Inputs	Input voltage	Min		Max
		-10V		+10V
	Input resistance	1 MΩ		
Digital I/O	Input voltage		Min	Max
		High	2V	5V
		Low	0V	0.8V
	Output voltage	High	2.4V	5V
		Low	0V	0.4V
	Output current	10mA		
	Input current	500μA		

Table 3.3 Specifications of CP1103

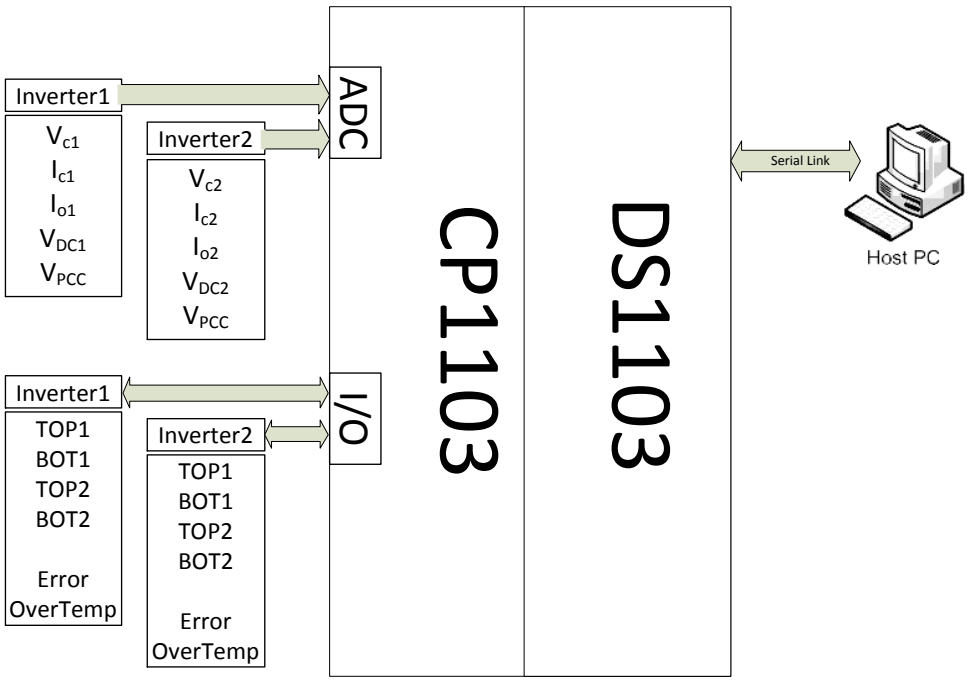

Figure 3.11 DS1103 and CP1103 connection with inverters inputs and outputs

3.6. Interface Board

Each inverter system has two contactors: an input contactor that connects the DC link capacitor to the DC source (K1 in Figure 3.1) and an output contactor that connects the output to the AC bus (K2 in Figure 3.1). The digital control

signals outputs from the DS1103 controller have logic states voltage, 0V for low state and 5V for high state. The contactors, however, need 230VAC to be energized. This requires a circuit, which receives the low voltage signals and applies a corresponding signal to the contactors. Therefore, an interface board was built. The schematic diagram of the circuit is shown in Figure 3.12.

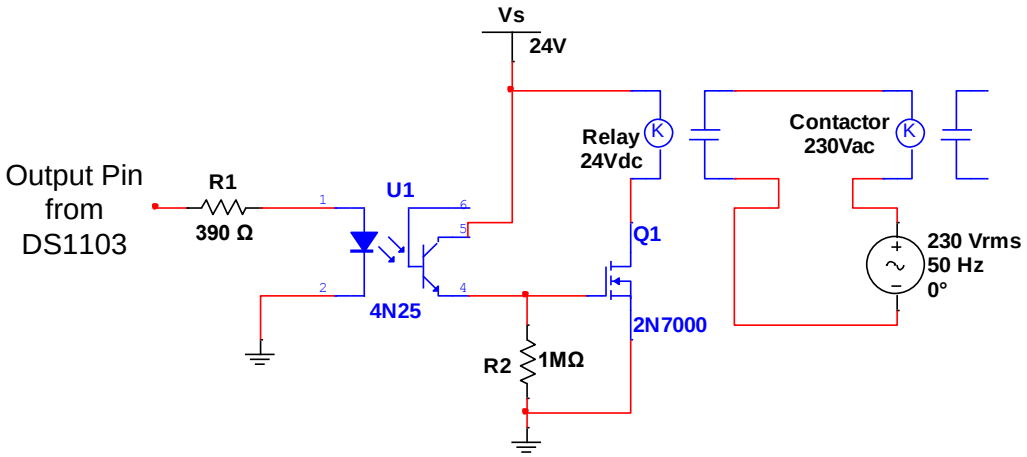

Figure 3.12 Schematic of the interface board

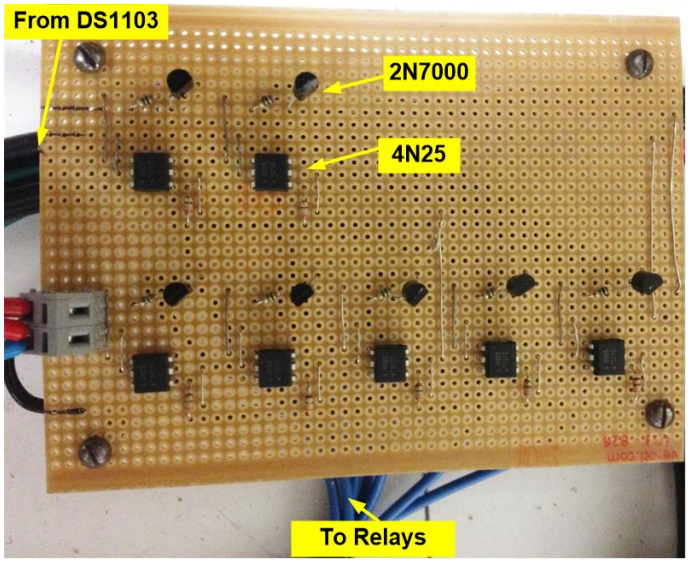

Figure 3.13 View of the interface board

The circuit uses an opto-coupler (4N25) as an isolation interface between the controller and the relays. The value of R1 was chosen to limit the current to 10mA as this is the maximum current that can be delivered by any DS1103's digital output pin. The opto-coupler drives a 24V relay, using a FET transistor 2N7000. The relay applies the desired 230Vac across the contactor coil. The complete physical circuit is shown in Figure 3.13.

3.7. Voltage and current measurements

The closed loop control of each inverter requires the filter capacitor voltage and current to be measured and fed-back. As mentioned earlier, LEM voltage and current sensors are used to measure these signals.

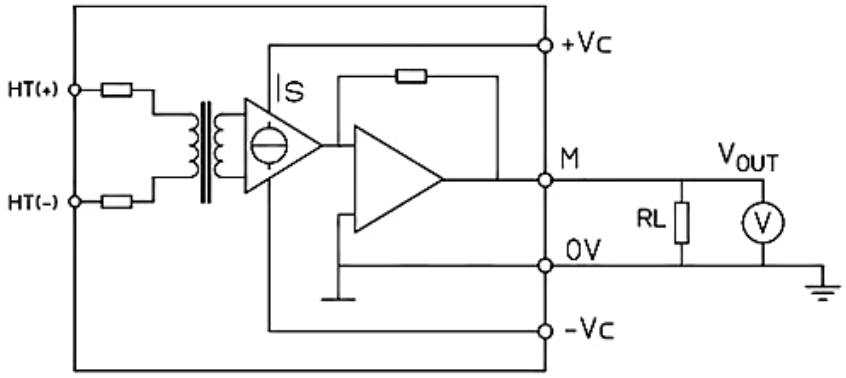

Figure 3.14 Connection of the voltage sensor [71]

3.7.1. Voltage measurement

To measure the capacitor voltage, the voltage transducer CV3-1000 is used. The sensor can handle a nominal RMS voltage of 700V and a maximum voltage of 1000V. It has a conversion ratio of 10V:1000V. The connection of the sensor

is shown in Figure 3.14. According to the datasheet, the load resistance R_L should be greater than 1kΩ.

3.7.2. Current measurement

The current transducer LA 125-P/SP4 is used to measure the capacitor current and the output current. It can measure a nominal current of 125A and its conversion ratio is 1 : 2000. The transducer output is a current signal so in order to obtain a voltage signal representing the current, a measuring resistor should be connected as in Figure 3.15 and it's value is 50 ohm as recommended in the datasheet.

An experimental test was carried out on the current sensors by measuring the current supplied from a 23Vrms source to a resistive 50 ohm load. After testing the output signal from the current sensor, it was observed that it contained high frequency noise. This noise could be acceptable if the current is high and hence the current to noise ratio is high. However, in this laboratory-scale system, the measured currents do not exceed 4A. Therefore, an active low pass filter is designed to mitigate the noise.

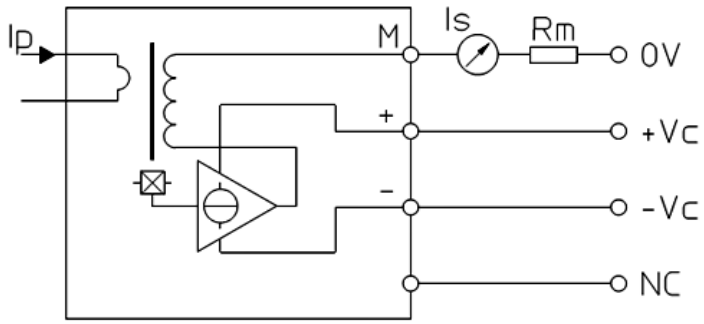

Figure 3.15 Connection of the current sensor [72]

3.7.3. Measurements filters

A low pass filter is designed using open source software from Texas Instruments called FilterPro. The cutoff frequency is initially chosen to be about 1 kHz to cancel out the high frequency noise and the schematic of the filter is shown in Figure 3.16.

The performance of the filter was satisfactory in terms of noise rejection; however, the filter cutoff frequency has an impact on the system stability as concluded from Section 3.4. The practical results of lower (1kHz) and higher (200kHz) cutoff frequency will be discussed later.

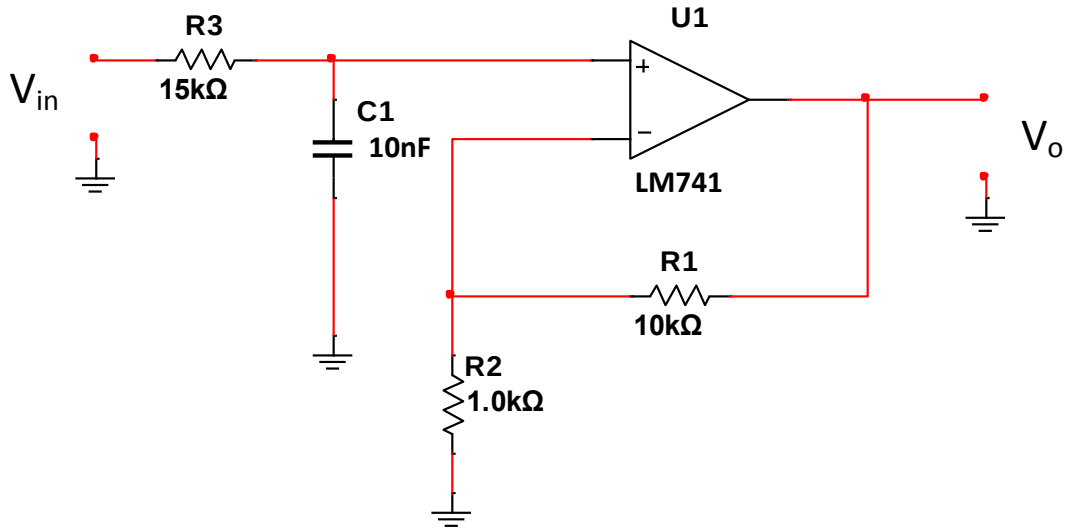

Figure 3.16 Schematic of measurement filter

A view of the final assembled filters with current sensors is shown in Figure 3.17. It depicts three sensors that are used to measure inductor, capacitor and output currents.

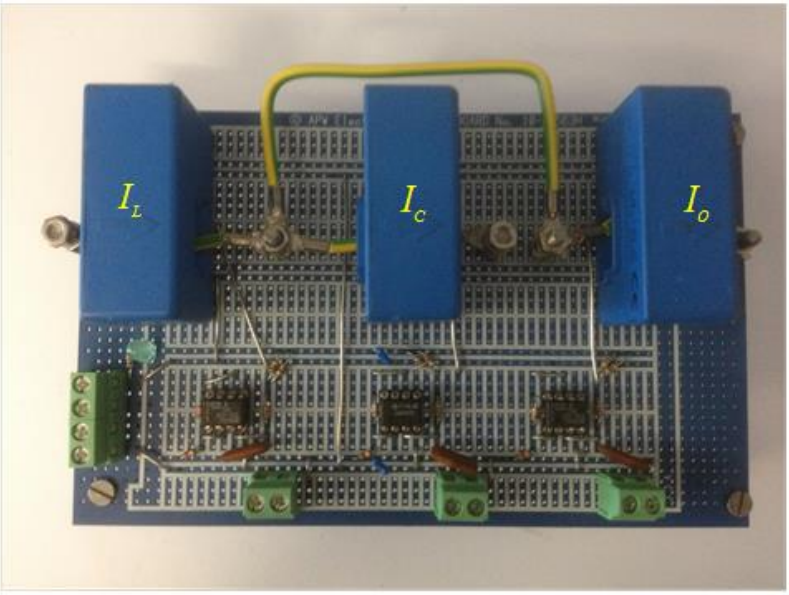

Figure 3.17 View of the current measurement filters

Figure 3.18 shows a view of the bench made for the voltage and current sensors for both inverters.

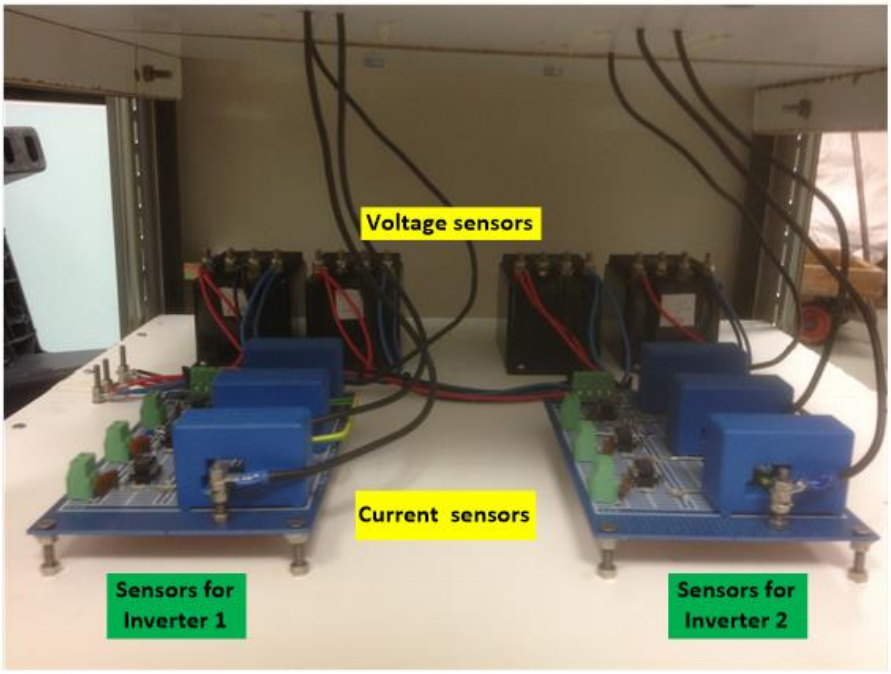

Figure 3.18 Voltage and current sensors installation

3.8. Graphical User Interface

The dSPACE has a graphical user interface (GUI) software package called ControlDesk, which provides a high-level control and monitoring of the real-time system. ControlDesk has many GUI tools such as plotters, texts and buttons. In addition, many layouts can be created and each can measure different group of signals.

Figure 3.19 shows a screenshot of the GUI developed to control and monitor the system. Controller parameters such as controller gains can be changed by the user. Measurements such voltage, current and power can be presented on the screen.

Figure 3.19 Screenshot of ControlDesk GUI

3.9. DSP Task Timing

The DSP of the dSPACE can be simply programmed by the Simulink Coder which is a Matlab tool that converts Simulink block diagrams into C code and upload it directly on the DSP memory of the dSPACE. Figure 3.20 illustrates the interconnection between the Host (Simulink and ControlDesk), dSPACE and inverters.

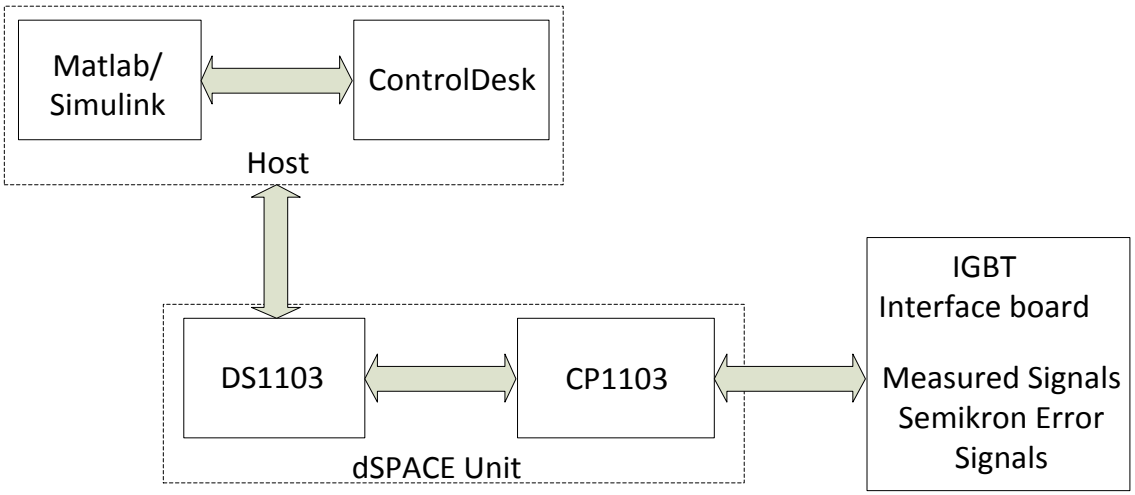

Figure 3.20 General interconnection between host, dSPACE and inverters

The role of Matlab/Simulink here is just generating the code and programming the DSP of the dSPACE while the ControlDesk is used to monitor the system variables and change the parameters as required through its GUI.

In the Simulink environment, the sampling time of the model determines the speed of the DSP code execution. The sampling time should be kept short to minimize the computational time delay. However, choosing it too short might lead to an overrun problem where the DSP is unable to perform all the controller tasks within time as shown in Figure 3.21. Thus, the sampling period has to be

chosen carefully to minimize delay and to avoid overrun. In this system, the sampling frequency of the Simulink model was set to 60kHz which was found to give satisfactory performance in terms of code execution speed while the ADC sampling frequency is 16kHz and the switching frequency is 8kHz. Less than 60kHz, the computational time is long that results distorted voltage outputs. However, this frequency caused an overrun problem which was resolved using processor “Multitasking” which is explained in the following.

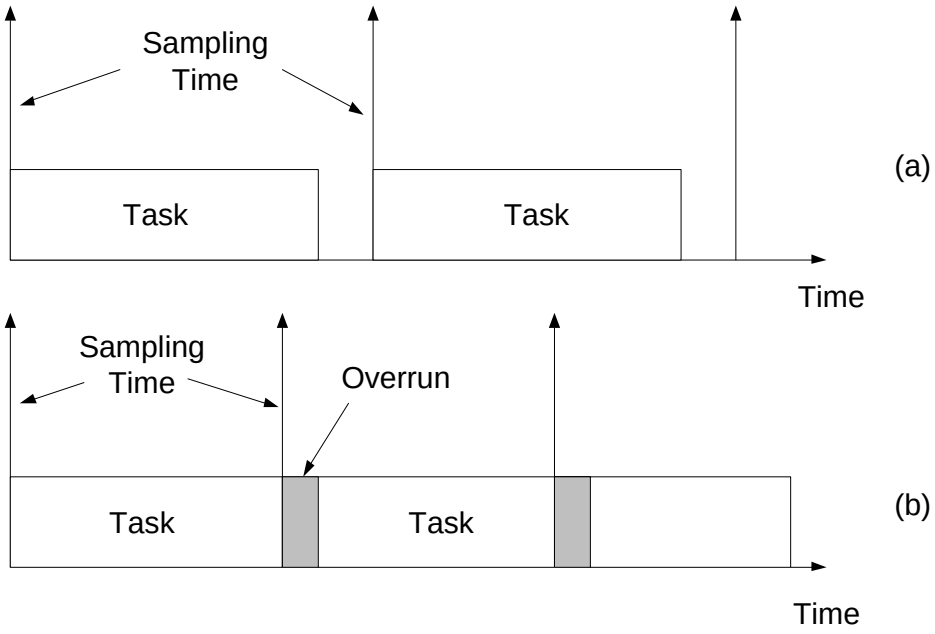

Figure 3.21 Single Timer operation (a) long sampling time (b) short sampling time (overrun happens)

The dSPACE controller has three independent timers and each can be used individually to execute some parts of the controller code. If one timer is used to execute the entire code then the operation is called single timer task mode (Figure 3.21). Otherwise it is called multiple timer task mode or Multitasking. The latter approach can be used to prioritize the execution of some controller tasks over others and it is preferable when a controller code has some tasks

that need to be executed more often than others. This happens by assigning a group of tasks to a timer and another group to another timer and so on as shown in Figure 3.22. Timer 1 executes Task A while Timer 2 executes Task B. Task A needs to be run more frequently than others so Timer 1 is faster. In addition, the priority determines which task will start first. The highest priority tasks can also interrupt the lower priority tasks. The user can determine the task speed and priority manually then Matlab automatically assigns it to a timer.

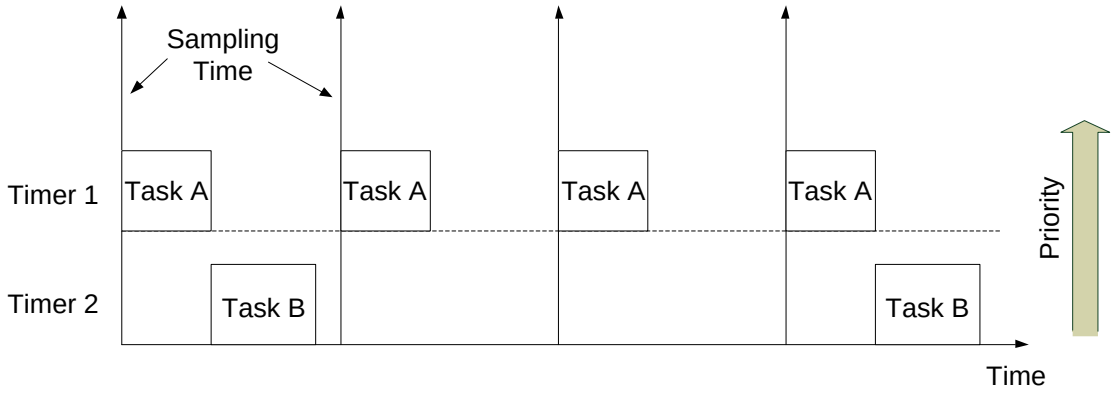

Figure 3.22 Multitasking operation concept

Figure 3.23 shows the Simulink blocks of the controller. Each block represents a different task and each is executed at a different speed (1 to 4). The task with the highest number has the lowest priority and lowest speed. Simulink blocks “PWM Generation”, “Voltage controller” and “ADC” have the highest priority and hence the highest speed because they carry out the critical part of the control algorithm and any delay in the execution can lead to instability. Power calculation and droop controller are assigned to a lower speed task since it is a slower control loop than the voltage controller. The PLL block is used for synchronization with the grid or the other inverter. It has lower priority than the

previous tasks. The rest of the tasks such as RMS and THD calculations have the lowest priority as they do not affect the operation of the controller.

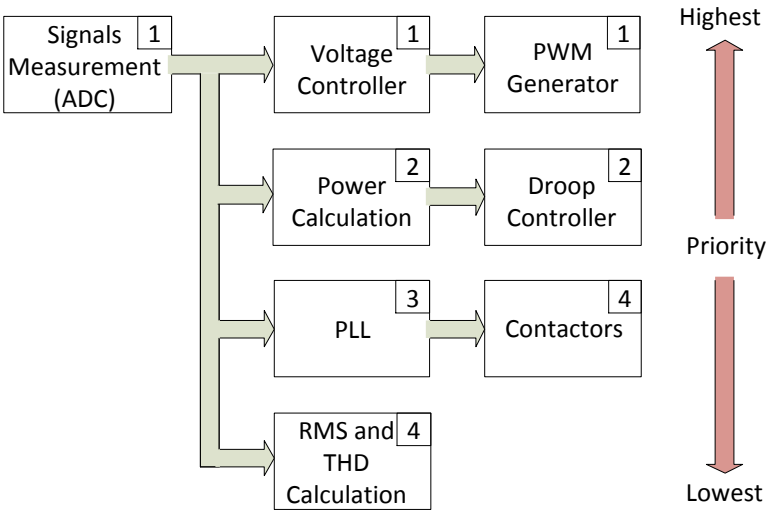

Figure 3.23 General Simulink block distribution in Multitask mode

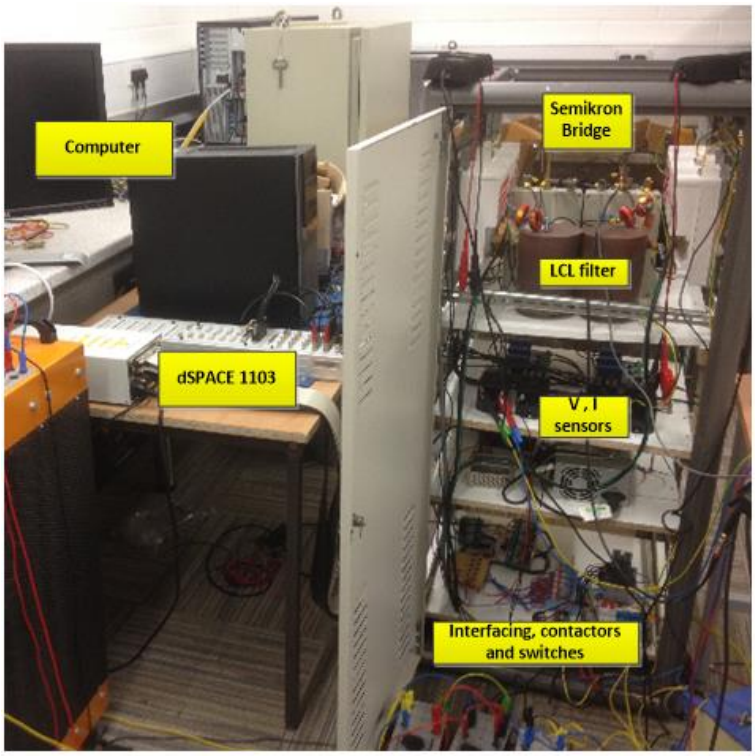

Figure 3.24. Test rig for the experimental setup

The dSPACE controller has 4 external hardware inputs used as interrupts. These interrupts can trigger some tasks independently. Therefore, they have been employed to stop the system in case of an error signal being generated by the Semikron converter.

3.10. Practical Results

Initial tests were carried out to demonstrate the functionality of the complete experimental setup that has been built in the laboratory. The results were taken using the GUI implemented in ControlDesk software.

Figure 3.24 shows a view of the power electronic inverters, auxiliary measurement equipment, host computer, and dSPACE unit for real-time control of the system.

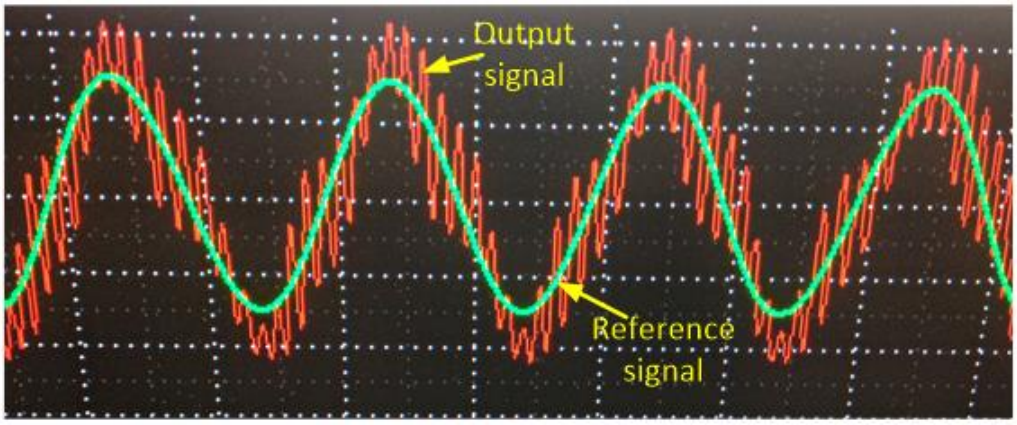

Figure 3.25 Output voltage when low (1kHz) filter cutoff frequency is used

The first test is running each inverter as a standalone inverter and supplying a load. Each inverter is supplied by 40V DC source and powering a 60w resistive load to confirm practically the impact of the current measurement filter on the

output voltage. A primary filter cutoff frequency of 1kHz is used. The output voltage is depicted in Figure 3.25 as it has a sustained oscillation of about 900Hz that is close to the resonant frequency seen in Figure 3.7. The variation between the two results is because of the parasitic resistance of the inductors that affect the resonance frequency and amplitude [73]. A simulation was carried out by building one inverter unit supplying a load with considering the measurement filter. The filter has been incorporated with the designed 1kHz cutoff frequency. Figure 3.26 shows how the system generates a resonance that confirms the results in Figure 3.7 and Figure 3.25. To mitigate the resonance, a higher cutoff frequency is chosen which provides a compromise between the noise rejection and the system stability. The new cutoff frequency is chosen as 220kHz. This is done by changing the capacitor (C1) value to 47pF in Figure 3.16. Figure 3.27 shows the practical results of the sensor's output signal with and without the measurement filter.

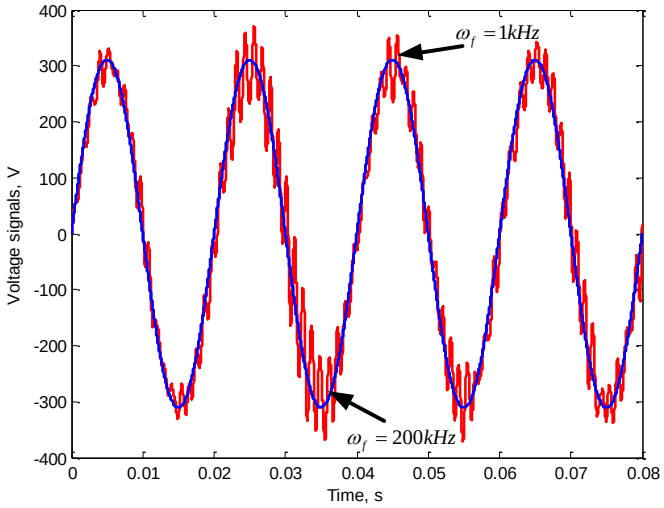

Figure 3.26 Simulation results of voltage output

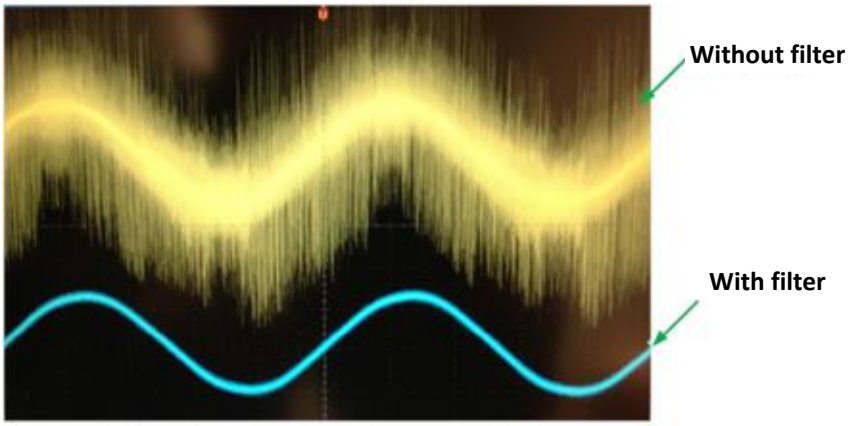

Figure 3.27 Measured current waveform with and without the filter

With the new filter configuration, Figure 3.28, Figure 3.29 and Figure 3.30 show output voltage, current and power signals of one inverter. All these results have been captured by the internal registers of the dSPACE 1103 and plotted using Matlab.

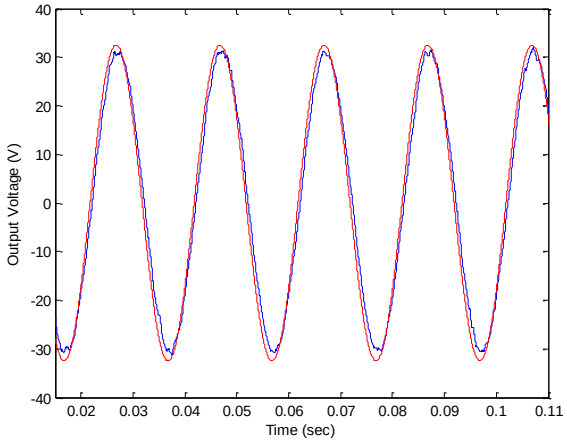

Figure 3.28 Inverter output voltage and the reference signal

The phase locked loop (PLL), used to provide synchronization between the two inverters, was tested. The PLL control loop minimizes the phase angle difference between the two inverters to reduce the initial circulating currents. Both inverters were supplied from the same DC source through diodes as seen

in Figure 3.1. The first inverter was running and supplying the load and the second inverter was connected to it by closing the contactor K2 after receiving a signal from the PLL unit.

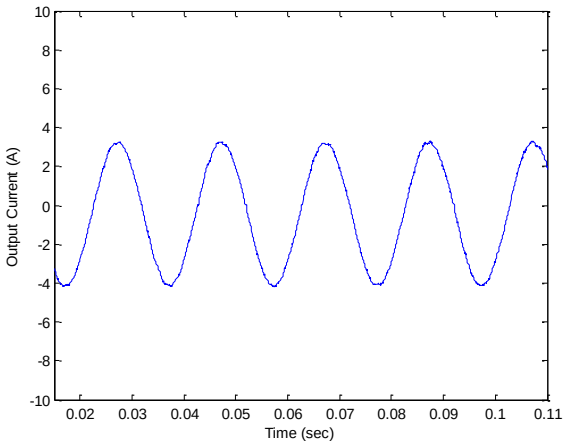

Figure 3.29 Inverter output current

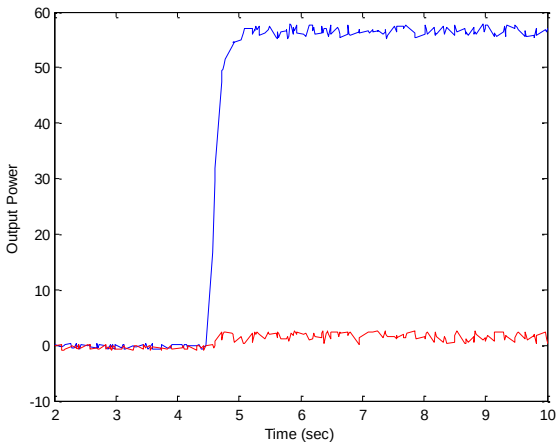

Figure 3.30 Inverter output active and reactive power when supplying a resistive load at 4.5 sec

Figure 3.31 shows the output voltages and PLL phase output during synchronization. The closing signal is generated when the phase angle between the inverters' output voltages is zero. Figure 3.32 shows the output voltages at

the moment of closing K2. The results confirm the stability and readiness of the setup to test the controllers that will be proposed in the following chapters.

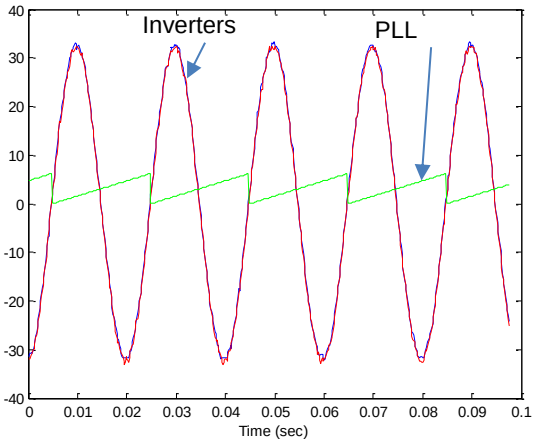

Figure 3.31 Inverters output voltages and PLL phase output

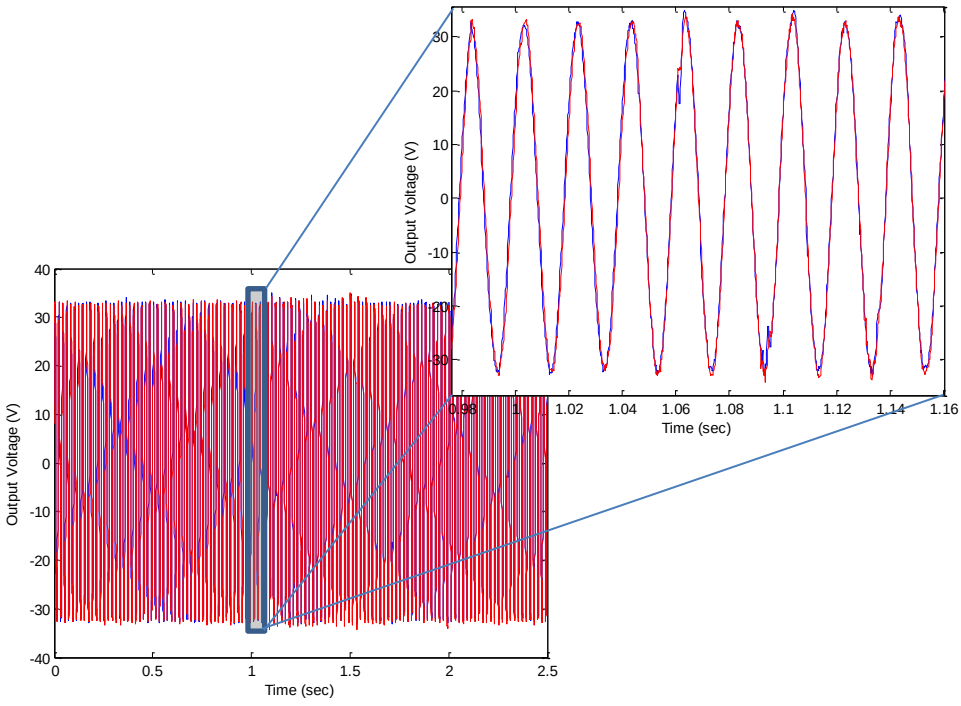

Figure 3.32 Output voltages during synchronization

3.11. Summary

This chapter has described the experimental setup built for the experimental phase of the research work for verifying the developed models and examining the performance of the proposed controllers to achieve the research aims.

A detailed explanation of the experimental setup consisting of two inverters and local load has been presented. The key peripheral components of the experimental facility have also been described. An overview of the programming environment for the dSPACE controller and ControlDesk interface has been presented, along with the discussion on the realization of the control algorithm. Experimental results of the two voltage source inverters have been presented.

CHAPTER 4 CONTROL OF TRANSIENT POWER DURING UNINTENTIONAL ISLANDING OF MICROGRIDS

4.1. Introduction

This chapter investigates the issue of transient power between parallel inverters during unintentional islanding. This circulating power can raise the DC link voltage of the inverters causing the inverter to shut down if the voltage level exceeds its maximum limit. The chapter also proposes a controller to limit this circulating power by adjusting the power set-point according to the rise in the DC link voltage. A small signal model of a microgrid consisting of two inverters in island mode is developed and used to design the controller. Simulation and experimental results are presented to validate the design.

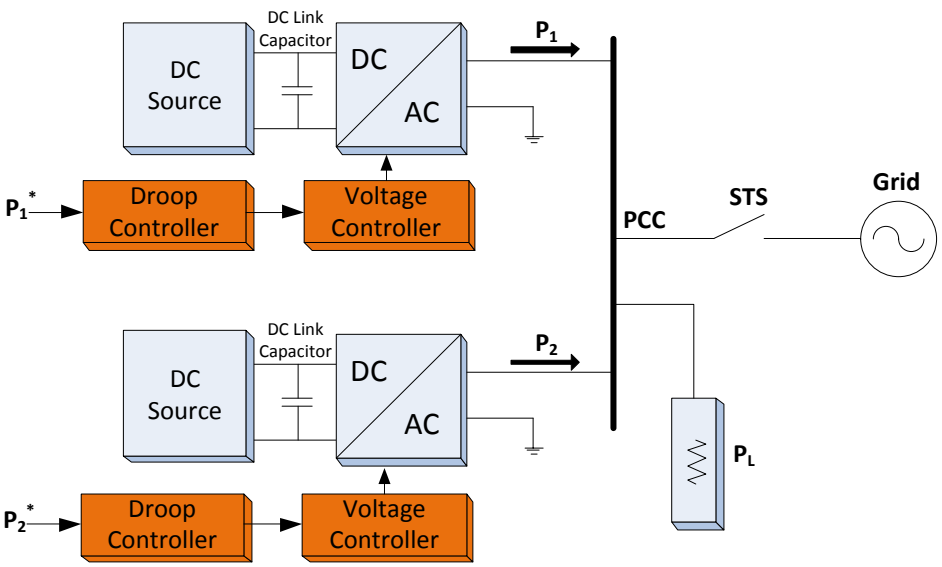

Figure 4.1. Two inverters in microgrid and their voltage and droop control

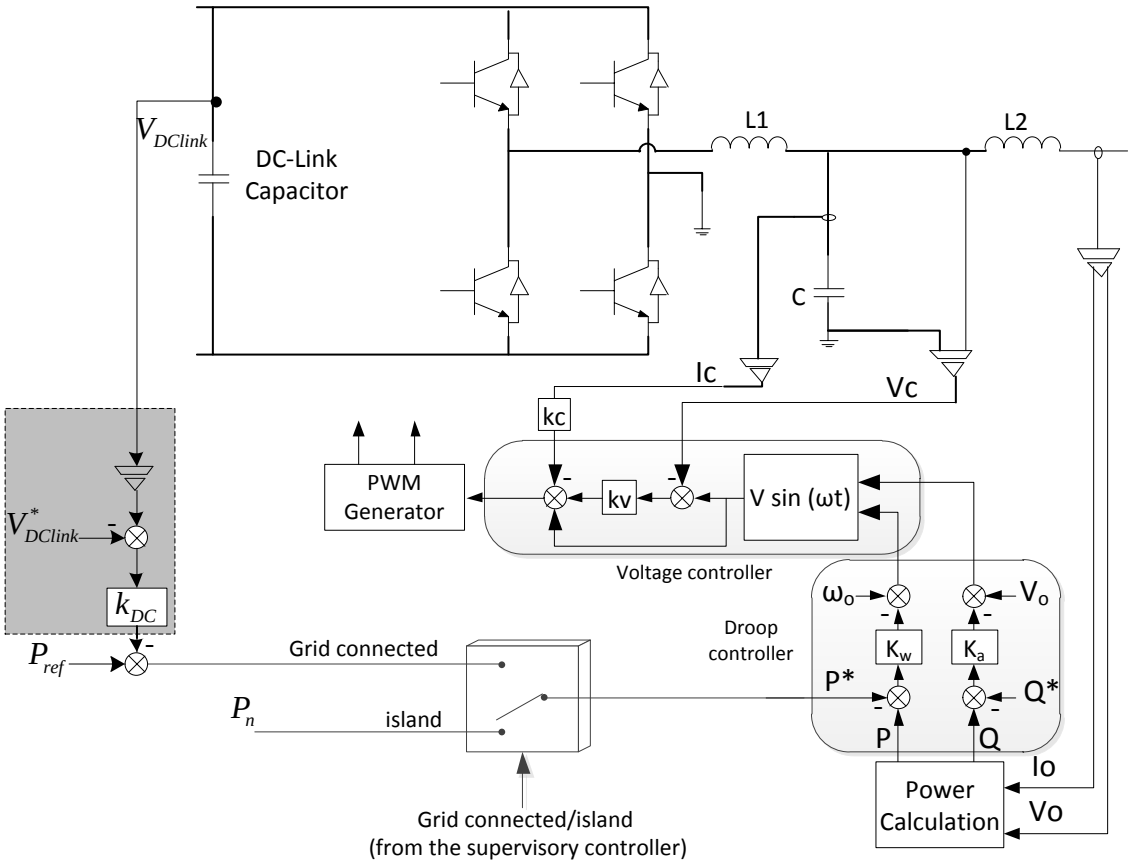

Figure 4.2. Inverter circuit diagram

Symbol	Value	Description
L_1	1350μH	Inverter-side filter inductor
C	240μF	Filter capacitor
L_2	250μH	Grid-side filter inductor
C_{DC}	2000μF	DC link capacitor

Table 4.1 DC/AC converter Parameter values

4.2. Droop Control

In this chapter, a microgrid consisting of two inverters as shown in Figure 4.1 is considered. The circuit diagram of each inverter and its LCL filter and controller is illustrated in Figure 4.2. The system parameters are listed in Table 4.1. The frequency and voltage droop control of an inverter operating in a microgrid is given by

$$\omega = \omega_o^* - k_\omega (P - P^*) \tag{10}$$

$$V = V_o^* - k_a (Q - Q^*) \tag{11}$$

where ω_o^*, V_o^* are the nominal frequency and nominal voltage references, k_ω, and k_a are the proportional frequency drooping coefficient, and proportional voltage drooping coefficient, respectively. The droop slopes are determined according to the power rating of the inverter and according to the maximum allowable variations in output frequency and voltage [74]. The active and reactive power set-points $P^*$and Q^* are set to the reference power P_{ref} and Q_{ref} in grid connected mode. In stand-alone mode, however, they are set to nominal active and reactive power P_n and Q_n to improve frequency and voltage regulation [8]. The inverter controller receives a signal from the supervisory controller about the status of the STS then the set-points $P^*$and Q^* are set accordingly as shown in Figure 4.2. Without losing generality, it is assumed that the two inverters in Figure 4.1 have the same power ratings and hence they have the same drooping gains $k_{\omega 1} = k_{\omega 2} = k_\omega$. In grid-connected mode, the inverters are assumed to have different power set-points such as $P_1^* \neq P_2^*$. Figure 4.3 shows the droop control of the two inverters with different power set-

points. During grid-connected mode, the frequency is fixed by the stiff grid ω_{grid} which equals the nominal frequency ω_o and the two inverters generate different power values $P_{grid(1)}$ and $P_{grid(2)}$. When the microgrid transfers to island mode (due to unintentional islanding) the island frequency ω_{island} deviates from its nominal value ω_o and inverters 1 and 2 generate $P_{island(1)}$ and $P_{island(2)}$, respectively. In this case, $P_{island(2)}$ is negative and hence inverter 2 is importing power. In the event of unintentional islanding and from (10), the system will have steady state frequency such as

$$\begin{aligned} \omega_{island} &= \omega_o^* - k_{\omega 1}P_1 + k_{\omega 1}P_1^* \\ &= \omega_o^* - k_{\omega 2}P_2 + k_{\omega 2}P_2^* \end{aligned} \tag{12}$$

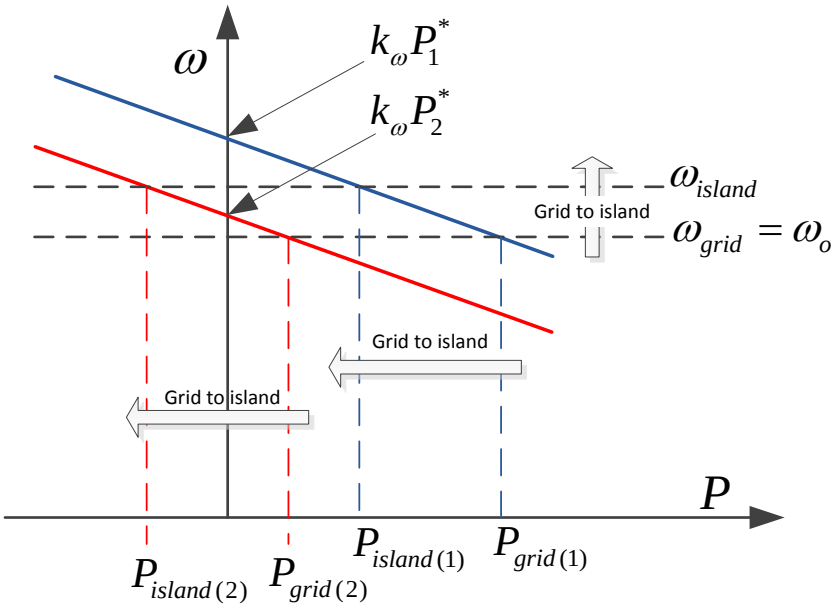

Figure 4.3. Droop control of two inverters in microgrid

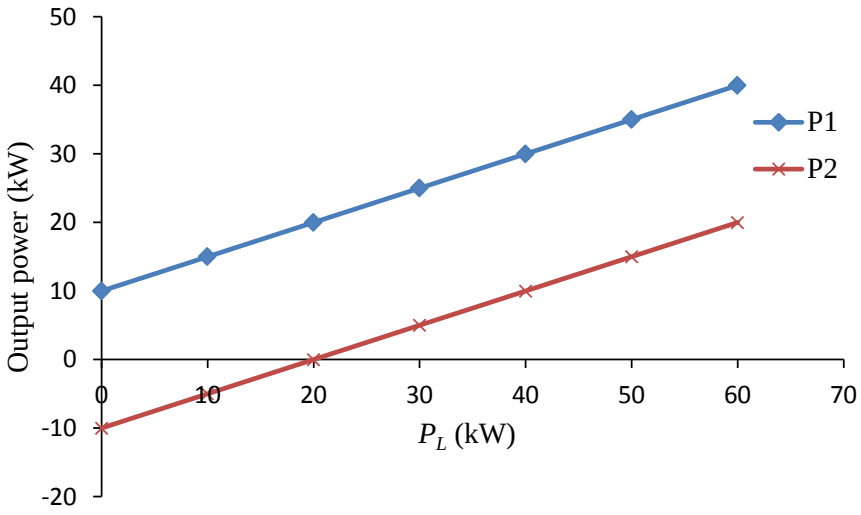

Figure 4.4. Output power versus load power, $P_1^* = 30kW$ and $P_2^* = 10kW$

Knowing that the two inverters have the same drooping gain $k_{\omega 1} = k_{\omega 2} = k_\omega$, (12) becomes

$$P_1 = P_1^* + P_2 - P_2^* \tag{13}$$

The total power dissipated by the load should equal the output power generated by the two inverters i.e.,

$$P_L = P_1 + P_2 \tag{14}$$

Substituting (13) and (14) in (12) the steady state island frequency is given by

$$\omega_{island} = \omega_o^* - \frac{k_\omega}{2}(P_L - P_1^* - P_2^*) \tag{15}$$

Equation (15) shows that the deviation from the nominal frequency depends on the local load and the power set-points of the inverters. Substituting, (14) in (13), the steady state output power of inverter 1 in island mode is given by

$$P_1 = \frac{1}{2}(P_L + P_1^* - P_2^*) \tag{16}$$

Similarly, the steady state output power of inverter 2 is given by

$$P_2 = \frac{1}{2}(P_L + P_2^* - P_1^*) \quad (17)$$

Equations (16) and (17) show that the two inverters will only share the load equally if $P_1^* = P_2^*$. They also show that if the load power is less than the difference between the two set-points, i.e.,

$$P_L < \left|P_1^* - P_2^*\right| \quad (18)$$

then one of the inverters will import power. Consider for example the case where $P_1^* = 30kW$ and $P_2^* = 10kW$, Figure 4.4 shows how the inverters output power varies with respect to local load. If islanding happens when the load is less than 20kW, i.e., $P_L < P_1^* - P_2^*$, the power output P_2 will be negative hence inverter 2 will import power. This power will cause the DC link voltage (see Figure 4.1) to rise and if the voltage exceeds the maximum allowed limit, the inverter will shut down. This phenomenon will reduce the reliability of the microgrid. In normal operation and after unintentional islanding is detected by the supervisory controller, a signal is sent to all inverters updating them with the status of the microgrid (grid-connected or stand-alone) so that the inverters local controller changes the set-points. However, this signal is sent via a relatively slow communication protocol (such as CAN-bus or Ethernet).

Regardless of the speed of the communication protocol, there can be some delay between when the islanding happens and until islanding is detected by the supervisory controller and an update signal is sent and received. During this transitional period, the dynamic of the microgrid is important in determining the amount of energy imported by an inverter.

4.3. Small Signal Model

In this section, a small signal model is developed to help analysing the system behaviour during unintentional islanding. The model will be developed for two inverters in island mode. The inverter can be modelled by a two-terminal Thevenin equivalent circuit as shown in Figure 4.5 where $G(s)$ and $Z_o(s)$ represent the closed loop and output impedance transfer functions, respectively [75].The response time of $G(s)$ is quite fast with respect to that of the outer droop control and hence it will be assumed as unity [8]. It is worth mentioning that all the harmonics have been neglected as it does not affect the calculated power.

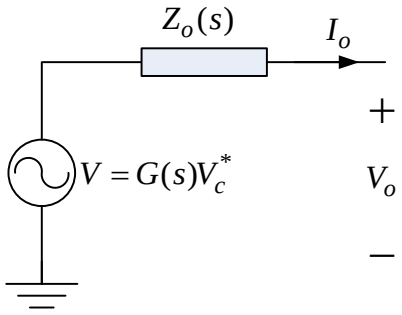

Figure 4.5. Inverter equivalent circuit at the fundamental frequency

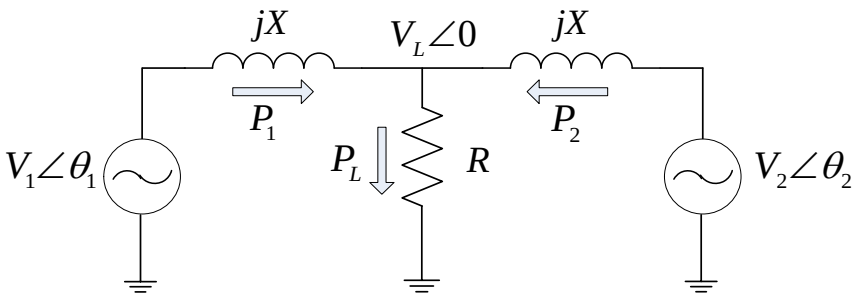

Figure 4.6. Equivalent circuit of two inverters in island mode at the fundamental frequency

The output impedance $Z_o(s)$ is predominantly inductive around the fundamental frequency [76],[77],[75] and hence $Z_o(s)$ can be approximated such as $Z_o(s) \approx s.L_o$. The inductance L_o can be determined by the slope of $Z_o(s)$ around the fundamental frequency and in the experimental setup used in this research it is 2500µH. Figure 4.6 shows the equivalent circuit for the two inverters operating in island mode. For simplicity, it is assumed that both inverters have identical output impedance $X = \omega L_o = 2\pi(50)L_o$ and they supply a local resistive load.

A. Power flow equations and power measurement

The current that flows from each inverter can be described as follows:

$$I_n = \frac{V_n \angle \theta_n - V_L}{X \angle 90}, \quad n = 1,2 \tag{19}$$

Applying Kirchhoff current law at the load node gives

$$\frac{V_L - V_1 \angle \theta_1}{X \angle 90} + \frac{V_L}{R} + \frac{V_L - V_2 \angle \theta_2}{X \angle 90} = 0 \tag{20}$$

Rearranging (20), the load voltage is given by

$$V_L = \frac{R(V_1 \angle \theta_1 + V_2 \angle \theta_2)}{2R + X \angle 90} \tag{21}$$

The apparent power of each inverter is given by

$$P_n + jQ_n = V_n . I_n^*, \quad n = 1,2 \tag{22}$$

Substituting (21) in (19) and the result into (22), the instantaneous active and reactive powers (in the time domain) for the two inverters are given by

$$P_1 = \frac{\frac{XV_1^2}{R} + 2V_1V_2\sin(\theta_1 - \theta_2) + \frac{XV_1V_2}{R}\cos(\theta_1 - \theta_2)}{4X + \frac{X^3}{R^2}} \quad (23)$$

$$Q_1 = \frac{(\frac{X^2}{R^2} + 2)V_1^2 - 2V_1V_2\cos(\theta_1 - \theta_2) + \frac{XV_1V_2}{R}\sin(\theta_1 - \theta_2)}{4X + \frac{X^3}{R^2}} \quad (24)$$

$$P_2 = \frac{\frac{XV_2^2}{R} + 2V_1V_2\sin(\theta_2 - \theta_1) + \frac{XV_1V_2}{R}\cos(\theta_2 - \theta_1)}{4X + \frac{X^3}{R^2}} \quad (25)$$

$$Q_2 = \frac{(\frac{X^2}{R^2} + 2)V_2^2 - 2V_1V_2\cos(\theta_2 - \theta_1) + \frac{XV_1V_2}{R}\sin(\theta_2 - \theta_1)}{4X + \frac{X^3}{R^2}} \quad (26)$$

When practically implementing the droop control, average active and reactive powers need to be measured and thus the droop control equations described in (10) and (11) become

$$\omega = \omega_o^* - k_\omega(P_{avg} - P^*) \quad (27)$$

$$V = V_o^* - k_a(Q_{avg} - Q^*) \quad (28)$$

The average power can be obtained by passing the instantaneous powers through a low pass filter. Hence, the average power P_{avg}, and Q_{avg} in the s-domain, are given by

$$P_{avg} = F(s)P(s) \quad (29)$$

$$Q_{avg} = F(s)Q(s) \quad (30)$$

where $P(s)$ and $Q(s)$ are the instantaneous active power and reactive power, respectively and described in equation (23)-(26). $F(s)$ is the transfer function of the LPF and is given by

$$F(s) = \frac{1}{\tau s + 1} \tag{31}$$

where τ is the filter time constant. Here τ is set to give fast response with little ripple.

B. State Space Equations

The state equation can be obtained by perturbing each state and calculating it in terms of other states and inputs. For instant, the output power perturbation of the first inverter (23) will be,

$$\begin{aligned} \Delta P_1 &= \frac{\partial P_1}{\partial V_1}\Delta V_1 + \frac{\partial P_1}{\partial V_2}\Delta V_2 + \frac{\partial P_1}{\partial \theta_1}\Delta\theta_1 + \frac{\partial P_1}{\partial \theta_2}\Delta\theta_2 \\ &= a_1\Delta V_1 + b_1\Delta V_2 + c_1\Delta\theta_1 + d_1\Delta\theta_2 \end{aligned} \tag{32}$$

By perturbing other power flow equations (24)–(26) we obtain,

$$\Delta P_2 = a_2\Delta V_1 + b_2\Delta V_2 + c_2\Delta\theta_1 + d_2\Delta\theta_2 \tag{33}$$

$$\Delta Q_1 = a_3\Delta V_1 + b_3\Delta V_2 + c_3\Delta\theta_1 + d_3\Delta\theta_2 \tag{34}$$

$$\Delta Q_2 = a_4\Delta V_1 + b_4\Delta V_2 + c_4\Delta\theta_1 + d_4\Delta\theta_2 \tag{35}$$

where Δ means a small perturbation around the equilibrium points ($V_{1eq}, V_{2eq}, \theta_{1eq}, \theta_{2eq}$). The coefficients a,b,c,d (with the different subscripts) are obtained by calculating the corresponding partial derivatives and they are given in (36).

$$a_1 = \frac{\partial P_1}{\partial V_1} = \frac{2\frac{X}{R}V_{1eq} + 2V_{2eq}\sin(\theta_{1eq} - \theta_{2eq}) + \frac{X}{R}V_{2eq}\cos(\theta_{1eq} - \theta_{2eq})}{M}$$

$$b_1 = \frac{\partial P_1}{\partial V_2} = \frac{2V_{1eq}\sin(\theta_{1eq} - \theta_{2eq}) + \frac{X}{R}V_{1eq}\cos(\theta_{1eq} - \theta_{2eq})}{M}$$

$$c_1 = \frac{\partial P_1}{\partial \theta_1} = \frac{2V_{1eq}V_{2eq}\cos(\theta_{1eq} - \theta_{2eq}) - \frac{X}{R}V_{1eq}V_{2eq}\sin(\theta_{1eq} - \theta_{2eq})}{M}$$

$$d_1 = \frac{\partial P_1}{\partial \theta_2} = -c_1$$

$$a_2 = \frac{\partial P_2}{\partial V_1} = \frac{2V_{2eq}\sin(\theta_{2eq} - \theta_{1eq}) + \frac{X}{R}V_{2eq}\cos(\theta_{2eq} - \theta_{1eq})}{M}$$

$$b_2 = \frac{\partial P_2}{\partial V_2} = \frac{2\frac{X}{R}V_{2eq} + 2V_{1eq}\sin(\theta_{2eq} - \theta_{1eq}) + \frac{X}{R}V_{1eq}\cos(\theta_{2eq} - \theta_{1eq})}{M} \qquad (36)$$

$$c_2 = \frac{\partial P_2}{\partial \theta_1} = \frac{-2V_{1eq}V_{2eq}\cos(\theta_{2eq} - \theta_{1eq}) + \frac{X}{R}V_{1eq}V_{2eq}\sin(\theta_{2eq} - \theta_{1eq})}{M}$$

$$d_2 = \frac{\partial P_2}{\partial \theta_2} = -c_2$$

$$a_3 = \frac{\partial Q_1}{\partial V_1} = \frac{2(\frac{X^2}{R^2} + 2)V_{1eq} - 2V_{2eq}\cos(\theta_{1eq} - \theta_{2eq}) + \frac{X}{R}V_{2eq}\sin(\theta_{1eq} - \theta_{2eq})}{M}$$

$$b_3 = \frac{\partial Q_1}{\partial V_2} = \frac{-2V_{1eq}\cos(\theta_{1eq} - \theta_{2eq}) + \frac{X}{R}V_{1eq}\sin(\theta_{1eq} - \theta_{2eq})}{M}$$

$$c_3 = \frac{\partial Q_1}{\partial \theta_1} = \frac{2V_{1eq}V_{2eq}\sin(\theta_{1eq} - \theta_{2eq}) + \frac{X}{R}V_{1eq}V_{2eq}\cos(\theta_{1eq} - \theta_{2eq})}{M}$$

$$d_3 = \frac{\partial Q_1}{\partial \theta_2} = -c_3$$

$$a_4 = \frac{\partial Q_2}{\partial V_1} = \frac{-2V_{2eq}\cos(\theta_{2eq} - \theta_{1eq}) + \frac{X}{R}V_{2eq}\sin(\theta_{2eq} - \theta_{1eq})}{M}$$

$$b_4 = \frac{\partial Q_2}{\partial V_2} = \frac{2(\frac{X^2}{R^2} + 2)V_{2eq} - 2V_{1eq}\cos(\theta_{2eq} - \theta_{1eq}) + \frac{X}{R}V_{1eq}\sin(\theta_{2eq} - \theta_{1eq})}{M}$$

$$c_4 = \frac{\partial Q_2}{\partial \theta_1} = \frac{-2V_{1eq}V_{2eq}\sin(\theta_{2eq} - \theta_{1eq}) - \frac{X}{R}V_{1eq}V_{2eq}\cos(\theta_{2eq} - \theta_{1eq})}{M}$$

$$d_4 = \frac{\partial Q_2}{\partial \theta_2} = -c_4$$

where $M = 4X + \frac{X^3}{R^2}$

By perturbing (27) and (28) we obtain,

$$\Delta\omega_n = -k_\omega \Delta P_{avgn} \tag{37}$$

$$\Delta V_n = -k_a \Delta Q_{avgn} \tag{38}$$

where *n*=1, 2, …. is the inverter's number. Substituting (31) in (29) and (30) the average power is related to the instantaneous power by

$$\Delta P_{avgn} = \frac{1}{\tau s + 1}\Delta P_n \tag{39}$$

$$\Delta Q_{avgn} = \frac{1}{\tau s + 1}\Delta Q_n \tag{40}$$

Substituting (32) in (39) and rearranging gives,

$$s.\Delta P_{avgn} = \frac{1}{\tau}(a_n\Delta V_1 + b_n\Delta V_2 + c_n\Delta\theta_1 + d_n\Delta\theta_2) - \frac{1}{\tau}\Delta P_{avgn} \qquad n = 1,2 \tag{41}$$

Substituting (34) in (40) and rearranging gives

$$s.\Delta Q_{avgn} = \frac{1}{\tau}(a_{n+2}\Delta V_1 + b_{n+2}\Delta V_2 + c_{n+2}\Delta\theta_1 + d_{n+2}\Delta\theta_2) - \frac{1}{\tau}\Delta Q_{avgn} \qquad n = 1,2 \tag{42}$$

The inverter power angle is related to the frequency by,

$$s\Delta\theta_n = \Delta\omega_n, \qquad n = 1,2 \tag{43}$$

Equations (32)-(43) can be combined into a homogenous state space equation such as,

$$[sX_1]=[A_1][X_1] \tag{44}$$

where [X] contains the state variables and is given by

$$[X_1]=\begin{bmatrix} \Delta\theta_1 \\ \Delta\theta_2 \\ \Delta\omega_1 \\ \Delta\omega_2 \\ \Delta V_1 \\ \Delta V_2 \\ \Delta P_{avg1} \\ \Delta P_{avg2} \\ \Delta Q_{avg1} \\ \Delta Q_{avg2} \end{bmatrix}$$

The state variable matrix $[A_1]$ is given in (45). Thus, equation (44) represents a state space model of the two inverters in island mode.

$$[A_1]=\begin{bmatrix} 0 & 1 & 0 & 0 & 0 & 0 & 0 & 0 & 0 & 0 \\ 0 & 0 & 0 & 1 & 0 & 0 & 0 & 0 & 0 & 0 \\ -\frac{k_\omega.c_1}{\tau} & -\frac{k_\omega.d_1}{\tau} & -\frac{1}{\tau} & 0 & -\frac{k_\omega.a_1}{\tau} & -\frac{k_\omega.b_1}{\tau} & 0 & 0 & 0 & 0 \\ -\frac{k_\omega.c_2}{\tau} & -\frac{k_\omega.d_2}{\tau} & 0 & -\frac{1}{\tau} & -\frac{k_\omega.a_2}{\tau} & -\frac{k_\omega.b_2}{\tau} & 0 & 0 & 0 & 0 \\ -\frac{k_a.c_3}{\tau} & -\frac{k_a.d_3}{\tau} & 0 & 0 & -\frac{(1+k_a.a_3)}{\tau} & -\frac{k_a.b_3}{\tau} & 0 & 0 & 0 & 0 \\ -\frac{k_a.c_4}{\tau} & -\frac{k_a.d_4}{\tau} & 0 & 0 & -\frac{k_a.a_4}{\tau} & -\frac{(1+k_a.b_4)}{\tau} & 0 & 0 & 0 & 0 \\ \frac{c_1}{\tau} & \frac{d_1}{\tau} & 0 & 0 & \frac{a_1}{\tau} & \frac{b_1}{\tau} & \frac{-1}{\tau} & 0 & 0 & 0 \\ \frac{c_2}{\tau} & \frac{d_2}{\tau} & 0 & 0 & \frac{a_2}{\tau} & \frac{b_2}{\tau} & 0 & \frac{-1}{\tau} & 0 & 0 \\ \frac{c_3}{\tau} & \frac{d_3}{\tau} & 0 & 0 & \frac{a_3}{\tau} & \frac{b_3}{\tau} & 0 & 0 & \frac{-1}{\tau} & 0 \\ \frac{c_4}{\tau} & \frac{d_4}{\tau} & 0 & 0 & \frac{a_4}{\tau} & \frac{b_4}{\tau} & 0 & 0 & 0 & \frac{-1}{\tau} \end{bmatrix} \tag{45}$$

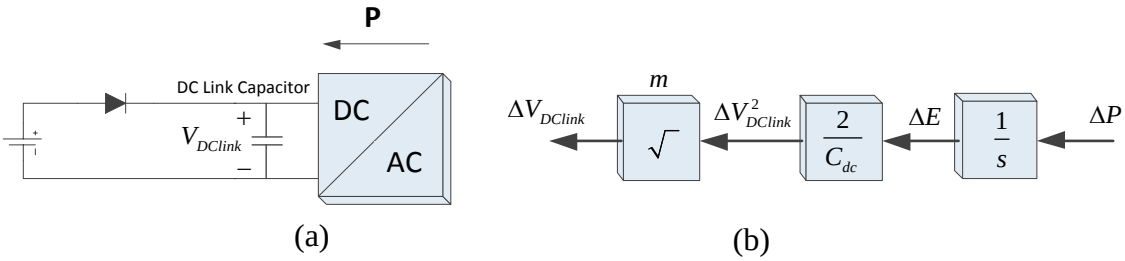

Figure 4.7. DC link capacitor (a) when DC/AC inverter is importing power, (b) small signal model.

4.4. DC Link Voltage Controller

A. DC link modelling

As explained earlier, the imported power may raise the DC link voltage to an unacceptable limit. In this section, the state space model developed in section 4.3. will be extended to include the DC link voltage.

Figure 4.7(a) shows the DC link capacitor when the inverter is importing power during the transient period. The energy E absorbed by the capacitor is related to the capacitor voltage V_{DClink} by,

$$E = \int P(t)dt = \frac{1}{2}C_{dc}V_{DClink}^2 \tag{46}$$

where P is the instantaneous absorbed power and C_{DC} is the DC link capacitance. In order to have a linear relationship between ΔP and ΔV_{DClink}, the square root relation needs to be linearized. Let $x = V_{DClink}^2$ and $(x) = \sqrt{x}$, small change in y is given by:

$$\Delta y = \Delta x . \left.\frac{dy}{dx}\right|_{x=x_o} \tag{47}$$

where Δx is a small change in Δx and x_o is the equilibrium point. Given that the DC link voltage needs to be around x_o, Δy becomes

$$\Delta y = m.\Delta x \tag{48}$$

where $m = \left.\frac{dy}{dx}\right|_{x=x_o} = \left.\frac{1}{2\sqrt{x}}\right|_{x=X_o^2}$

Therefore, as shown in Figure 4.7(b), the linear relationship between the DC link voltage and the power is given by

$$\Delta V_{DClinkn} = \frac{2m}{C_{dc}s}.\Delta P_n \tag{49}$$

Substituting (32) and (33) in (49) gives the state equation for $\Delta V_{DClink1}$ and $\Delta V_{DClink2}$. This can then be combined with (44) to give (50) such as

$$[\mathrm{sX}_2] = [\mathrm{A}_2][\mathrm{X}_2] \tag{50}$$

where,

$$[\mathrm{X}_2] = \begin{bmatrix} \mathrm{X}_1 \\ \Delta V_{DClink1} \\ \Delta V_{DClink2} \end{bmatrix}$$

$$[\mathrm{A}_2] = \begin{bmatrix} \mathrm{A}_1 & [0]_{10\times 2} \\ \mathrm{A}_3 & [0]_{2\times 2} \end{bmatrix}$$

where A_3 is,

$$[\mathrm{A}_3] = \begin{bmatrix} \frac{2mc_1}{C_{dc}} & \frac{2md_1}{C_{dc}} & 0 & 0 & \frac{2ma_1}{C_{dc}} & \frac{2mb_1}{C_{dc}} & 0 & 0 & 0 & 0 & 0 & 0 & 0 & 0 \\ \frac{2mc_2}{C_{dc}} & \frac{2md_2}{C_{dc}} & 0 & 0 & \frac{2ma_2}{C_{dc}} & \frac{2mb_2}{C_{dc}} & 0 & 0 & 0 & 0 & 0 & 0 & 0 & 0 \end{bmatrix} \tag{51}$$

Equation (50) represents the state space equation for the complete model of the two inverters in island mode including the dynamics of the DC link voltages.

B. Design of DC link voltage controller to limit transient power

In this section, a controller is proposed to limit the amount of imported power during the transitional period so the inverters carry on working without interruption until they receive the update signal from the supervisory controller as explained earlier. The controller reduces the power set-points if the DC link voltage exceeds a certain limit. The proposed controller is illustrated in Figure 4.8.

During normal operation when the power flows out of the inverter, the DC link voltage is regulated by a DC/DC boost converter. The reference V^*_{DCLink} is the nominal DC voltage such that it only becomes effective if the DC link voltage exceeds a threshold which means the inverter is importing power. In this case, the controller will change the reference power set-point until the DC voltage difference is minimized.

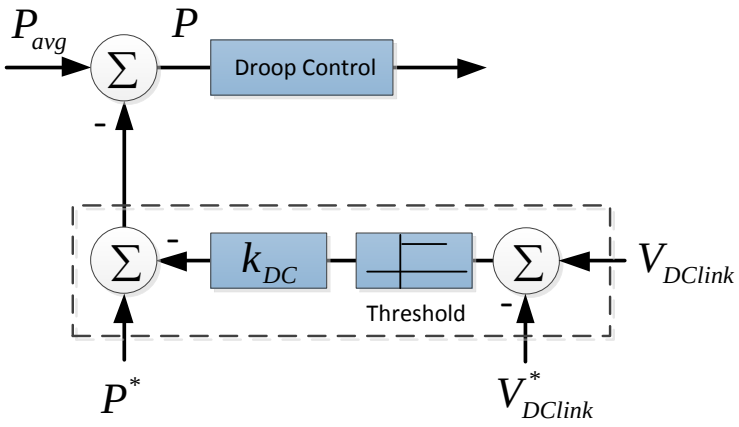

Figure 4.8. Proposed Controller based on DC link voltage

The controller gain k_{DC} must be selected carefully to guarantee good stability and good reduction in imported energy. In order to analyse stability, the small signal model described by (50) will be slightly modified to include the DC link voltage controller. If the proposed controller is implemented for inverter 1, from Figure 4.8 we can write,

$$P = P_{avg1} - P^* + k_{DC}(V_{DClink1} - V^*_{DClink1}) \tag{52}$$

By perturbing (52) around the equilibrium points we get:

$$\Delta P = \Delta P_{avg1} + k_{DC}\Delta V_{DClink1} \tag{53}$$

Substituting (53) in (37) gives,

$$\Delta\omega = -k_{\omega}(\Delta P_{avg1} + k_{DC}\Delta V_{DClink1}) \tag{54}$$

The state variable "$s.\Delta\omega$" becomes

$$s\Delta\omega = -k_{\omega}s\Delta P_{avg1} - k_{\omega}k_{DC}s\Delta V_{DClink1} \tag{55}$$

The state space equation of (50) can be modified to include this control loop. It can be done by modifying the 3rd row of the state matrix of A_2 according to (55). If the controller is implemented for inverter 2 then the 4th row of A_2 is also modified.

In order to analyse the effect of k_{DC} on the system stability, the locus of the eigenvalues of A_2 is plotted as shown in Figure 4.9. The eigenvalues of the system are plotted for $0 < k_{DC} < 10$. They are in the left half plane for the selected gain range. The arrows depict the evolution of the eigenvalues when the gain value increases, which show that the system becomes faster with higher overshoot by increasing the gain since the complex poles become the

dominant poles whilst the effect of the real poles decreases, which exposing more oscillation and even instability if it is quite high.

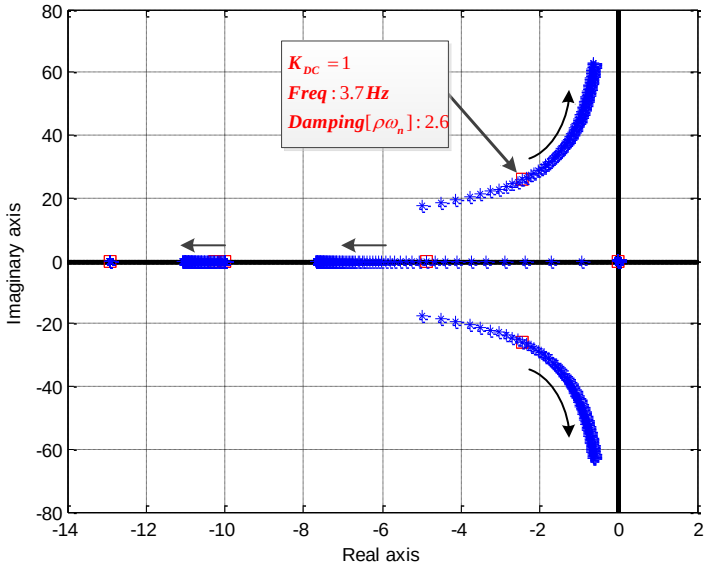

Figure 4.9. Root locus of the system when $0 < k_{DC} < 10$

Symbol	Description	Value
P_1^*	Active Power set-point for inverter 1	20 W
P_2^*	Active Power set-point for inverter 2	0 W
Q_1^*	Reactive Power set-point for inverter 1	0 VAR
Q_2^*	Reactive Power set-point for inverter 2	0 VAR
P_L	Load power	0
L_o	Inverter output inductance (small signal and detailed simulation model)	2500 µH
k_ω	Frequency drooping gain	0.05 rad/s/W
k_a	Voltage drooping gain	0.01 V/Var
V_o	Voltage set point	23 Vrms
f_o	Frequency set point	50 Hz
τ	Measurement filter time constant	0.1 sec
V_{DClink}^*	Nominal DC link voltage	40 V
$V_{DClink\_max}^*$	Maximum DC link voltage	120 V
m	Linearization factor relating V_{DClink}^2 to V_{DClink}	0.0125

Table 4.2 Simulation and Experimental Parameters

Increasing the gain k_{DC} decreases the absorbed energy and so the DC voltage is minimized. However, it will increase the oscillatory components resulting in higher overshoot. Thus, by choosing k_{DC} equal to 1, a compromise between stability and absorbed energy is achieved.

4.5. Simulation and Experimental Results

The simulation results of the state space model developed earlier are compared with that of a detailed model developed using Matlab/SimPowerSystems and the results obtained from an experimental setup. The two inverters have been modelled as ideal voltage sources in Simulink as shown in Figure 4.6. The simulation parameters are shown in Table 4.2. A laboratory-scale microgrid, where the AC voltages and power ratings are scaled down by a factor of 10, was built as in Chapter 3. In addition, setup parameters are listed in Table 4.2.

State Variable	X_{eq}	**Case 1 (starting in island mode)**		**Case 2 (unintentional islanding)**	
		$X(0)$	$\Delta X(0)$	$X(0)$	$\Delta X(0)$
$\Delta\theta_1$	0.019 rad	0 rad	-0.019 rad	0.034 rad	0.015 rad
$\Delta\theta_2$	-0.019 rad	0 rad	0.019 rad	-0.004 rad	0.015 rad
$\Delta\omega_1$	314.66 rad/s	315.16 rad/s	0.5 rad/s	314.16 rad/s	-0.5 rad/s
$\Delta\omega_2$	314.66 rad/s	314.16 rad/s	-0.5 rad/s	314.16 rad/s	-0.5 rad/s
ΔV_1	23 Vrms	23 Vrms	0	23 Vrms	0
ΔV_2	23 Vrms	23 Vrms	0	23 Vrms	0
ΔP_{avg1}	10W	0	-10 W	20 W	10 W
ΔP_{avg2}	-10W	0	10 W	0 W	10 W
ΔQ_{avg1}	0	0	0	0	0
ΔQ_{avg2}	0	0	0	0	0

Table 4.3 Equilibrium points and initial deviations for the small signal model

A. Initial Conditions for the state space model

Two cases will be considered to validate the state space model: In case 1, two inverters are started in island mode with different power set-points. Even though this case is not practical, as the supervisory controller should set the power set-points equally before starting the inverters, it provides a good test for validating the small signal model. Case 2: represents unintentional islanding when the two inverters have different set points. Each state variable of the small signal model described in (44) represents the deviation $\Delta x(t)$ from the equilibrium point x_{eq}. The time domain response $x(t)$ is calculated by adding the deviation to the equilibrium point such as

$$x(t) = x_{eq} + \Delta x(t) \tag{56}$$

The equilibrium points are calculated as follows: the average power equilibrium points are calculated using (16) and (17). The frequency equilibrium point is calculated using (15). The angle equilibrium point can be calculated using (57) which relates the active power transferred from each inverter to the load node

$$P_n = \frac{V_n V_L \sin(\theta_n)}{X}, \quad n = 1,2 \tag{57}$$

All equilibrium points are listed in Table 4.3. The initial deviations from the equilibrium points $\Delta x(0)$ are calculated using (58) such as

$$\Delta x(0) = x(0) - x_{eq} \tag{58}$$

where $x(0)$ represents the initial condition at the beginning of the simulations. In case 1, $x(0)$ are the initial conditions at rest before starting the inverters. In case 2, however, $x(0)$ represents the initial condition in grid-connected mode

just before the unintentional islanding. All the initial conditions and initial deviations are calculated for both cases and listed in Table 4.3.

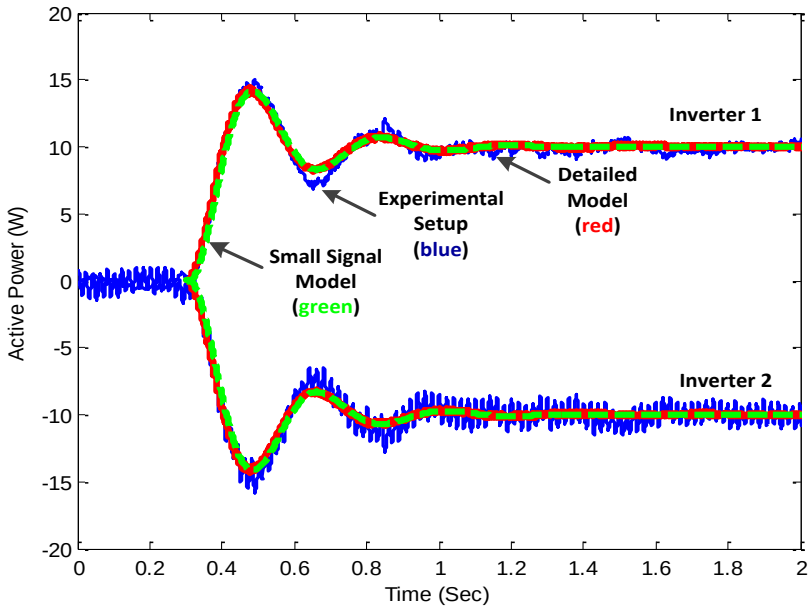

Figure 4.10. Average measured active power of inverters 1 and 2 in island mode (case 1)

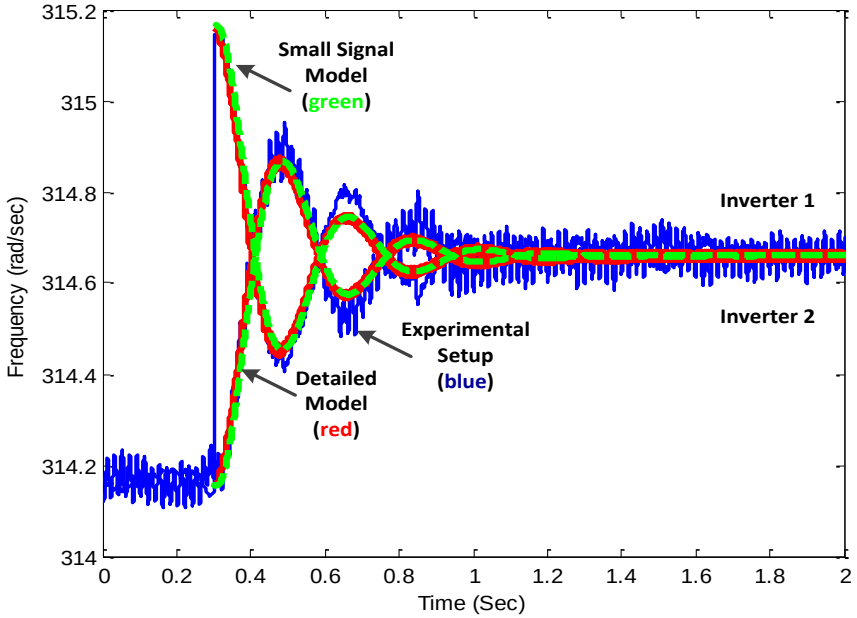

Figure 4.11. Frequency of inverters 1 and 2 in island mode (case 1)

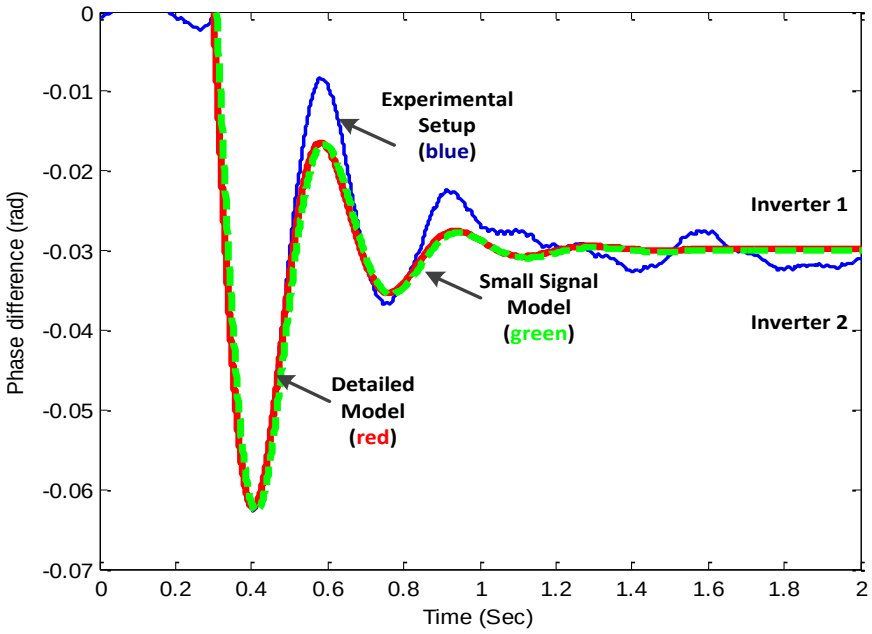

Figure 4.12. Phase of inverters 1 and 2 in island mode (case 1)

B. Validation of the small signal model

Results of case 1

Figure 4.10 depicts the average active power for both inverters under case 1 conditions. The figure includes the results obtained from the small signal model, the detailed Simulink model and the experimental setup. As can be seen, the small signal model is in complete agreement with the detailed model and both agree with the experimental results. A similar conclusion can be obtained from Figure 4.11 and Figure 4.12 which show the response of the frequency and phase angle, respectively.

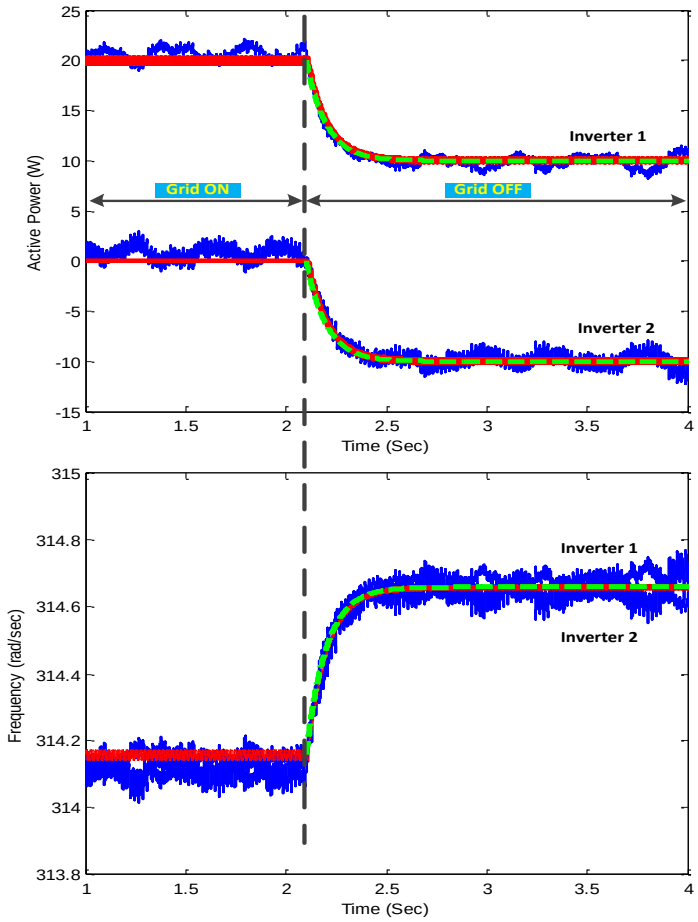

Figure 4.13. Average measured active power (above) and frequency (below) of inverters 1 and 2 after grid loss- unintentional islanding (case 2)

Results of case 2

In this case, the two inverters are initially operating in grid connected mode. At time t = 2.1 seconds, the grid is isolated so the two inverters operate in island mode. Figure 4.13 shows the responses of the average active power (instantaneous power after being filtered by the LPF) of both inverters using the detailed and the small signal model and the experimental setup. Again, the responses dynamics are all in full agreement. Figure 4.13 also shows the

frequency responses of both inverters. The behaviour of the second inverter, which is importing 10W, develops high voltage across the DC link capacitor resulting in a power trip as shown in Figure 4.14, which depicts the experimental DC link voltage of inverter 2 before and after islanding. When the DC link exceeds the max limit, a trip signal is generated.

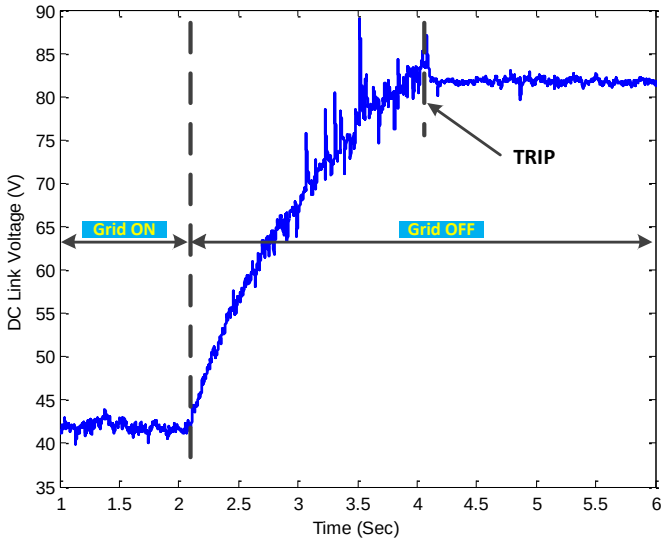

Figure 4.14. DC Link voltage across the capacitor of inverter 2

C. Results of the proposed DC Controller

Figure 4.15 shows the simulation and experimental results of the unintentional islanding case (case 2) with $P_L = 0$. The first inverter was generating 20W while the second inverter was generating 0W in grid-connected mode. When the islanding occurs at t=3 sec the output powers become $P_1 = 10W$ and $P_2 = -10W$ which agree with (16) and (17). The DC link voltage of inverter 2 starts to rise, and when it reaches 100V the DC Link controller is activated. The active powers are then reduced to zero and the dc voltage is reduced to 50V. The

charging time in simulation and practical results are slightly different since knowledge of the dynamics of the DC source (applied on the DC link capacitor) is beyond the scope of this research. In addition, considering an ideal AC voltage source instead of the full dynamics of the inverter as stated previously, results in that the simulated DC value is a calculated value not a measured one. The effectiveness of the proposed controller is clear, as it has prevented the DC link voltage from reaching the trip limit by quickly adjusting the power demand and the inverters kept working waiting for an update signal to be received from the supervisory controller.

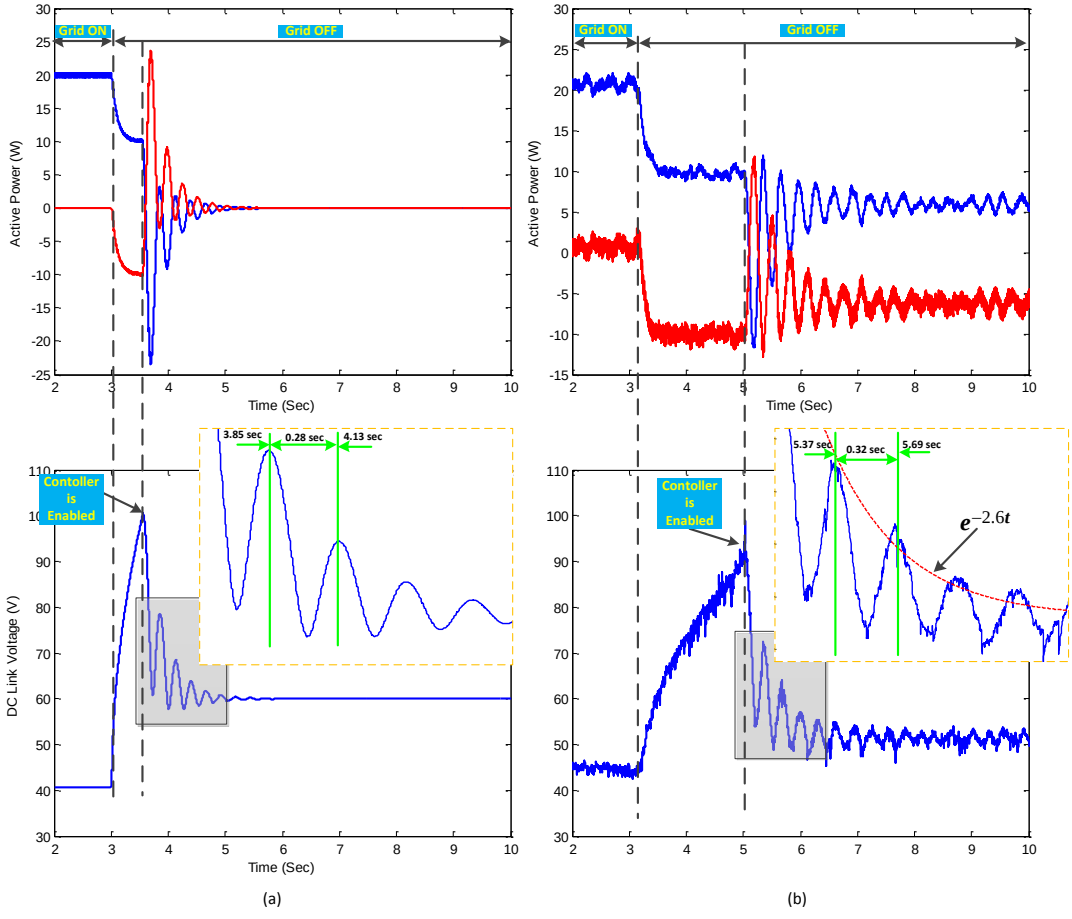

Figure 4.15. Average measured active power of both inverters and DC link voltage of inverter 2 with proposed controller ($k_{DC} = 1$) (a) Simulink detailed model, (b) experimental setup

According to the eigenvalues of the DC link controller of Figure 4.9, the predicted transient response of the dc voltage is $c(t) = e^{-2.6t}\sin(2\pi 3.7t)$ for $k_{DC} = 1$. The magnified portion in Figure 4.15 shows the transient oscillation of the dc voltage. The oscillation frequencies of the detailed model and the experimental setup are 3.57Hz and 3.125Hz, respectively. The small signal model has provided good prediction of the transient response. The exponential decaying term also agrees with the eigenvalues of Figure 4.9.

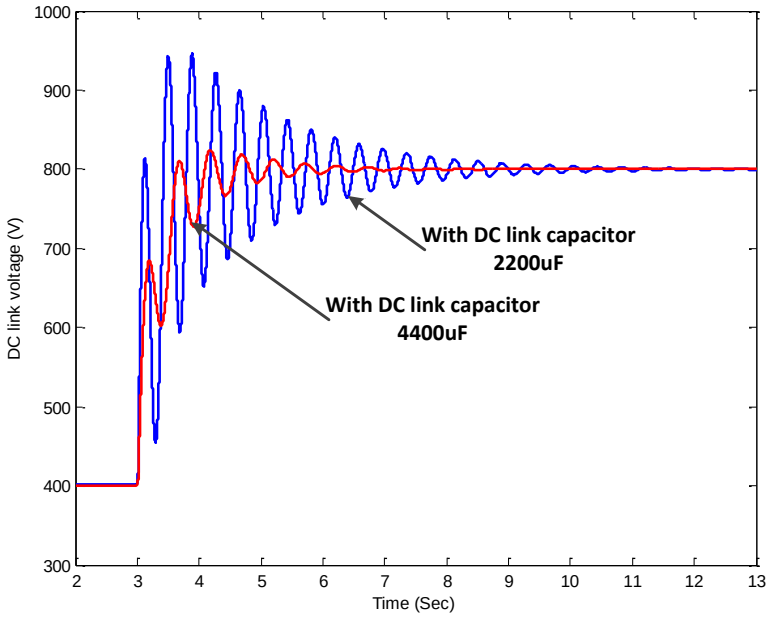

Figure 4.16. DC link voltage responses in case of different values of DC link capacitor

To test the controller at high voltages and power, Figure 4.16 shows the simulation results of unintentional islanding of two inverters operating at high voltages (nominal AC voltage V_o = 230Vrms and nominal DC link voltage V^*_{Dclink} = 400V). One inverter was injecting 10kW and the second inverter was injecting 0kW into the grid before islanding. The simulation is carried out for two different

values of DC link capacitance (2200μF and 4400μF). As expected from equation (49), the DC link voltage peak deviation is inversely proportional to the capacitance value but in both cases the controller was able to prevent the DC link voltage from reaching the trip limit of 1000V. The response with the low value of DC link capacitance is quite oscillatory. Choosing a larger capacitance value will give better transient response but it will also increase cost, size and losses.

Choosing a smaller capacitance value can either lead to instability (if a high k_{DC} value is used) or failure to prevent the DC link from reaching the trip limit. It is worth mentioning here that the DC link capacitance value has traditionally been selected to satisfy certain requirements such as limiting the AC voltage ripple when the inverter is fed from a rotational machine plus rectifier or to decouple the inverter power stage from the driving prime mover stage. However, if the inverter is to be used in a microgrid, the effect of unintentional islanding on the rise of DC link voltage needs to be taken into account when selecting the DC link capacitance.

4.6. Proposed controller for a Multi-inverter microgrid

The study of the aforementioned problem in this chapter based on a microgrid containing multi-inverter units is important; particularly the general structure of the majority of microgrids consists of many parallel inverters. The expected behaviour of the DC link voltage of one inverter importing power from many other inverters will have a fast rising and short time for the controller to act, particularly, if the value of the capacitor is not very high. This work exposes new

challenges in terms of modelling and practical implementation. However, in this section, a small signal model of a multi-inverter three phase island microgrid will be developed based on dq-frame and evaluated the model by simulation without validating it practically as the laboratory capability is limited. Moreover, by means of the same strategy as in the previous sections, the states of the DC link voltages will be incorporated in the model and a controller will be applied to limit the DC voltage rise in any unit.

4.6.1. Island Microgrid Modelling

The model developed in [45] included the inner voltage and current controller loop but it was concluded that the outer power sharing loop dominates the effect on stability. In addition, in [78], Iyer et al. assumed that the dynamics of the inner voltage and current loops can be neglected as their bandwidths are much higher than the outer droop controller loop due to the low pass filter used to average the active and reactive powers. Thus, in Figure 4.17, the dynamics of the inner voltage and current controller loops are neglected and later the microgrid model will be divided into subsystems and re-constructed into one state-space model.

Figure 4.17 shows a microgrid model in island mode. The model contains g parallel inverters modelled as an ideal voltage sources with equivalent output impedance. Each inverter has its own power sharing loop. The network of m distribution lines and l loads elements are also included.

Each inverter has two cascaded sub-state space models. The first model is for the power sharing controller while the second one is the output impedance model. The derived model is based on dq-frame so voltage and current states need to be converted from abc to dq-frame.

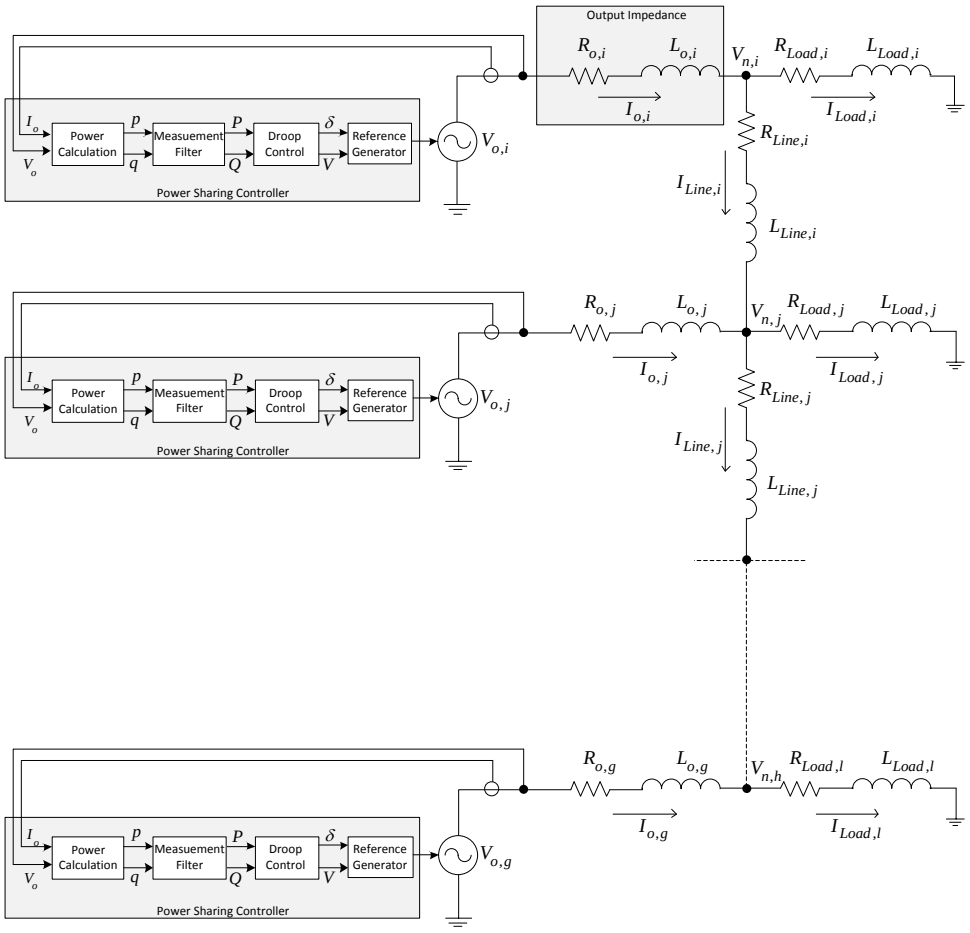

Figure 4.17. Multi-inverter island microgrid

A. Power sharing loop model

The instantaneous output power of each inverter can be calculated as,

$$p_{ins} = \frac{3}{2}(v_{od} i_{od} + v_{oq} i_{oq})$$
$$q_{ins} = \frac{3}{2}(v_{od} i_{oq} - v_{oq} i_{od}) \quad (59)$$

These calculated powers should pass through a low pass filter to cancel out high frequency components and ripples. The averaged power is given by,

$$P = \frac{\omega_c}{s + \omega_c} p_{ins}$$
$$Q = \frac{\omega_c}{s + \omega_c} q_{ins} \quad (60)$$

As the d-component is chosen to align phase A voltage in a three phase system, the q-component will equal zero and then the adopted droop control for each unit to share the power in dq-frame is,

$$\omega = \omega_o^* - m_p P$$
$$v_{od} = V_o^* - n_q Q \quad (61)$$
$$v_{oq} = 0$$

where ω_o^*, V_o^* are the nominal frequency and nominal voltage references, m_p, and n_q are the proportional frequency drooping coefficient, and proportional voltage drooping coefficient, respectively. To construct the small signal model, the variables in (61) should be perturbed around the equilibrium points. Equation (62) depicts the linearization of power calculation equations in (59).

$$\Delta p_{ins} = I_{od}.\Delta v_{od} + I_{oq}.\Delta v_{oq} + V_{od}.\Delta i_{od} + V_{oq}.\Delta i_{oq}$$
$$\Delta q_{ins} = I_{oq}.\Delta v_{od} - I_{od}.\Delta v_{oq} - V_{oq}.\Delta i_{od} + V_{od}.\Delta i_{oq} \quad (62)$$

where V_{od}, V_{oq}, I_{od}, I_{oq} are the equilibrium points for the output voltage and current. The symbol "Δ" denotes a small signal variation in a state.

Applying small signal variations on (60) and (61) gives,

$$
\begin{aligned}
s\Delta P &= \omega_c \Delta p_{ins} - \omega_c \Delta P \\
s\Delta Q &= \omega_c \Delta q_{ins} - \omega_c \Delta Q \\
\\
\Delta\omega &= -m_p \Delta P \\
\Delta v_{od} &= -n_q \Delta Q \\
\Delta v_{oq} &= 0
\end{aligned}
\tag{63}
$$

and the phase state of any inverter could be calculated as,

$$s\Delta\delta = \Delta\omega \tag{64}$$

The phase state assumes a fixed frequency at the PCC. This could be valid in grid-connected mode with a stiff grid. However, in island mode, the common frequency throughout the system might have small deviations. To take that into account, equation (64) is updated to be,

$$s\Delta\delta = \Delta\omega - \Delta\omega_{com} \tag{65}$$

where $\Delta\omega_{com}$ is a small variation of the common frequency of the system. This will be utilized also, in Part C, to transform any inverter state from its local frame to a common frame to couple all the subsystems together in one system.

By arranging the results of (62), (63) and (65), then the sub-state space model of the small signal representation of the droop control is derived as (66) where $\Delta\delta, \Delta P, \Delta Q, \Delta i_{odq}, \Delta v_{odq}, \Delta\omega$ are small deviations in the phase, averaged active power, averaged reactive power, output current, output voltage and frequency, respectively, and the symbol [$\dot{}$] denotes the state equation.

$$\begin{bmatrix}\dot{\Delta\delta}\\ \Delta P\\ \Delta Q\end{bmatrix} = A_P\begin{bmatrix}\Delta\delta\\ \Delta P\\ \Delta Q\end{bmatrix} + B_{Pv}\begin{bmatrix}\Delta v_{od}\\ \Delta v_{oq}\end{bmatrix} + B_{Pi}\begin{bmatrix}\Delta i_{od}\\ \Delta i_{oq}\end{bmatrix} + B_{P\omega com}\left[\Delta\omega_{com}\right]$$

$$\left[\Delta\omega\right] = C_{P\omega}\begin{bmatrix}\Delta\delta\\ \Delta P\\ \Delta Q\end{bmatrix},$$

$$\begin{bmatrix}\Delta v_{od}\\ \Delta v_{oq}\end{bmatrix} = C_{Pv}\begin{bmatrix}\Delta\delta\\ \Delta P\\ \Delta Q\end{bmatrix}, C_P = \begin{bmatrix}C_{P\omega}\\ C_{Pv}\end{bmatrix} \quad (66)$$

$$A_P = \begin{bmatrix}0 & -m_p & 0\\ 0 & -\omega_c & 0\\ 0 & 0 & -\omega_c\end{bmatrix},$$

$$B_{Pv} = \begin{bmatrix}0 & 0\\ 1.5\omega_c.I_{od} & 1.5\omega_c.I_{oq}\\ 1.5\omega_c.I_{oq} & -1.5\omega_c.I_{od}\end{bmatrix}, B_{Pi} = \begin{bmatrix}0 & 0\\ 1.5\omega_c.V_{od} & 1.5\omega_c.V_{oq}\\ -1.5\omega_c.V_{oq} & 1.5\omega_c.V_{od}\end{bmatrix}, B_{P\omega com} = \begin{bmatrix}-1\\ 0\\ 0\end{bmatrix},$$

$$C_{P\omega} = \begin{bmatrix}0 & -m_p & 0\end{bmatrix}, C_{Pv} = \begin{bmatrix}0 & 0 & -n_q\\ 0 & 0 & 0\end{bmatrix}$$

B. Output impedance model

The output impedance model is a simple RL network between two voltage nodes where the output current is assigned to be out of the inverter. The source voltage node is v_o and the sink voltage node is v_n. The sub-state space model in terms of the output current state is,

$$\begin{bmatrix}\dot{\Delta i}_{od}\\ \Delta i_{oq}\end{bmatrix} = A_Z\begin{bmatrix}\Delta i_{od}\\ \Delta i_{oq}\end{bmatrix} + B_{Z1}\begin{bmatrix}\Delta\omega\\ \Delta v_{od}\\ \Delta v_{oq}\end{bmatrix} + B_{Z2}\begin{bmatrix}\Delta v_{nd}\\ \Delta v_{nq}\end{bmatrix} \quad (67)$$

$$A_Z = \begin{bmatrix}-R_o/L_o & \omega_o\\ -\omega_o & -R_o/L_o\end{bmatrix}, B_{Z1} = \begin{bmatrix}I_{oq} & 1/L_o & 0\\ -I_{od} & 0 & 1/L_o\end{bmatrix}, B_{Z2} = \begin{bmatrix}-1/L_o & 0\\ 0 & -1/L_o\end{bmatrix}$$

where R_o and L_o is the output impedance resistance and inductance respectively.

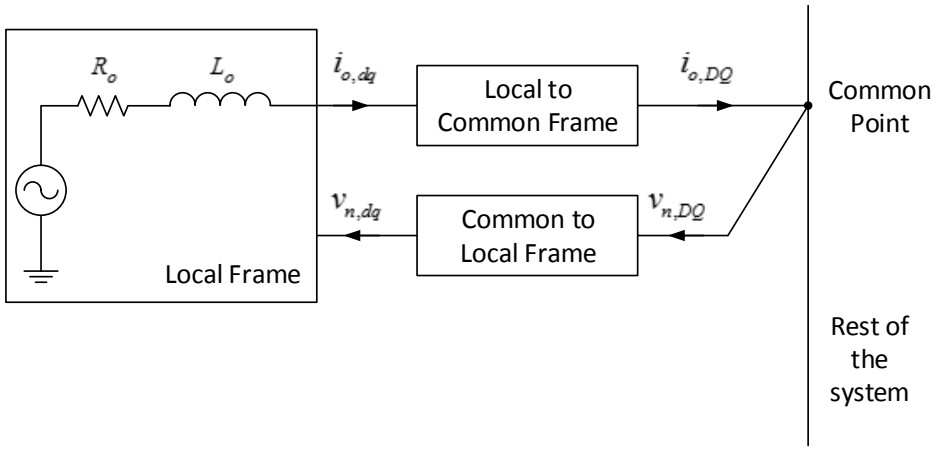

Figure 4.18. Frame transformation

C. Mapping model

The output of each inverter to the network will be the states of Δi_{odq} in the local dq-frame of each inverter as shown in Figure 4.18. However, the distribution lines and loads models will be in a common DQ-frame which is selected as the local frame of the first inverter. Therefore, each inverter output state has to be converted to the common DQ-frame. The node voltages v_{nDQ} are converted from the common frame to the local one because they will be used as inputs to each inverter model in its local frame. The conversion between the frames could be calculated using (68) as,

$$x_{DQ} = T_m . x_{dq}$$

$$where \qquad (68)$$

$$T_m = \begin{bmatrix} \cos(\delta) & -\sin(\delta) \\ \sin(\delta) & \cos(\delta) \end{bmatrix}$$

and for the sake of the model building, small deviations of (68) produce the sub-state space of the conversion process. The state equations of the output current from the local to the common frame are,

$$\begin{bmatrix} \Delta i_{oD} \\ \Delta i_{oQ} \end{bmatrix} = C_{Ti} \begin{bmatrix} \Delta\delta \\ \Delta P \\ \Delta Q \end{bmatrix} + D_{Ti} \begin{bmatrix} \Delta i_{od} \\ \Delta i_{oq} \end{bmatrix} \tag{69}$$

where

$$C_{Ti} = \begin{bmatrix} -I_{od}.\sin(\delta_o) - I_{oq}.\cos(\delta_o) & 0 & 0 \\ I_{od}.\cos(\delta_o) - I_{oq}.\sin(\delta_o) & 0 & 0 \end{bmatrix}, D_{Ti} = \begin{bmatrix} \cos(\delta_o) & -\sin(\delta_o) \\ \sin(\delta_o) & \cos(\delta_o) \end{bmatrix}$$

and the state equations of the node voltage from the common to the local frame are,

$$\begin{bmatrix} \Delta v_{nd} \\ \Delta v_{nq} \end{bmatrix} = C_{Tv} \begin{bmatrix} \Delta\delta \\ \Delta P \\ \Delta Q \end{bmatrix} + D_{Tv} \begin{bmatrix} \Delta i_{od} \\ \Delta i_{oq} \end{bmatrix} \tag{70}$$

where

$$C_{Tv} = \begin{bmatrix} -V_{nD}.\sin(\delta_o) + V_{nQ}.\cos(\delta_o) & 0 & 0 \\ -V_{nD}.\cos(\delta_o) - V_{nQ}.\sin(\delta_o) & 0 & 0 \end{bmatrix}, D_{Tv} = \begin{bmatrix} \cos(\delta_o) & \sin(\delta_o) \\ -\sin(\delta_o) & \cos(\delta_o) \end{bmatrix}$$

where δ_o and V_{nDQ} are the equilibrium points of the phase and node voltage respectively.

D. Distribution lines model

The distribution lines in Figure 4.17 are another series of RL networks between the node voltages $v_{n,i}$ to $v_{n,h}$. Here, we called any source node for any line current as v_{source} and the sink node as v_{sink}. Using the common DQ-frame the

state equations for the line currents connected between the nodes v_{source} and v_{sink} are,

$$\begin{aligned}\frac{di_{LineD}}{dt} &= \frac{-R_{Line}}{L_{Line}} i_{LineD} + \omega_o . i_{LineQ} - \frac{1}{L_{Line}} v_{sourceD} + \frac{1}{L_{Line}} v_{sinkD} \\ \frac{di_{LineQ}}{dt} &= \frac{-R_{Line}}{L_{Line}} i_{LineQ} - \omega_o . i_{LineD} - \frac{1}{L_{Line}} v_{sourceQ} + \frac{1}{L_{Line}} v_{sinkQ}\end{aligned} \tag{71}$$

By perturbing the states we obtain the small signal state space of each line as,

$$\begin{bmatrix} \Delta \dot{i}_{LineD} \\ \Delta \dot{i}_{LineQ} \end{bmatrix} = A_N \begin{bmatrix} \Delta i_{LineD} \\ \Delta i_{LineQ} \end{bmatrix} + B_{N\omega} \left[\Delta \omega\right] + B_{Nvsource} \begin{bmatrix} \Delta v_{sourceD} \\ \Delta v_{sourceQ} \end{bmatrix} + B_{Nvsink} \begin{bmatrix} \Delta v_{sinkD} \\ \Delta v_{sinkQ} \end{bmatrix}$$

where

$$A_N = \begin{bmatrix} -R_{Line}/L_{Line} & \omega_o \\ \omega_o & -R_{Line}/L_{Line} \end{bmatrix}, B_{N\omega} = \begin{bmatrix} I_{LineQ} \\ -I_{LineD} \end{bmatrix}, \tag{72}$$

$$B_{Nvsource} = \begin{bmatrix} 1/L_{Line} & 0 \\ 0 & 1/L_{Line} \end{bmatrix}, B_{Nvsink} = \begin{bmatrix} -1/L_{Line} & 0 \\ 0 & -1/L_{Line} \end{bmatrix}$$

E. Loads model

By the same manner, the state equations of the loads at any node v_n can be obtained as,

$$\begin{aligned}\frac{di_{LoadD}}{dt} &= \frac{-R_{Load}}{L_{Load}} i_{LoadD} + \omega_o . i_{LoadQ} + \frac{1}{L_{Load}} v_{nD} \\ \frac{di_{LoadQ}}{dt} &= \frac{-R_{Load}}{L_{Load}} i_{LoadQ} - \omega_o . i_{LoadD} + \frac{1}{L_{Load}} v_{nQ}\end{aligned} \tag{73}$$

and the small signal model is,

$$\begin{bmatrix} \Delta \dot{i}_{LoadD} \\ \Delta \dot{i}_{LoadQ} \end{bmatrix} = A_L \begin{bmatrix} \Delta i_{LoadD} \\ \Delta i_{LoadQ} \end{bmatrix} + B_{L\omega} \left[\Delta \omega \right] + B_{Lv} \begin{bmatrix} \Delta v_{nD,i} \\ \Delta v_{nQ,i} \end{bmatrix}$$

where

$$A_L = \begin{bmatrix} -R_{Load} / L_{Load} & \omega_o \\ \omega_o & -R_{Load} / L_{Load} \end{bmatrix}, B_{L\omega} = \begin{bmatrix} I_{LoadQ} \\ -I_{LoadD} \end{bmatrix}, \quad (74)$$

$$B_{Lv} = \begin{bmatrix} 1/L_{Load} & 0 \\ 0 & 1/L_{Load} \end{bmatrix}$$

F. Single inverter model

A complete state space model of an inverter can be obtained by combining the state space models of the power sharing controller, (66), and the output impedance, (67). The model contains the states of $\Delta\delta, \Delta P, \Delta Q, \Delta i_{odq}$ and the inputs are the node voltages, Δv_{nDQ}, in common DQ-frame to be internally converted. The output state is essentially the inverter's output current Δi_{oDQ} in the common DQ-frame. The first inverter should give an extra output that is a frequency of the common DQ-frame, $\Delta\omega_{com}$.

Now a state space model of one single inverter, i, can be built as follows,

$$\dot{\left[\Delta x_{inv,i}\right]} = A_{inv,i}\left[\Delta x_{inv,i}\right] + B_{inv,i}\left[\Delta v_{nDQ,i}\right] + B_{inv\omega com,i}\left[\Delta\omega_{com,i}\right]$$

$$\begin{bmatrix}\Delta\omega_i \\ \Delta i_{oD,i} \\ \Delta i_{oQ,i}\end{bmatrix} = \begin{bmatrix}C_{inv\omega,i} \\ C_{invc,i}\end{bmatrix}\left[\Delta x_{inv,i}\right]$$

where

$$\left[\Delta x_{inv,i}\right] = \begin{bmatrix}\Delta\delta_i & \Delta P_i & \Delta Q_i & \Delta i_{od,i} & \Delta i_{oq,i}\end{bmatrix}^T \quad (75)$$

$$A_{inv,i} = \begin{bmatrix} A_P + B_{Pv}.C_{Pv} & B_{Pi} \\ B_{Z1}.C_P + B_{Z2}.C_{Tv} & A_Z \end{bmatrix}, B_{inv,i} = \begin{bmatrix} 0 \\ B_{Z2}.D_{Tv} \end{bmatrix}, B_{inv\omega com,i} = \begin{bmatrix} B_{P\omega com} \\ 0 \\ 0 \end{bmatrix}$$

$$C_{inv\omega,i} = \begin{cases} \begin{bmatrix} C_{P\omega} & 0 & 0 \end{bmatrix}, i = 1 \\ [0]_{1\times 5}, i \neq 1 \end{cases}$$

$$C_{invc,i} = \begin{bmatrix} C_{Ti} & D_{Ti} \end{bmatrix}$$

G. Combined inverters model

As the output of each individual inverter model is in a common DQ-frame that corresponds to the first inverter frame for example, a lumped model of all inverters can be built to be later integrated with other model subsystems in DQ-frame. Therefore, for a microgrid having g inverters, the state space model of combined parallel inverters is given in (76).

$$\dot{[\Delta x_{INV}]} = A_{INV}[\Delta x_{INV}] + B_{INV}[\Delta v_{nDQ}]$$
$$[\Delta i_{oDQ}] = C_{INVc}[\Delta x_{INV}]$$

where

$$[\Delta x_{INV}] = [\Delta x_{inv,1} \quad \Delta x_{inv,2} \quad \dots \quad \Delta x_{inv,g}]^T$$
$$[\Delta v_{nDQ}] = [\Delta v_{nDQ,1} \quad \Delta v_{nDQ,2} \quad \dots \quad \Delta v_{nDQ,n}]^T$$
$$[\Delta i_{oDQ}] = [\Delta i_{oDQ,1} \quad \Delta i_{oDQ,2} \quad \dots \quad \Delta i_{oDQ,g}]^T$$

$$A_{INV} = \begin{bmatrix} A_{inv,1} + B_{inv,1}.C_{inv\omega com,1} & 0 & . & 0 \\ B_{inv,2}.C_{inv\omega com,2} & A_{inv,2} & . & 0 \\ . & . & . & 0 \\ B_{inv,g}.C_{inv\omega com,g} & 0 & 0 & A_{inv,g} \end{bmatrix}_{5g\times 5g}, \tag{76}$$

$$B_{INV} = \begin{bmatrix} B_{inv,1} & 0 & . & 0 \\ 0 & B_{inv,1} & . & 0 \\ . & . & . & 0 \\ 0 & 0 & 0 & B_{inv,g} \end{bmatrix}_{5g\times 2n},$$

$$C_{INVc} = \begin{bmatrix} C_{invc,1} & 0 & . & 0 \\ 0 & C_{invc,2} & . & 0 \\ . & . & . & 0 \\ 0 & 0 & 0 & C_{invc,g} \end{bmatrix}_{2g\times 5g},$$

$$C_{INV\omega com} = [C_{inv\omega,1} \quad C_{inv\omega,2} \quad . \quad C_{inv\omega,g}]$$

H. Completed microgrid model

The adopted strategy of modelling enables us to divide the whole system to subsystems. Each has its inputs, outputs and states. Therefore, the model is simplified as a source subsystem that is represented by the combined inverters model, the combined distribution lines and the combined loads models to be defined later. Therefore, in the same way, the distribution lines model could be

combined in one subsystem and the loads models in another subsystem. Finally, we obtain three subsystems that together give the full representation of the microgrid. Now for m lines, the combined distribution lines model will be,

$$A_{NET} = \begin{bmatrix} A_{N,1} & 0 & . & 0 \\ 0 & A_{N,2} & . & 0 \\ . & . & . & 0 \\ 0 & 0 & 0 & A_{N,m} \end{bmatrix}_{2m\times 2m},$$
$$B_{NET\omega} = \begin{bmatrix} B_{N\omega,1} \\ B_{N\omega,2} \\ . \\ B_{N\omega,m} \end{bmatrix}_{2m\times 1}, B_{NETv} = \begin{bmatrix} B_{Nvsource,1} + B_{Nvsink,1} \\ B_{Nvsource,2} + B_{Nvsink,2} \\ . \\ B_{Nvsource,m} + B_{Nvsink,m} \end{bmatrix}_{2m\times 2n} \quad (77)$$

The same for l loads, the combined model will be,

$$A_{Load} = \begin{bmatrix} A_{L,1} & 0 & . & 0 \\ 0 & A_{L,2} & . & 0 \\ . & . & . & 0 \\ 0 & 0 & 0 & A_{L,l} \end{bmatrix}_{2l\times 2l},$$
$$B_{Load\omega} = \begin{bmatrix} B_{L\omega,1} \\ B_{L\omega,2} \\ . \\ B_{L\omega,l} \end{bmatrix}_{2l\times 1}, B_{Loadv} = \begin{bmatrix} B_{Lv,1} \\ B_{Lv,2} \\ . \\ B_{Lv,l} \end{bmatrix}_{2m\times 2l} \quad (78)$$

Before getting the entire microgrid system, it is noted that the node voltages are treated as inputs to the subsystems. To close the loop, these voltages have to be defined in terms of the states to ease the model construction. To achieve that, a virtual high resistor r_N can be assumed to be connected to each node voltage. This resistor has negligible impact on the system dynamics [79]. Consequently, the node voltage states can be calculated as,

$$\left[\Delta v_{nDQ,i}\right] = \left[R_N\right]_{2n\times 2n}\left(\left[C_{io}\right]_{2n\times 2g}.\begin{bmatrix}\Delta i_{oDQ,i}\\ .\\ .\\ \Delta i_{oDQ,g}\end{bmatrix}_{2g\times 1} + \left[C_{iLine}\right]_{2n\times 2m}.\begin{bmatrix}\Delta i_{LineDQ,i}\\ .\\ .\\ \Delta i_{LineDQ,m}\end{bmatrix}_{2m\times 1} - \left[C_{iLoad}\right]_{2n\times 2l}.\begin{bmatrix}\Delta i_{LoadDQ,i}\\ .\\ .\\ \Delta i_{LoadDQ,l}\end{bmatrix}_{2l\times 1}\right) \quad (79)$$

In (79), R_N is a diagonal matrix whose element is r_N. The matrix C_{io} maps each inverter connection points to the network nodes. For example, if the inverter i is connected to node j then the element (i,j) is 1 and others row elements are zeros. Likewise, the C_{iLoad} matrix maps the load, i, connection points to the network nodes. The matrix C_{iLine} maps the distribution line connections to the network nodes. Note that if the node is a source, the element corresponding to it will be +1 and if it is a sink node then the element will be -1.

Eventually, the subsystems can be gathered together and a full microgrid model is then obtained as (80) where the states are $[\Delta\delta_i, \Delta P_i, \Delta Q_i, \Delta i_{odq,i}, \Delta i_{LineDQ,i}, \Delta i_{LoadDQ,i}, \Delta v_{nDQ,i}]$.

$$A_{mg} = \begin{bmatrix} A_{INV} + B_{INV}.R_N.C_{io}.C_{INVc} & B_{INV}.R_N.C_{iLine} & B_{INV}.R_N.C_{iLoad} \\ B_{NET\omega}.C_{INV\omega com} + B_{NETv}.R_N.C_{io}.C_{INVc} & A_{NET} + B_{NETv}.R_N.C_{iLine} & B_{NETv}.R_N.C_{iLoad} \\ B_{Load\omega}.C_{INV\omega com} + B_{Loadv}.R_N.C_{io}.C_{INVc} & B_{Loadv}.R_N.C_{iLine} & A_{Load} + B_{Loadv}.R_N.C_{iLoad} \end{bmatrix} \quad (80)$$

4.6.2. DC link voltage model

The small signal model of the microgrid is extended to include the voltage across the DC link capacitor. The relationship between the imported power (during transient, inverter can absorb power) and the capacitor energy E, Figure 4.7, is derived and linearized as seen in Section 4.4. In the same way, the energy equation in (81) is linearized and the state of the DC link voltage, ΔV_{DClink}, for any inverter is obtained as in (82). In (83), the states are manipulated to correspond to the same previous state vector Δx_{inv}.

$$E = \frac{1}{2} C_{DClink} V_{DClink}^2 = \int p_{ins} dt$$
$$\Delta V_{DClink,i} = \frac{2m}{C_{DClink,i}.s} \Delta p_{ins} \quad (81)$$

where, p_{ins} is the instantaneous active power

$$\begin{bmatrix} \Delta \dot{V}_{DClink} \end{bmatrix} = \begin{bmatrix} B_{DCv} \end{bmatrix} \begin{bmatrix} \Delta v_{od} \\ \Delta v_{oq} \end{bmatrix} + \begin{bmatrix} B_{DCi} \end{bmatrix} \begin{bmatrix} \Delta i_{od} \\ \Delta i_{oq} \end{bmatrix}$$

where (82)

$$B_{DCv} = \frac{3m}{C_{DClink}} \begin{bmatrix} I_{od} & I_{oq} \end{bmatrix}, B_{DCi} = \frac{3m}{C_{DClink}} \begin{bmatrix} V_{od} & V_{oq} \end{bmatrix}$$

where, m is the square root linearization factor

$$\begin{bmatrix} \Delta \dot{V}_{DClink,i} \end{bmatrix} = \begin{bmatrix} B_{DC,i} \end{bmatrix} . \begin{bmatrix} x_{inv,i} \end{bmatrix}$$
$$B_{DC,i} = \begin{bmatrix} \begin{bmatrix} 0 & B_{DCv,i} \end{bmatrix} . C_{P,i} & B_{DCi,i} \end{bmatrix} \quad (83)$$

Before finalising the entire model, the combined DC voltage state equations are obtained as,

$$\begin{bmatrix} \cdot \\ \Delta V_{DClink,1} \\ \Delta V_{DClink,2} \\ \cdot \\ \Delta V_{DClink,g} \end{bmatrix} = [B_{DC}].[x_{INV}] \tag{84}$$

$$B_{DC} = \begin{bmatrix} B_{DC,1} & 0 & . & 0 \\ 0 & B_{DC,2} & . & 0 \\ . & . & . & 0 \\ 0 & 0 & 0 & B_{DC,g} \end{bmatrix}_{g\times 5g}$$

By recalling the matrix A_{mg} and incorporating the states of DC link voltages, the completed model will be redefined as,

$$A'_{mg} = \begin{bmatrix} A_{mg} & & [0]_{(5g+2m+2l)\times g} \\ B_{DC} \quad [0]_{g\times 2m} & [0]_{g\times 2l} & [0]_{g\times g} \end{bmatrix} \tag{85}$$

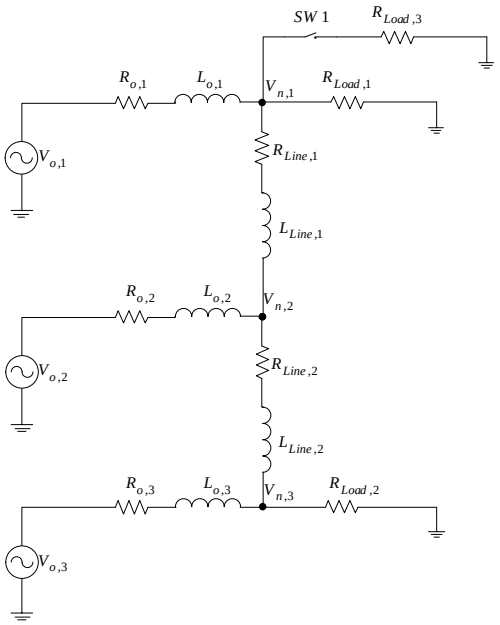

Figure 4.19. The microgrid simulation model of three parallel inverters with two distribution lines and three loads

4.6.3. Model evaluation

The small signal model in (85) has been linearized around stable operating points. These points can be calculated by two methods. One method is to set the nonlinear state equations to zero. Another approach is to simulate the model in Matlab to determine the numerical solutions. Here, the second approach is adopted. Thereafter, the linearized model has been compared with a three phase detailed model built in Matlab/Simulink using SimPowerSystem library with the same parameters in Table 4.4. The model, in Figure 4.19, is a single phase diagram of the three phase system that includes three inverters with the same droop control gains and output impedances. The first part of testing is to disturb the system by exciting it with a 3.8kW step change. This is realized by closing the switch SW1 and engaging Load 3. Figure 4.20 shows the average active power output responses of the three inverters. The responses of both models are in good agreement, which reveals quite accurate transient expectations from the small signal model.

Figure 4.21 shows the active power responses of the three inverters if the set-points are ($P_1^* = 20kW, P_2^* = 10kW \; and \; P_3^* = 0kW$) and the load is 13.1 kW (without Load 3). The small signal model is again in a very good agreement with the detailed model. The third inverter is importing power which increases the voltage across the DC link capacitor. Figure 4.22 shows how the DC link voltage of the third inverter is rising which will cause the inverter to trip unless a controller is used [80].

Symbol	Description	Value
P_1^*	Active Power set-point for inverter 1	20 kW
P_2^*	Active Power set-point for inverter 2	10 kW
P_3^*	Active Power set-point for inverter 3	0 kW
Q_1^*	Reactive Power set-point for inverter 1	0 VAR
Q_2^*	Reactive Power set-point for inverter 2	0 VAR
Q_3^*	Reactive Power set-point for inverter 3	0 VAR
R_{L1}	Load Resistance 1	25 Ω/phase
R_{L2}	Load Resistance 2	20 Ω/phase
R_{L3}	Load Resistance 3	38 Ω/phase
L_o	Inverter output inductance (small signal and detailed simulation model)	2000 µH
R_o	Inverter output resistance (small signal and detailed simulation model)	0.1 Ω
m_p	Frequency drooping gain	5×10^{-4} rad/s/W
n_q	Voltage drooping gain	5×10^{-4} V/Var
V_o	Voltage set point	220 Vrms
f_o	Frequency set point	50 Hz
ω_c	Measurement filter cutoff frequency	30 rad/s
V_{DClink}^*	Nominal DC link voltage	750 V
$V_{DClink\_max}^*$	Maximum DC link voltage	1200 V
m	Linearization factor relating V_{DClink}^2 to V_{DClink}	6.5×10^{-4}
X_{line1}	Distribution line reactance 1	0.1 Ω
R_{line1}	Distribution line resistance 1	0.23 Ω
X_{line2}	Distribution line reactance 2	0.58 Ω
R_{line2}	Distribution line resistance 2	0.35 Ω
k_p	DC link voltage controller proportional gain	30
k_d	DC link voltage controller derivative gain	1

Table 4.4 Simulation Parameters of a three phase microgrid system

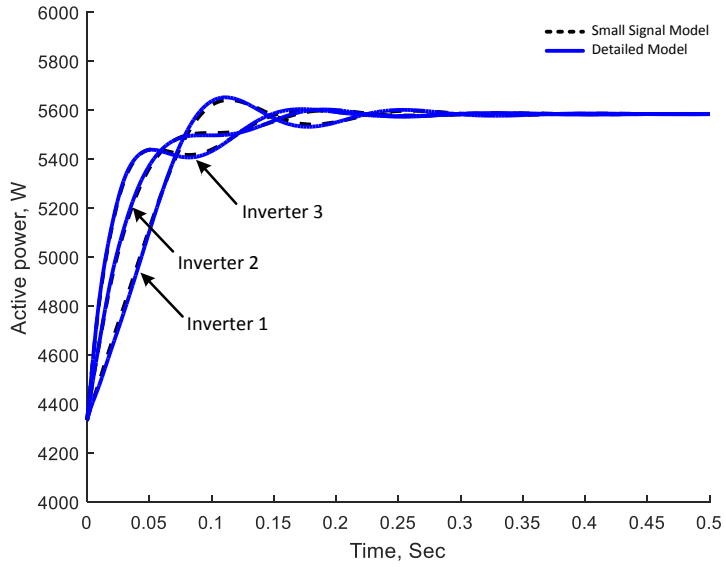

Figure 4.20. Active power output of the three inverters in island mode by the small signal and the detailed models

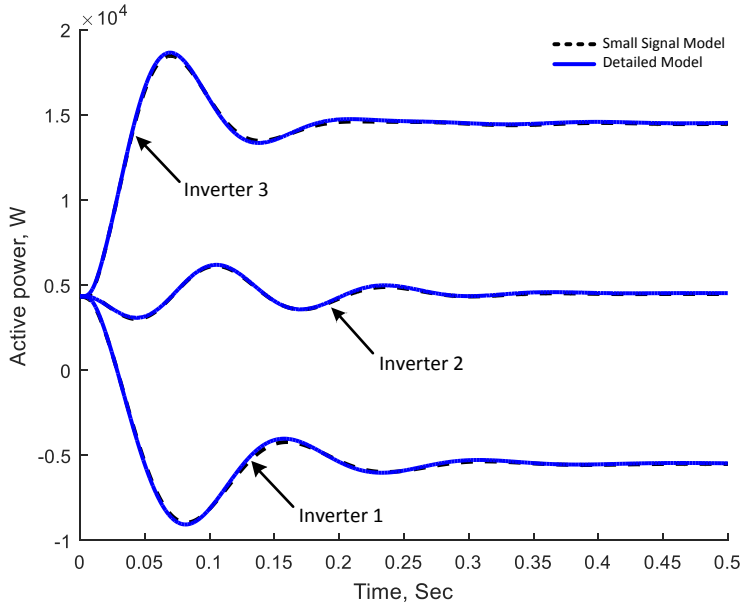

Figure 4.21. Active power output of the three inverters under different power set-points (small signal model and detailed model)

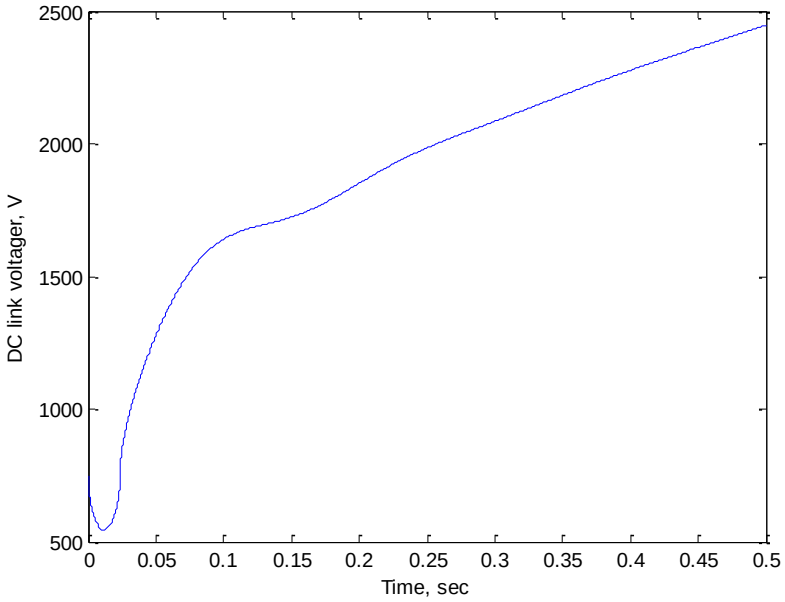

Figure 4.22. DC link voltage response of the third inverter

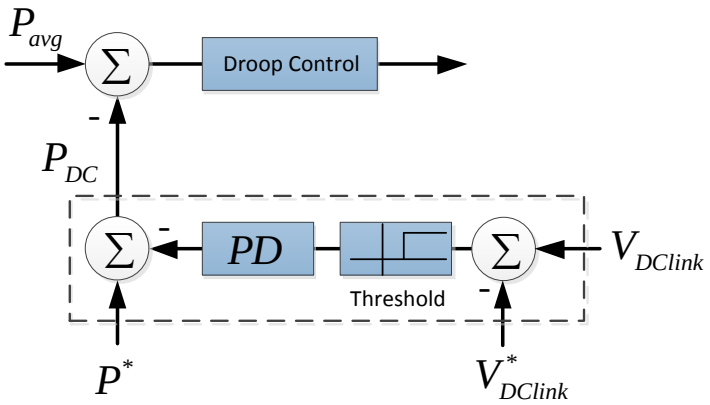

Figure 4.23. Proposed PD DC link voltage controller

4.6.4. Proposed DC link voltage controller

In this section, a PD controller will be proposed and studied for the multi-inverter model developed in previous sections. The proposed controller is shown in Figure 4.23. It employs P and D terms to emphasize the generality of the

modelling technique and to demonstrate that the derivative term also enhances the overshoot and settling time of the system response. The derivative term produces fast action corresponding to any disturbance. Thus the D term allows for fast response to compensate the output variations in the DC voltage.

A. DC link voltage controller modelling

The input signal to the droop control loop is,

$$P_{DC} = -P^{*} + (k_p + s.k_d)(V_{DClink} - V^{*}_{DClink}) \tag{86}$$

By perturbing it around the equilibrium points we obtain,

$$\Delta P_{DC} = (k_p + s.k_d).\Delta V_{DClink} \tag{87}$$

After rearranging, the controller for any inverter is calculated as,

$$\begin{aligned} &\Delta P_{DC} = C_{DC1}.\Delta V_{DClink} + C_{DC}.\Delta x_{inv} \\ &where \\ &C_{DC1} = k_p \\ &C_{DC} = [C_{DC2} \quad C_{DC3}] \\ &C_{DC2} = k_d.[0 \quad B_{DCv}].C_P \\ &C_{DC3} = k_d.[B_{DCi}] \end{aligned} \tag{88}$$

To insert this controller state equation into the model (85), the state of the phase angle has to change as,

$$s.\Delta\delta = -m_p(\Delta P + C_{DC1}.\Delta V_{DClink} + C_{DC}.\Delta x_{inv}) \tag{89}$$

Then by redefining equation (66), the $A_{inv,i}$ in (75) will be,

$$A'_{inv,i} = \begin{bmatrix} A_P + B_{Pv}.C_{Pv} - \begin{bmatrix} m_p.C_{DC2} \\ [0]_{2\times3} \end{bmatrix} & B_{Pi} - \begin{bmatrix} m_p.C_{DC3} \\ [0]_{2\times2} \end{bmatrix} \\ B_{Z1}.C_P + B_{Z2}.C_{Tv} & A_Z \end{bmatrix} \tag{90}$$

Consequently, the completed system with the DC voltage controller is derived as,

$$A'_{mg} = \begin{bmatrix} A_{mg} & & C_{DCcont} \\ B_{DC} & [0]_{g\times 2m} & [0]_{g\times 2l} & [0]_{g\times g} \end{bmatrix}$$

$$C_{DCcont} = \begin{bmatrix} \begin{bmatrix} C_{DC1,1} & . & . & 0 \end{bmatrix}_{1\times g} \\ [0]_{4\times g} \\ \begin{bmatrix} 0 & C_{DC1,2} & . & 0 \end{bmatrix}_{1\times g} \\ [0]_{4\times g} \\ . \\ . \\ \begin{bmatrix} 0 & . & . & C_{DC1,g} \end{bmatrix}_{1\times g} \\ [0]_{4\times g} \\ [0]_{(2m+2l)\times g} \end{bmatrix}_{(5g+2m+2l)\times g} \quad (91)$$

B. Analysis and simulation results

The same detailed model of three inverters in island mode, that has been utilized to validate the small signal model, is used to justify the performance of the proposed controller and the prediction of the developed small signal model. Figure 4.24 illustrates a zoomed version of the root locus of the microgrid model as the high frequency modes have less significance. The figure shows the poles trajectory as the derivative controller term has been excluded $(k_d = 0)$ and the proportional gain varies as $0 < k_p < 100$. As is seen, increasing k_p shifts the complex poles to be dominant and makes the system less damped toward instability if $k_p > 65$. The locus in Figure 4.25 is developed as the parameters of the PD controller vary. Figure 4.25a depicts the poles evaluation as $0 < k_p < 300,\ k_d = 1$ and in Figure 4.25b as $0 < k_d < 10,\ k_p = 30$. The arrows show the increasing trend. It is clear that the system is stable for the specified values range of k_p that is wider than the case in Figure 4.24. Furthermore, the

derivative gain existence introduces more damping to the system as the real poles dominate. In the other hand, by increasing k_d, the system becomes unstable. The Matlab/Simulink simulation adopted the values of $k_p = 30$, $k_d = 1$ as they give a damping ration of 0.3.

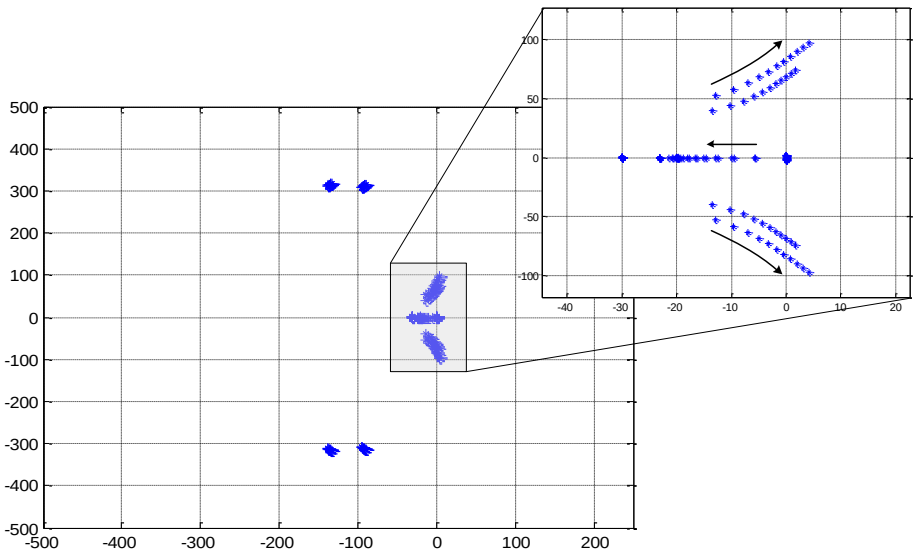

Figure 4.24. Root locus of the entire system with DC voltage controller when

$$0 < k_p < 100,\ k_d = 0$$

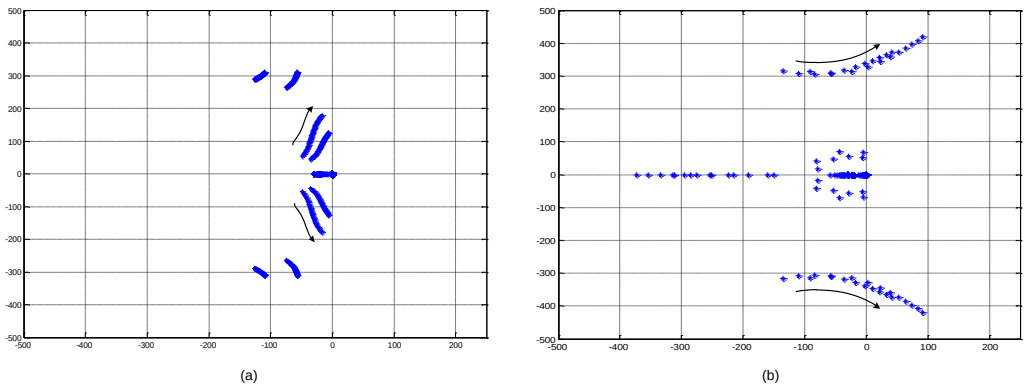

Figure 4.25. Root locus of the entire system with DC voltage controller when (a)

$0 < k_p < 300,\ k_d = 1$ (b) $0 < k_d < 10,\ k_p = 30$

Figure 4.26a shows the active power responses of the three inverters when initially run in island mode with power set-points are as $P_1^* = 20kW, P_2^* = 10kW \; and \; P_3^* = 0kW$. The derivative term is zero $(k_p = 30,\ k_d = 0)$, which makes the system more oscillatory as expected. The calculated frequency from the response is 62.2 rad/s and corresponds to the expectations from the rootlocus which is 68 rad/s. Figure 4.26b shows the response when $k_p = 30$, $k_d = 1$. In contrast with Figure 4.21, the controller succeeds in mitigating the circulating power from the other inverters and consequently prevents the rise of the DC link voltage, Figure 4.27, so decreasing the risk of tripping any inverter and presenting more damping compared with Figure 4.26a. As shown, each inverter has a different transient oscillation frequency that is predicted by the rootlocus plot as well. The locus portends two frequencies as 55.13 and 307.5 rad/s and in Figure 4.26b, the responses have two major frequencies of 54.16 and 306.5 rad/s, which reveals the validation of the developed model and the controller design criteria.

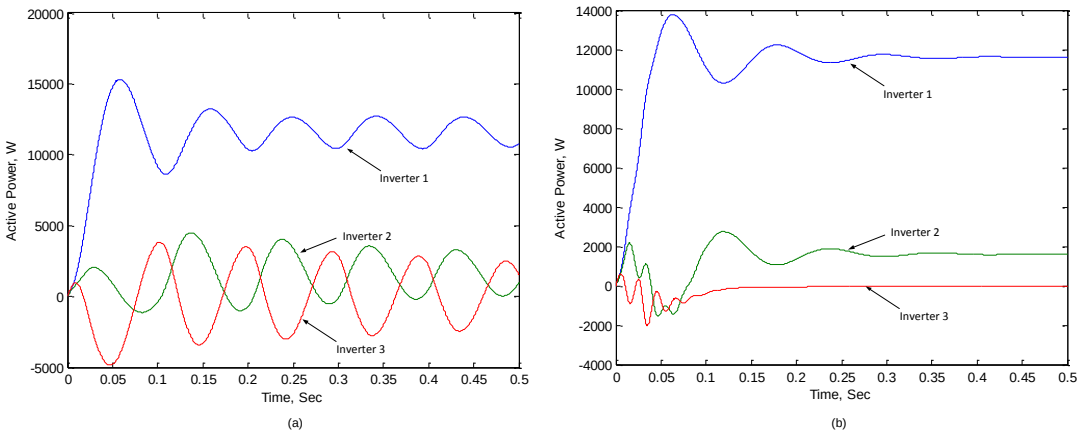

Figure 4.26. The active power responses of the three inverters when initially run in island mode and (a) $k_p = 30,\ k_d = 0$ (b) $k_p = 30,\ k_d = 1$

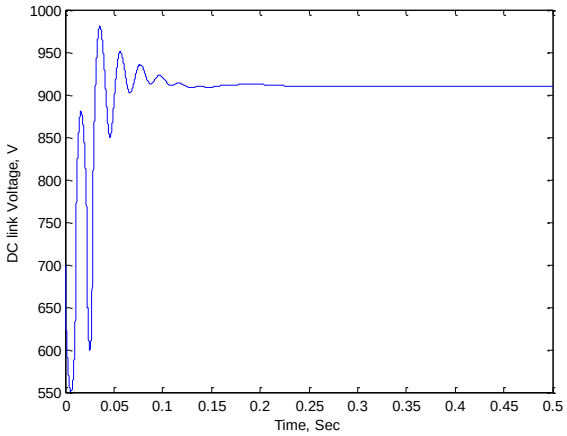

Figure 4.27. DC link voltage responses of the third inverter when the PD controller is adopted

4.7. Conclusion

This chapter has investigated the transient power between paralleled inverters during unintentional islanding and a controller to limit this circulating power has been proposed. The controller monitors the DC link voltage and in case the voltage rises above a specific limit, indicating power being imported, the controller adjusts the power set-point in proportion to the rise in the voltage. A small signal model of a microgrid consisting of two inverters in island mode has been developed and used to design the controller. Simulation and experimental results confirmed the accuracy of the developed model and the validity of the design. Finally, a completed island microgrid has been modelled based on dq-frame. The model also was used to investigate the problem when multi parallel inverters exist. A PD controller was proposed and a design by the rootlocus was presented which emphasized the predictions of the simulation results.

CHAPTER 5 IMPROVED REACTIVE POWER SHARING FOR PARALLEL-OPERATED INVERTERS IN ISLAND MODE

5.1. Introduction

Unequal impedances of interconnecting cables between paralleled inverters in island mode cause inaccurate reactive power sharing when traditional droop control is used. Many in the literature adopt low speed communications such as CAN and Ethernet, Figure 5.1, between the inverters and a central control unit to overcome this problem. However, the loss of this communication link can be very detrimental on the performance of the controller. This chapter proposes an improved reactive power-sharing control method. It uses discrete measurements of the voltage at the point of common coupling (PCC) to estimate the output impedance between the inverters and the PCC and readjust the voltage droop controller gains accordingly. The controller is then retrieved to traditional droop controller using the newly calculated gains. This increases the immunity of the controller against any loss in the communication links between the central control unit and the inverters. The capability of the proposed control method has been demonstrated in simulation and experimentally using a laboratory scale microgrid.

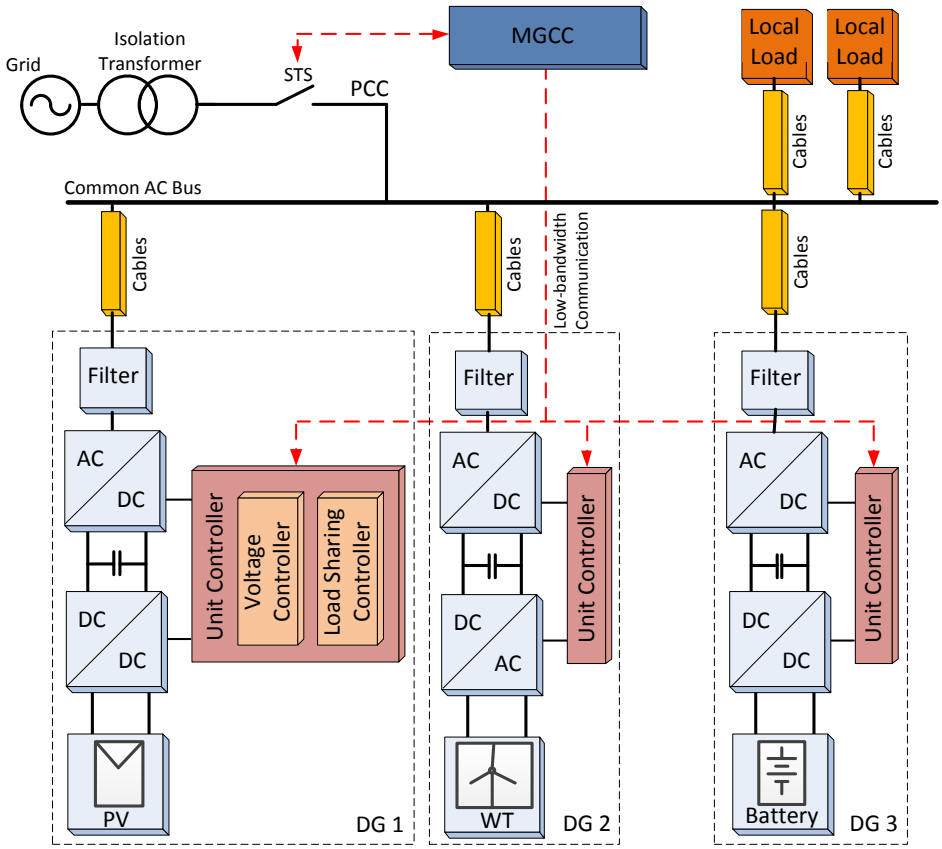

Figure 5.1. General microgrid structure including energy sources, DC/DC and DC/AC converters

5.2. Small signal analysis of reactive power sharing

Figure 5.2 shows a simple microgrid consisting of two inverters. Each inverter is modelled by its two-terminal Thevenin equivalent circuit where V and X_o represent the Thevenin voltage and impedance, respectively [8]. For a dominantly resistive output impedance, *P-V* and *Q-ω* droop control is commonly used while for an inductive output impedance, the *P-ω* and *Q-V* is used [81]. In this chapter, the output impedance is guaranteed to be inductive by using an inductive virtual impedance as described in [82] and hence the *P-ω* and *Q-V* droop control is employed. The two inverters are connected through different

feeder impedances X_{L1} and X_{L2}. The traditional droop control equations for inverter *i* are given by

$$\omega_i = \omega^* - m_i P_i \tag{92}$$

$$V_i = V^* - n_i Q_i \tag{93}$$

where ω_i and V_i are the output frequency and voltage, ω^* and V^* are the frequency and voltage set-points, m_i and n_i are the frequency and voltage droop gains and P_i and Q_i are the active and reactive power, respectively.

A small signal deviation (denoted by '~') in the output voltage $\tilde{V}_i$ in (93) is given by,

$$\tilde{V}_i = -n_i \tilde{Q}_i \tag{94}$$

This means that a small deviation in V_i with respect to a small deviation in Q_i (around the equilibrium point) is a linear line with a slope of $-n_i$ and the behaviour of V_i is determined by,

$$V_i = V_{eq} + \tilde{V}_i \tag{95}$$

By choosing the equilibrium point V_{eq} to be V^*, the small signal expression is,

$$V_i = V^* - n_i \tilde{Q}_i \tag{96}$$

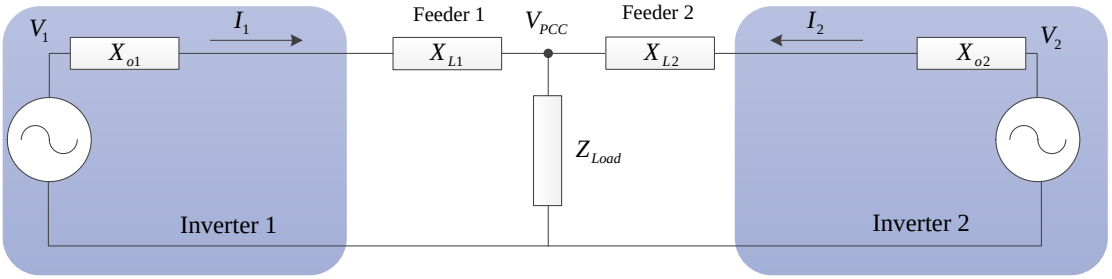

Figure 5.2. Simple islanded microgrid consists of two parallel inverters

The current flow causes a voltage drop across X_o and X_L and hence the voltage at the point of common coupling V_{PCC} will be different from V_1 and V_2.

By defining the total impedance of inverter *i* as $X_i = X_{oi} + X_{Li}$, the reactive power generated by inverter *i* can be shown to be given by

$$Q_i = \frac{V_i^2 - V_i V_{PCC} \cos\delta_i}{X_i} \tag{97}$$

where δ_i is the power angle between V_i and V_{PCC}. For a small power angle, $\cos\delta_i \approx 1$ and hence the reactive power can be approximated as

$$Q_i \approx \frac{V_i \Delta V_i}{X_i} \tag{98}$$

where

$$\Delta V_i = V_i - V_{PCC} \tag{99}$$

A small change (denoted by '~') in the reactive power $\tilde{Q}_i$ due to a change in voltage is given by

$$\tilde{Q}_i \approx \frac{1}{X_i}\left(\Delta V_{eq} \cdot \tilde{V}_i + V_{eq} \cdot \Delta\tilde{V}_i\right) \tag{100}$$

where ΔV_{eq} and V_{eq} are the equilibrium voltage difference ΔV_i and inverter output voltage V_i, respectively, around which the small signal perturbation is performed. The symbol $\Delta\tilde{V}_i$ denotes a small change in ΔV_i ; in other words $\Delta\tilde{V}_i = \tilde{V}_i - \tilde{V}_{pcc}$. Because $\Delta V_{eq} \ll V_{eq}$, and by choosing the equilibrium point $V_{eq} = V^*$, a small change in reactive power can be approximated as

$$\tilde{Q}_i \approx \frac{V^*}{X_i}\Delta\tilde{V}_i \tag{101}$$

By deviating ΔV_i in (99), substituting into (101) and rearranging, then the inverter output voltage behaviour around the equilibrium point can be expressed as

$$V_i = V_{eq} + \tilde{V}_i = V^* + \tilde{V}_{PCC} + \frac{X_i}{V^*}\tilde{Q}_i \tag{102}$$

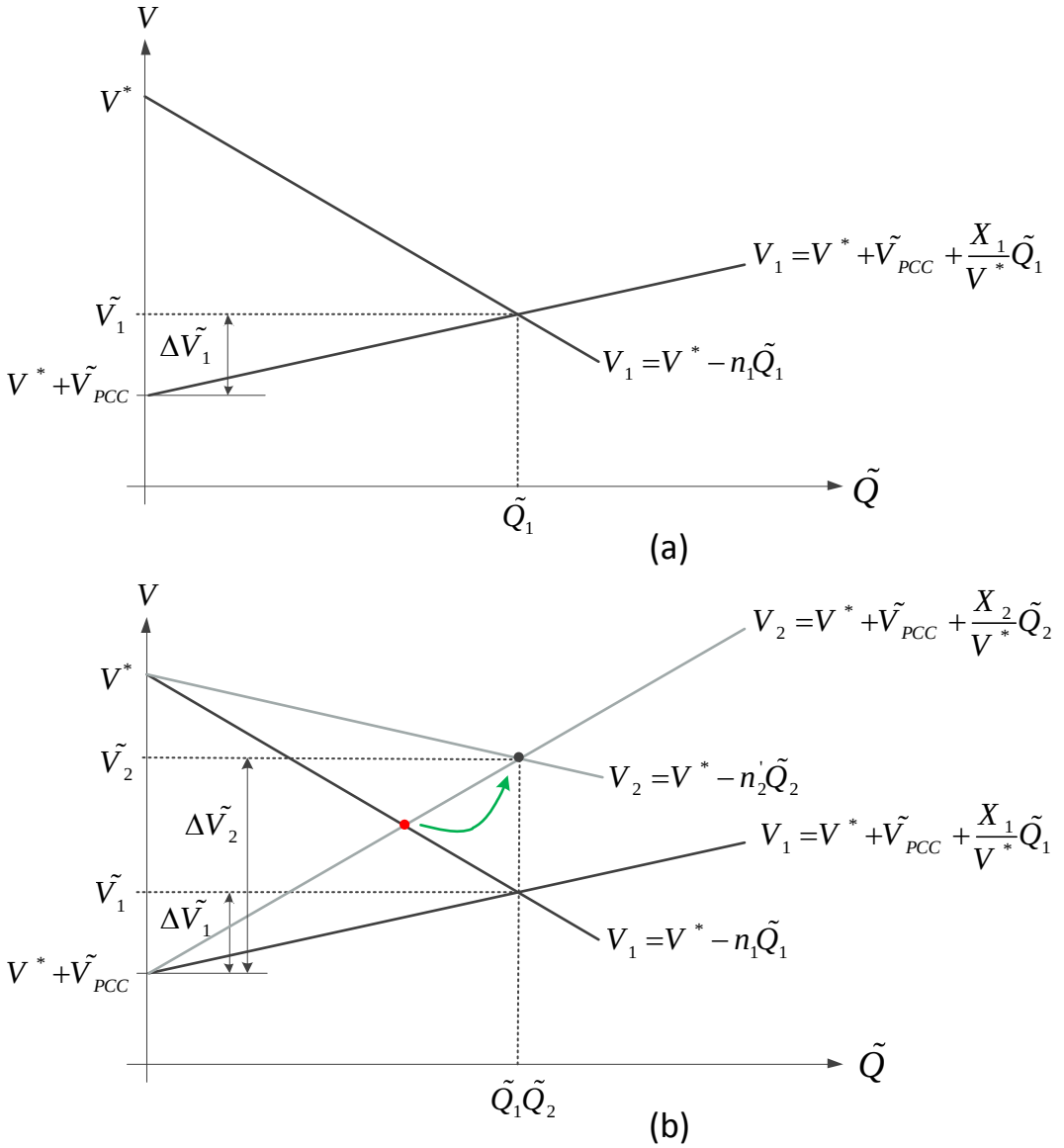

Figure 5.3. Reactive power sharing affected by the voltage drop

Both (96) and (102) define the relationship between V_i and $\tilde{Q}_i$ around the equilibrium. For inverter 1, Figure 5.3(a) represents (96) and (102) graphically as two lines. The delivered reactive power is given by where the two lines

intersect. If one inverter has higher total impedance X_i, the slope X_i/V^* in (102) will be higher and in order to deliver the same reactive power as the other inverter, the voltage droop coefficient n_i (slope in (96)) needs to be reduced. This is illustrated in Figure 5.3(b) where inverter 2 has a higher total impedance than inverter 1, $X_2 > X_1$. Therefore, for the two inverters to share reactive power equally, the voltage droop coefficient of inverter 2 needs to be reduced accordingly.

By substituting (96) into (102) we obtain

$$\tilde{Q}_i = \frac{-\tilde{V}_{PCC}}{n_i + X_i/V^*} \tag{103}$$

Hence, for the two inverters to share reactive power equally the following condition needs to be satisfied,

$$n_1 + X_1/V^* = n_2 + X_2/V^* \tag{104}$$

In order to have equal sharing of reactive power, the droop gain n_i needs to be adjusted in proportion to $1/X_i$. Thus inverters with higher output impedance will have voltage droop gains reduced. The new voltage droop gain n_i' is proposed to be calculated as

$$n'_i = n_i \frac{X_{oi}}{X_i} \tag{105}$$

where X_{oi} is the nominal output impedance of the inverter. The output impedance X_i includes the inverter output impedance X_{oi} and the interconnecting cable impedances such that $X_i = X_{oi} + X_{Li}$ (see Figure 5.2). The impedance X_{oi} should be known for each inverter while the impedance X_i can be estimated such as

$$X_i = \frac{V^* . \Delta V_i}{Q_i} \tag{106}$$

The value of X_i is needed to scale the droop gain to finally improve the reactive power sharing. This value X_i has to be calculated when all inverters share the reactive power adequately. Consequently, once an accurate reactive power sharing is obtained by using V_{PCC} [61], the output reactive power is measured then the output impedance is estimated. Therefore, after the estimation process and retrieving the traditional droop controller with the new gain, it will give the same power sharing again without V_{PCC}.

By readjusting the voltage droop gain according to (105), it can be guaranteed that the new droop gain is smaller or equal to the original droop gain. This is quite important because if the droop gain is increased beyond the designed value, instability can occur [16].

5.3. Proposed reactive power sharing controller

The proposed controller scheme is shown in Figure 5.4. It consists of two stages; in the first stage, the controller uses the PCC voltage to obtain accurate sharing between inverters, estimate X_i and calculate the new droop gain n_i'. In the second stage, reactive power control uses traditional voltage droop incorporating the new calculated droop gain n_i'. The two stages are explained below.

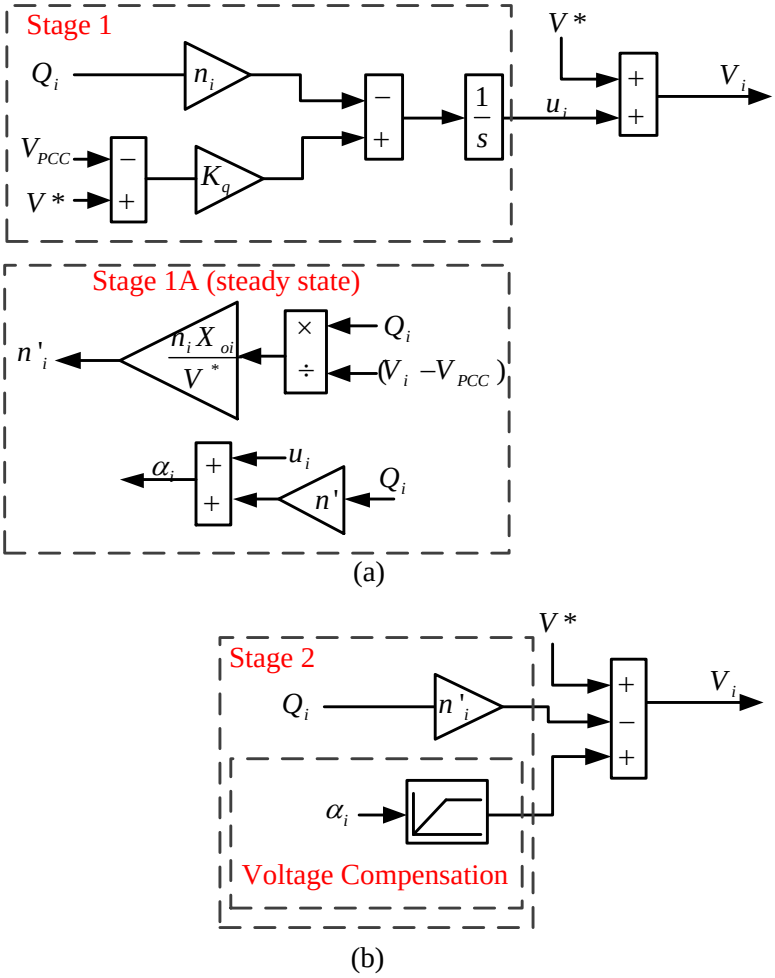

Figure 5.4. Proposed controller scheme (a) Stage 1: Accurate power sharing (b) Stage 2: Voltage compensation

A. **Stage 1**

In this stage, the voltage drop $V^* - V_{PCC}$ is calculated and compared to $n_i\, Q_i$ and the error signal is fed back to the controller through an integrator as proposed in [61] and shown in Figure 5.4a. The gain K_q is used to accelerate the transient response as required. In steady state condition, the input to the integrator is zero which means that the reactive power is given by,

$$Q_i = \frac{K_q(V^* - V_{PCC})}{n_i} \tag{107}$$

If all inverters have the same n, the right hand side of (107) is the same in all inverters. Thus, equal sharing is achieved even if the output impedances are different. When the steady state condition is reached (determined by zero input to the integrator), the output impedance X_i is estimated using (106) and the new droop gain is calculated using (105). All new droop gains are set in proportional to $1/X_i$ and thus traditional droop control can be used without using the PCC voltage.

B. **Stage 2**

In this stage, a smooth transition from a closed loop control that involves the measurement of the PCC voltage to a traditional droop control using the newly calculated droop gains is performed. At the end of stage 1 (once steady state condition is reached), the inverter output voltage is given by

$$V_{i(Stage1)} = V^* + u_i \tag{108}$$

In stage 2, after adopting the new droop gain n' with the traditional droop loop, the inverter output voltage is given by

$$V_{i(Stage2)} = V^* - n'_i Q_i + \alpha_i \tag{109}$$

where the offset α is added to make sure that the inverter voltage at the beginning of stage 2 is the same as that at the end of stage 1. Therefore, (108) and (109) should be equal and hence α is given as in (110) and it is calculated at the end of stage 1 as shown in Figure 5.4a.

$$\alpha_i = u_i + n'_i Q_i \tag{110}$$

In stage 2 the offset α is added via a ramp function as shown in Figure 5.4b.

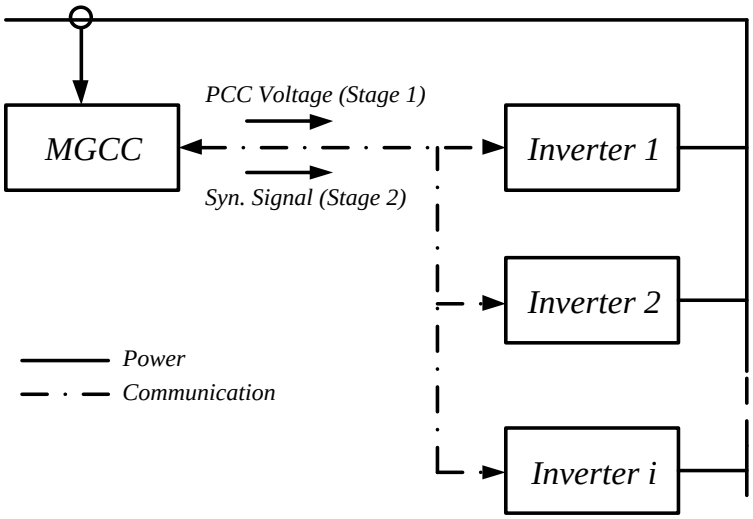

Figure 5.5. Communication scheme for the proposed controller

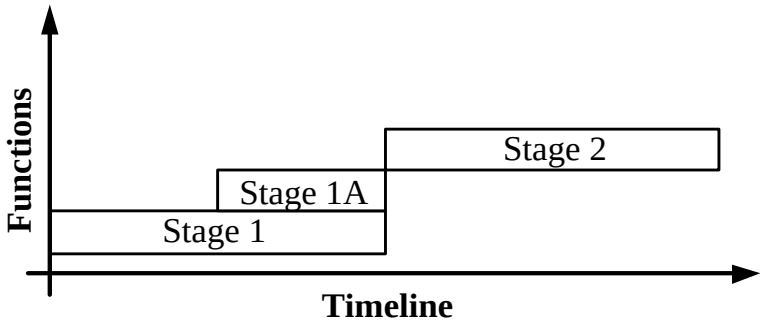

Figure 5.6. Proposed algorithm stages timeline

The proposed controller can be realized using a low-bandwidth communication link to connect each inverter with the MGCC as shown in Figure 5.5. This link sends the PCC voltage to all units simultaneously for stage 1 to get accurate *Q*

sharing. Once the steady state condition is reached (Stage 1A), flagged by zero input to the integrator, the new droop gain n' and the offset α are calculated as shown in the process timeline in Figure 5.6. At the end of stage 1, a synchronized flag is sent so that all inverters activate stage 2 at the same time. In this stage, the new calculated value of n'will be used instead of the old value n as the droop gain.

Symbol	Description	Value
m	Frequency droop gain	0.001
n	Voltage droop gain	0.001
V_o	Voltage set point	230 Vrms
f_o	Frequency set point	50 Hz
τ	Measurement filter time constant	0.5 sec
X_{o1}	Output impedance for inverter 1 (Simulation only)	2500μH
X_{o2}	Output impedance for inverter 2 (Simulation only)	2500μH
X_{L1}	Feeder line impedance for inverter 1	0 μH
X_{L2}	Feeder line impedance for inverter 2	500μH
K_q	V_{PCC} loop gain	10
P_{max}	Inverter's maximum active power	15kW
Q_{max}	Inverter's maximum reactive power	10kVar

Table 5.1 Simulation Parameter Values

5.4. Simulation Results

A model of microgrid with two inverters was built using Matlab/Simulink. Each inverter is modelled as an ideal voltage source with a series inductive output impedance as shown in Figure 5.2. The system parameters are shown in Table 5.1. The two inverters have identical parameters. However, extra impedance is inserted between inverter 2 and the PCC to model the impedance

of a long feeder, transformer of grid-side inductor. This part of the simulation is carried out to verify the proposed controller under different load conditions and comparing its performance with that of the traditional droop controller.

Figure 5.7 shows the reactive power of the two inverters with traditional droop control under different load conditions; low, medium and high corresponding to 10%, 50%, and 100% of the maximum reactive power rating of the microgrid (20kVar), respectively. It can be noticed that the two inverters do not share reactive power equally. Table 5.2 summarizes the steady state values of the simulation results.

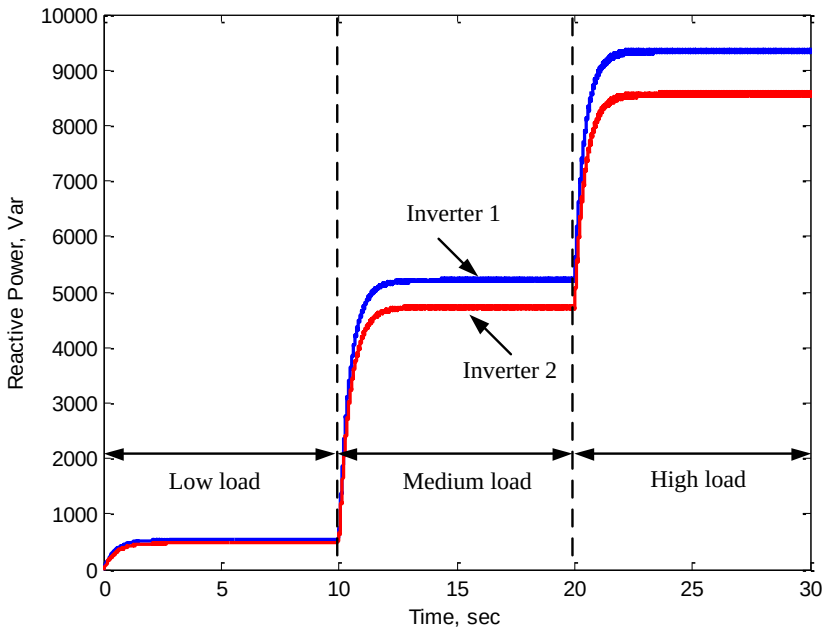

Figure 5.7. Inverter's output power when low, medium and high loads are supplied using traditional droop control

Figure 5.8 shows the reactive power with the proposed controller under different load conditions. The traditional droop controller is used until simulation time t = 5.5 sec when stage 1 is activated and the new droop gain n' and the offset α are being calculated. At simulation time t = 21 sec, stage 2 is activated and the controller reverts to traditional droop control but with the new calculated droop gain n'. At t = 21 sec, there is a dip in the reactive power and this is due to the difference between the inverter voltage at the end of stage 1 and at the beginning of stage 2. This is fixed by adding the offset α which is done gradually via a ramp function. After the controller is settled and at simulation time t = 32 sec, a sudden change in reactive load is applied to test the ability of the proposed controller to maintain good reactive power sharing. In Figure 5.8a, the activation of the proposed controller happens when the reactive load is *low* (500 Var) followed by a sudden change in reactive load from *low* to *high* (9500 Var). In Figure 5.8b, the activation of the proposed controller happens when the reactive load is *medium* (6200 Var) followed by a sudden change in reactive load from *medium* to *high* (12000 Var). In Figure 5.8c, the activation of the proposed controller happens when the reactive load is *high* (15000 Var) followed by a sudden change in reactive load from *high* to *low* (800 Var). Finally, in Figure 5.8d, the activation of the proposed controller happens when the reactive load is *high* (15000 Var) followed by a sudden change in reactive load from *high* to *medium* (8500 Var). The simulation results for these simulation conditions are all summarized in Table 5.2 which reveals the improvement of the reactive power sharing due to the proposed controller compared with the performance of the traditional control under different load conditions. It is noted that the total reactive power is different before and after

activating the proposed controller. This is due to the change of V_{PCC} as it increases by the action of the voltage drop compensation in stage 1 as seen in Figure 5.9.

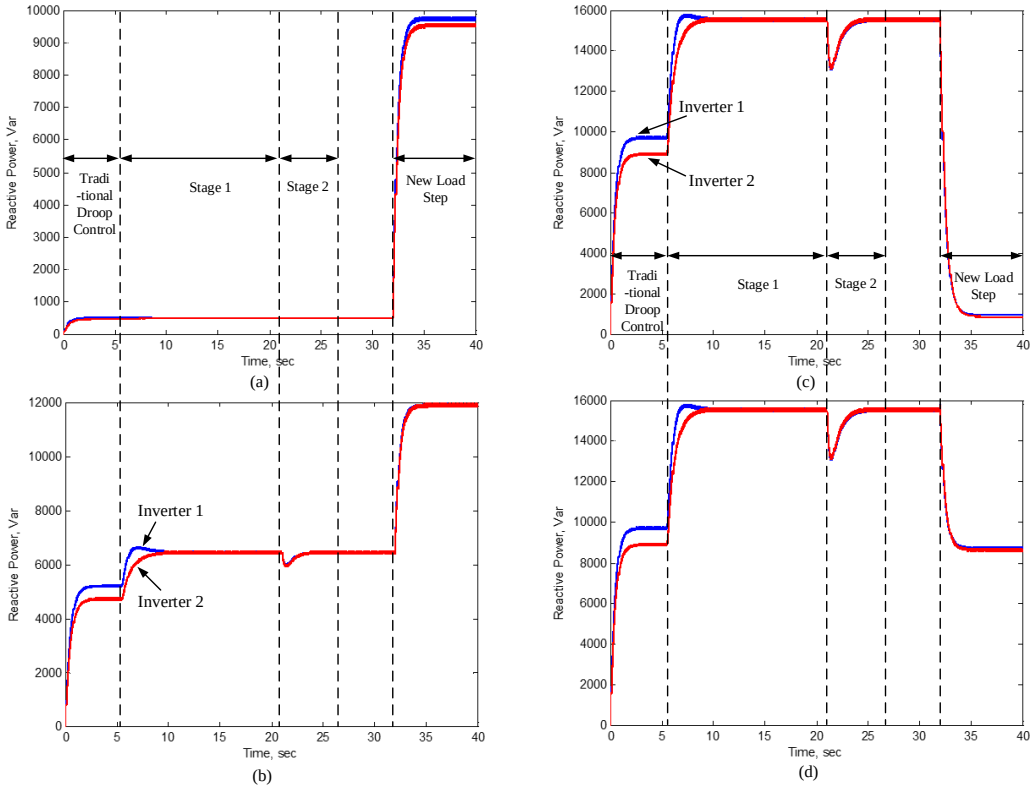

Figure 5.8. Simulation results of the proposed controller after a new load step at 32sec from (a) low to high (b) medium to high (c) high to low (d) high to medium

Figure 5.10 depicts the risk of a potential communication loss for controllers that rely on continuous measurements of the PCC voltage such as the one reported in [61] if a wireless link is used between the PCC and the inverters. Initially, the two inverters are supplying load 1 and adopting the traditional droop control until the instant t=5.5 sec when the algorithm reported in [61] is activated and accurate reactive power sharing is achieved. One of the two inverters loses the

PCC voltage measurements at t=20sec for 100ms. As can be seen, the output voltages of both inverters exceeded the limit which will cause the inverter to trip.

Traditional Droop control			
Load Case	Inverter 1 output (VAR)	Inverter 2 output (VAR)	Error %
Low	532	473	5.9%
Medium	5210	4725	4.9%
High	9350	8550	4.5%

Proposed Controller				
Load Case		Inverter 1 output (VAR)	Inverter 2 output (VAR)	Error %
During algorithm execution (Current load)	After algorithm execution (New load)			
Low	High	9770	9540	1.2%
Medium	High	11880	11880	0.0%
High	Low	952	878	4.0%
High	Medium	8725	8628	0.56%

Table 5.2 Traditional and proposed controller reactive output power

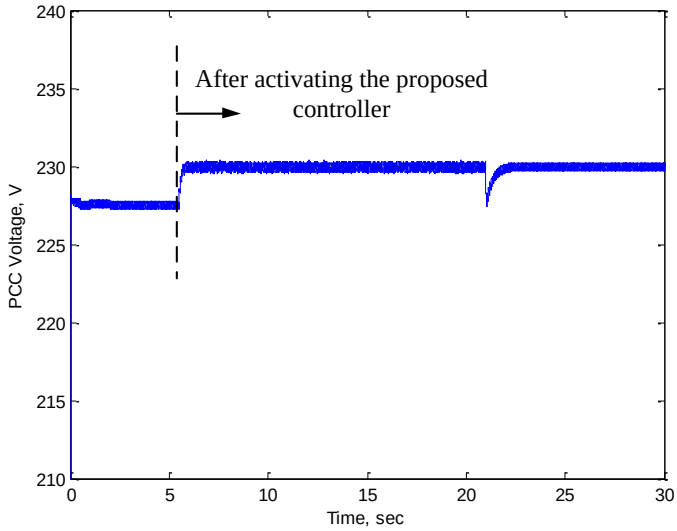

Figure 5.9. PCC voltage before and after activating the proposed controller (in all cases)

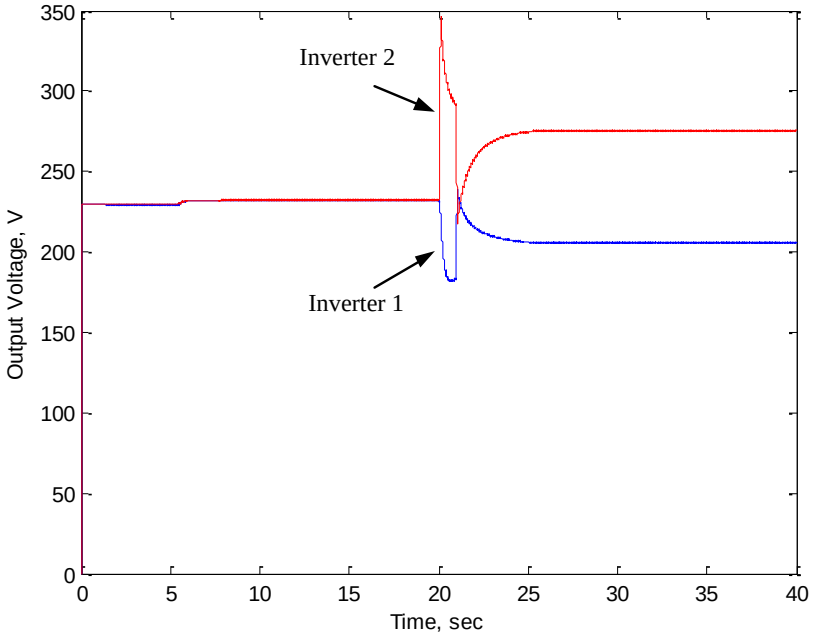

Figure 5.10. Output voltages when PCC voltage is lost at t=20 sec for 100ms

5.5. Experimental Results

A laboratory-scale microgrid that has been built in Chapter 3 is used to validate the proposed controller. The experimental setup parameters are listed in Table 5.3. A detailed simulation model of the experimental setup was also built using Matlab SimPowerSystem.

Figure 5.11 shows reactive power flows from the two inverters during the entire process. The initial PCC load was Load 1 as defined in Table 5.3. The microgrid was initially operating using the traditional droop method. The inverters do not share reactive power equally due to the mismatch in feeder impedances. Stage 1 began at t=5.5 sec and when t = 20 sec the Q sharing was achieved due to the integral controller using V_{PCC}. By the end of stage 1, the new droop gain and the voltage offset were calculated to be used in the next stage. Stage 2 began at t=20.5 sec and the controller switched to traditional droop method using the

new calculated droop gain and the integral controllers using V_{PCC} was stopped. At the beginning of stage 2, the voltage offset is added gradually using a ramp function and the whole process finished at t=26 sec. At t=32 sec, a step load was applied by connecting Load 2 at the PCC and the two inverters shared it equally. The figure, also, shows the inverters' output voltage responses during the whole process. The experimental results show good agreement with the simulation results and confirm the reliability of the proposed controller against load changing.

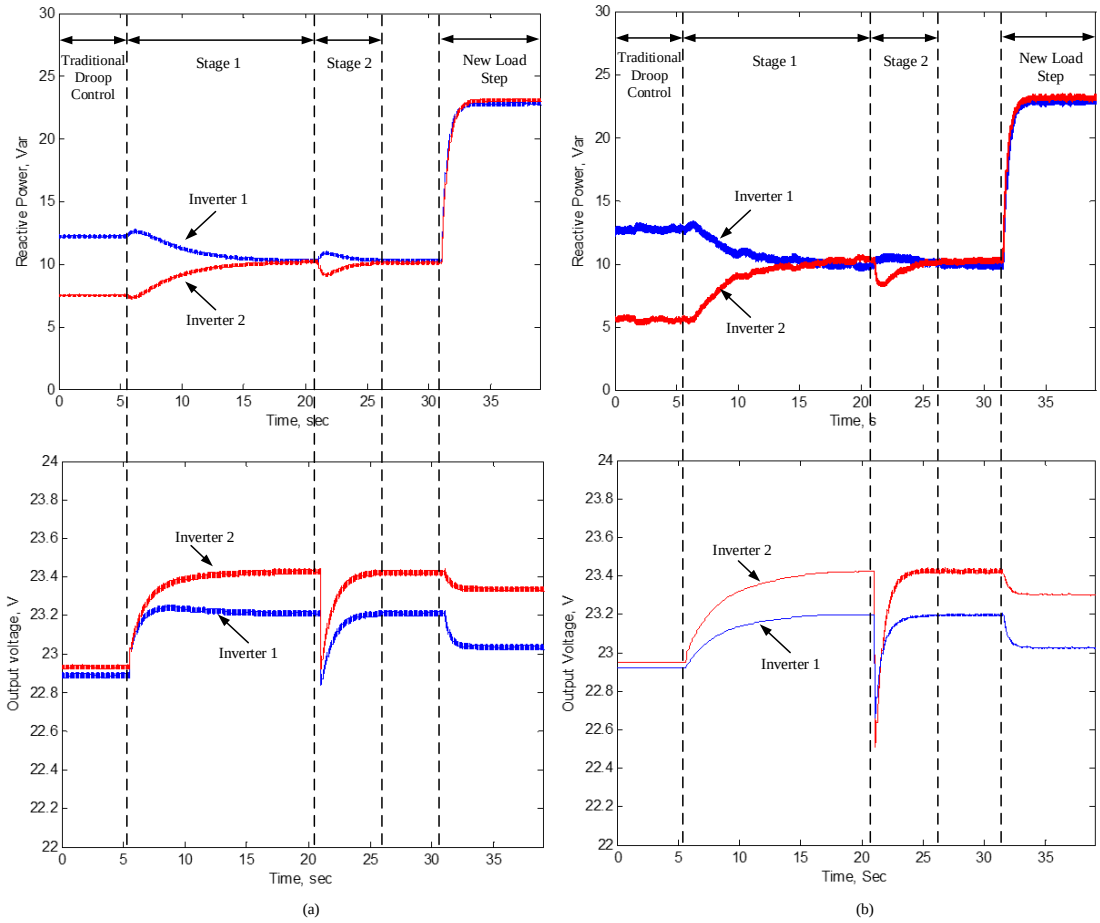

Figure 5.11. Reactive output power and output voltages results of the proposed controller: (a) simulation (b) experimental

Symbol	Description	Value
L_1	Inverter-side filter inductor	1400µH
C	Filter capacitor	240µF
L_2	Grid-side filter inductor	300µH
C_{DC}	DC link capacitor	2000µF
f_s	Sampling frequency	20kHz
f_{sw}	Switching frequency	10kHz
X_f	Feeder line impedance	500µH
m	Frequency droop gain	0.01
n	Voltage droop gain	0.01
V_o	Voltage set point	23 Vrms
Load 1	Load 1 active and reactive power parameters	80W, 15Var
Load 2	Load 2 active and reactive power parameters	27Var

Table 5.3 Experimental parameter values

5.6. Conclusion

In this chapter, a novel power-sharing algorithm was proposed to enhance the reactive power sharing between parallel inverters in island mode. The proposed strategy uses intermittent measurement of the PCC voltage to accomplish improved reactive power sharing. Under this condition it is possible to estimate the value of the output impedance of the inverters (assumed to be dominantly inductive), including that of the cables. The new estimated impedance values are then used to calculate a new value for the gain of a traditional droop controller that takes over control of reactive power sharing when the PCC voltage measurement is not available. The new droop configuration improves the reactive power sharing without needing to measure the PCC voltage continuously. Intermittent measurements could be repeated and transmitted to the inverters over a slow communication link to handle any changes in the network. This increases the reliability of the system against the communication

link loss. As the proposed controller assumes predominant inductive output impedance, this might decrease the sharing accuracy when it has significant resistive value. In addition, the discrete measurement of PCC voltage is managed according to the changes on the structure of the microgrid (loads, cables length and number of inverters). Finally, the simulation and experimental results are presented to validate the performance and effectiveness of the proposed controller.

CHAPTER 6 IMPEDANCE INTERACTION BETWEEN ISLANDED PARALLEL VOLTAGE SOURCE INVERTERS AND THE DISTRIBUTION NETWORK

6.1. Introduction

When controlling a microgrid, it is important to ensure the stability of each unit as well as the microgrid as a whole under different loads and system conditions. In many practical scenarios, the DGs are located far away from each other and therefore they are connected to the network via cables with non-negligible impedance. This could cause the voltage controllers of DGs working in parallel to become unstable. In this chapter, the effect of the inductive virtual impedance as well as cables' length on the stability of parallel-connected inverters is studied. A controller based on the second derivative of the output capacitor voltage is proposed to enhance the stability of the system. The proposed controller ensures stability over a range of cable impedance and virtual impedance values.

6.2. System modelling

Figure 6.1 shows an islanded microgrid consisting of two inverters and their LC filters, cables and load. The parameters of the system considered in this chapter are listed in Table 6.1. Figure 6.2 shows a block diagram of one inverter and its basic controller. It consists of an outer feedback loop of the capacitor voltage V_o and an inner feedback loop of the capacitor current I_c with the latter

employed to provide damping to the filter resonance. In addition to the dual feedback loops of V_c and I_c, a feedforward loop of the reference voltage is also implemented because it has been shown to minimise the steady state error. Furthermore, a virtual impedance loop is used to make the output impedance of the inverter more inductive and hence increase the performance of the droop control.

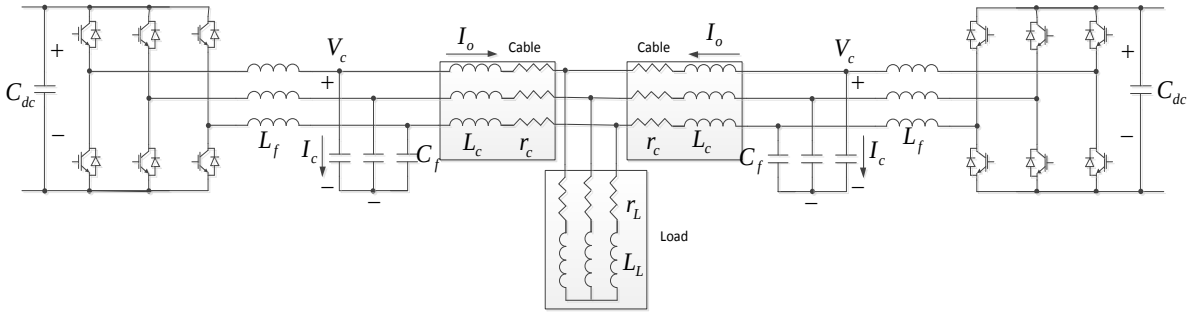

Figure 6.1. Islanded Microgrid Structure

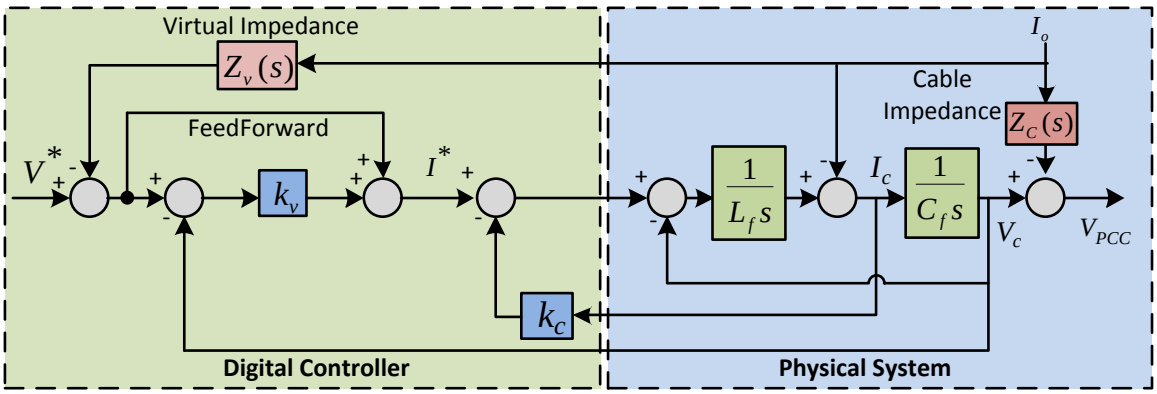

Figure 6.2. The basic double-loop voltage controller of an inverter

It can be shown from Figure 6.2 that the output voltage is given by

$$V_o(s) = G(s)V^*(s) - Z_o(s)I_o(s) \tag{111}$$

where $G(s)$ is the closed loop transfer function that relates V_o to V^* and $Z(s)$ is the closed loop output impedance and they are given by

$$G(s) = \frac{k_v + 1}{L_f C_f s^2 + k_c C_f s + k_v + 1} \tag{112}$$

$$Z_o(s) = \frac{L_f s}{L_f C_f s^2 + k_c C_f s + 1 + k_v} + G(s) Z_v(s) \tag{113}$$

Symbol	Description	Value
L_f	Inverter-side filter inductor	800μH
C_f	Filter capacitor	60μF
k_v	Voltage controller loop gain	2
k_c	Current controller loop gain	2.2
r_c	Cable resistance	$0.5\times10^{-3}\Omega/m$
L_c	Cable inductance	$1\mu H/m$
L_v	Nominal virtual inductance	650μH
τ	Time constant (virtual impedance)	1/1500

Table 6.1 System Parameter Values

The virtual impedance transfer function $Z_v(s)$ in (113) is given by

$$Z_v(s) = \frac{s}{\tau s + 1} L_v \tag{114}$$

where L_v is the inductance of the virtual impedance and τ is the time constant of the high pass filter used to approximate the derivative in the transfer function of the ideal virtual inductance ($Z_v = s.L_v$).

Figure 6.3 shows the Thévenin equivalent circuit of a simple single inverter model represented by (10).

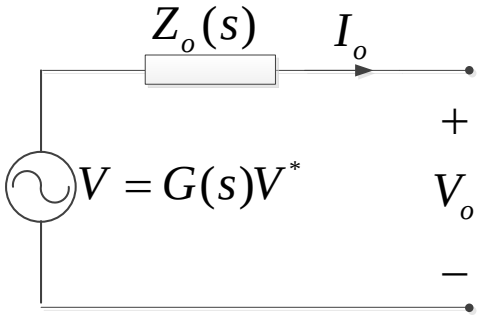

Figure 6.3. Simple inverter model (Thévenin equivalent circuit)

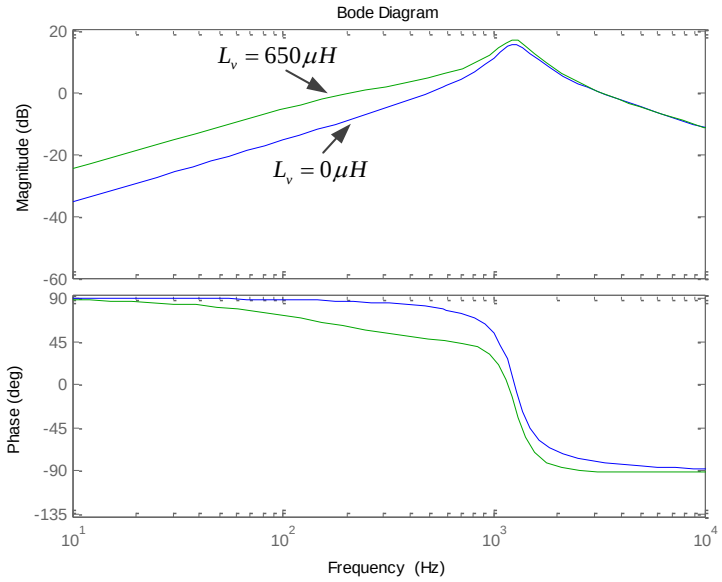

Figure 6.4. Bode plot of output impedance with/without virtual impedance

Figure 6.4 shows the frequency response of the output impedance transfer function $Z_o(s)$ with L_v equals to zero and 650μH. As can be seen, the output impedance has a predominant inductive behaviour in the region below the natural frequency that is important for proper droop control operation, especially, around the fundamental frequency. There is a resonance at the natural frequency but it has been damped thanks to the inner current loop.

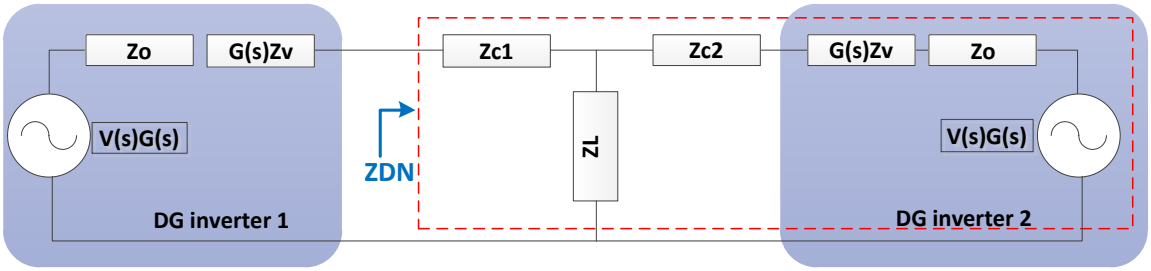

Figure 6.5. General microgrid model including the inverters and output impedance

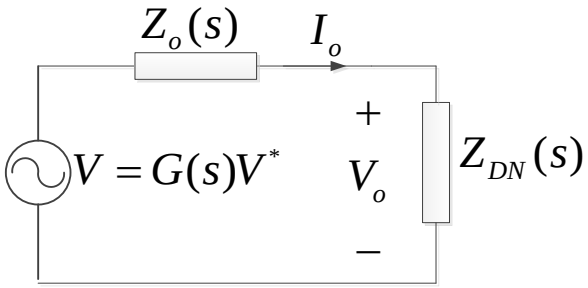

Figure 6.6. Simplified Model of an network side impedance

A circuit model for a microgrid consisting of two inverters connected through cables and supplying a common load is shown in Figure 6.5 where Z_{c1} and Z_{c2} are the impedances of the connecting cables. Using the superposition principle, i.e., by setting the voltage of the second inverter to zero, i.e., $G(s).V^*(s) = 0$, the microgrid from the point of view of the first inverter can be modelled as shown in Figure 6.6 where $Z_{DN}(s)$ represents the equivalent impedance of the load, cables and the output impedance of the second inverter. The load impedance in this chapter will be assumed very high (i.e., open circuit). This

represents the worst-case scenario for resistive loads, as the load resistivity will increase the system damping. Therefore, the equivalent impedance $Z_{DN}(s)$ is given by

$$Z_{DN}(s) = Z_{c1}(s) + Z_{c2}(s) + Z_o(s) \tag{115}$$

From Figure 6.6, the output voltage can be written as

$$V_o(s) = \frac{G(s)V_c^*(s) \times Z_{DN}(s)}{Z_o(s) + Z_{DN}(s)} \tag{116}$$

Equation (116) represents the closed loop transfer function relating the output voltage V_o to the reference voltage V^* taking into account the effect of the connecting cables and the impedance of the other inverters.

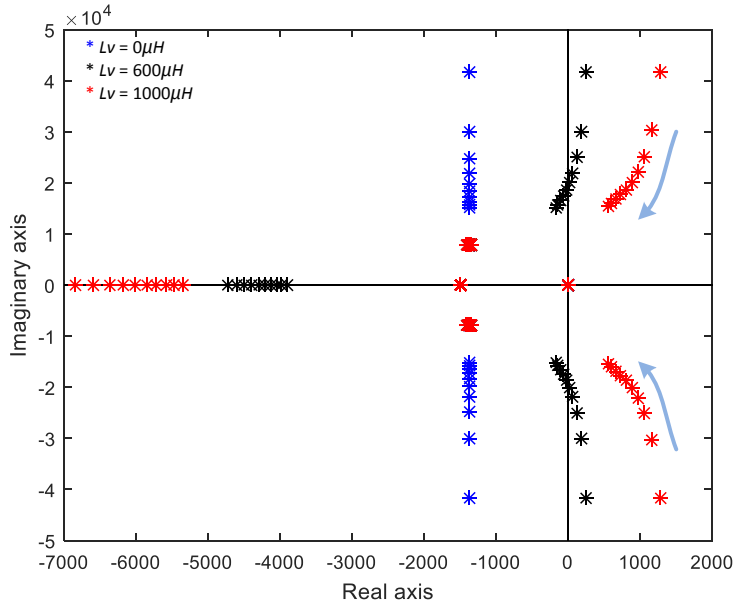

Figure 6.7. Root locus when cable length varies from 10m to 100m, for value of L_v of 0, 600 and 1000μH

6.3. Stability Analysis

From (116), the root locus of the characteristics equation (117), can be used to analyze the system stability as it represents the characteristics equation as

$$Z_o(s) + Z_{DN}(s) = 0 \tag{117}$$

The interaction between an inverter with the network containing cables and other inverters can be addressed using equation (117) in terms of the value of the virtual impedance and the length of cables.

The effect of the virtual impedance on stability is illustrated with the aids of the root locus as shown in Figure 6.7. In this figure, the effect of cables length, change from 10m to 100m, on the closed loop poles of the system is shown for three virtual impedance values of 0, 600 and 1000μH; the arrows show the direction of increase of the cable length. As depicted, high values of virtual inductance (above 600μH) make the system unstable. This can be explained to be due to the increase of the high frequency gain. The cable impedance also has a significant effect on the system. A combination of a short cable and a high virtual impedance value can destabilize the system. Increasing the length of the cable and hence its resistance improves system stability as expected.

6.4. Proposed controller

To improve the stability of the system we propose employing a feedback of the voltage second derivative to present more damping for the complex poles and shift them farther to the left. The new proposed controller is shown in Figure 6.8.

As known, the capacitor current is given by the derivative of the voltage across it,

$$I_c = C_f \frac{dV_c}{dt} \tag{118}$$

The second derivative of voltage can be therefore used to obtain the derivative of the capacitor current as:

$$\frac{dI_c}{dt} = C_f \frac{d^2V_c}{dt^2} \tag{119}$$

Hence, the extra damping term could be realized by the first derivative of capacitor current, which presents a PD^2 controller instead of PD controller as shown in its simplified version in Figure 6.9.

The PD^2 controller measures the change of rate of current change of rate that could reduce the disturbance effects on the system if proper gain is used to reject these disturbances.

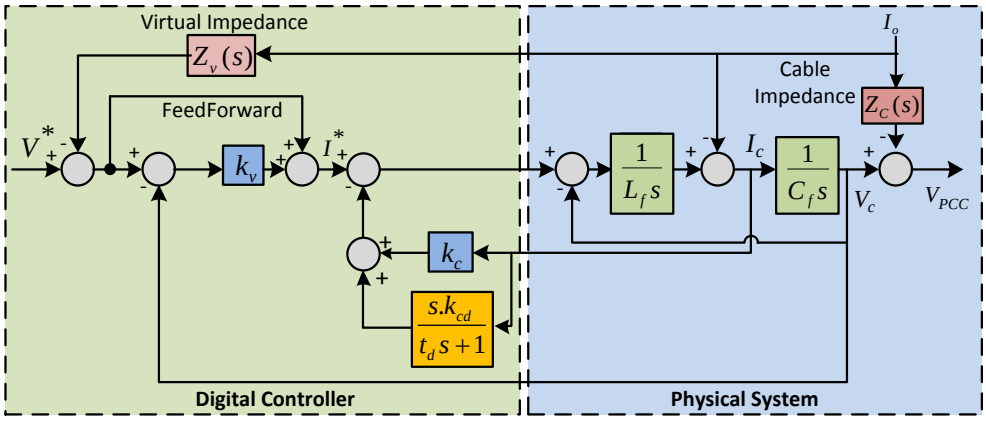

Figure 6.8. The proposed voltage controller

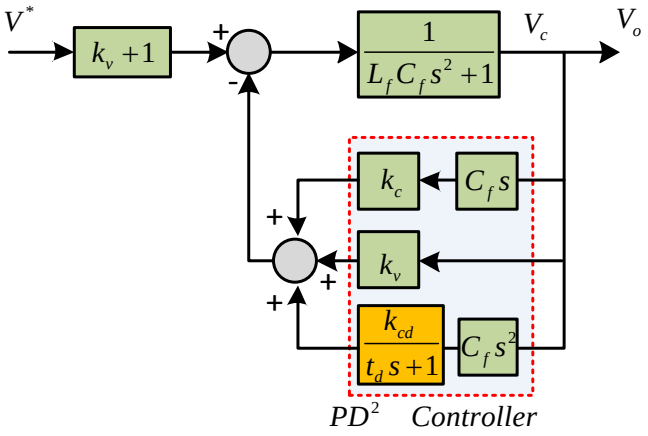

Figure 6.9. The simplified proposed voltage controller loop

The first derivative already can be measured directly by sensing the capacitor current. However, the second derivative needs to be calculated. Differentiation of the high-frequency capacitor current may cause serious noise multiplication problems that could lead to instability. Therefore, a low pass filter is added after the derivative term to minimize the effect of the high frequency on system stability. The full derivative followed by low pass filter is stated as:

$$s.I_c.\frac{1}{\tau_d s+1} \tag{120}$$

where τ_d is the time constant of the filter.

The new version of the voltage closed loop transfer function is calculated as stated in (121), where k_{cd} is the derivative gain of the capacitor current,

$$G_p(s)=\frac{(k_v+1)\tau_d s+k_v+1}{L_f.C_f.\tau_d s^3+(L_f.C_f+C_f.k_c.\tau_d+C_f.k_{cd})s^2+(k_c.C_f+\tau_d(k_v+1))s+k_v+1} \tag{121}$$

The new output impedance is obtained from Figure 6.8, with considering the virtual and cable impedances, as

$$Z_{op}(s)=\frac{L_f\tau_d s^2+L_f s}{L_f.C_f.\tau_d s^3+(L_f.C_f+C_f.k_c.\tau_d+C_f.k_{cd})s^2+(k_c.C_f+\tau_d(k_v+1))s+k_v+1}+G_p(s)Z_v(s)+Z_C(s) \quad (122)$$

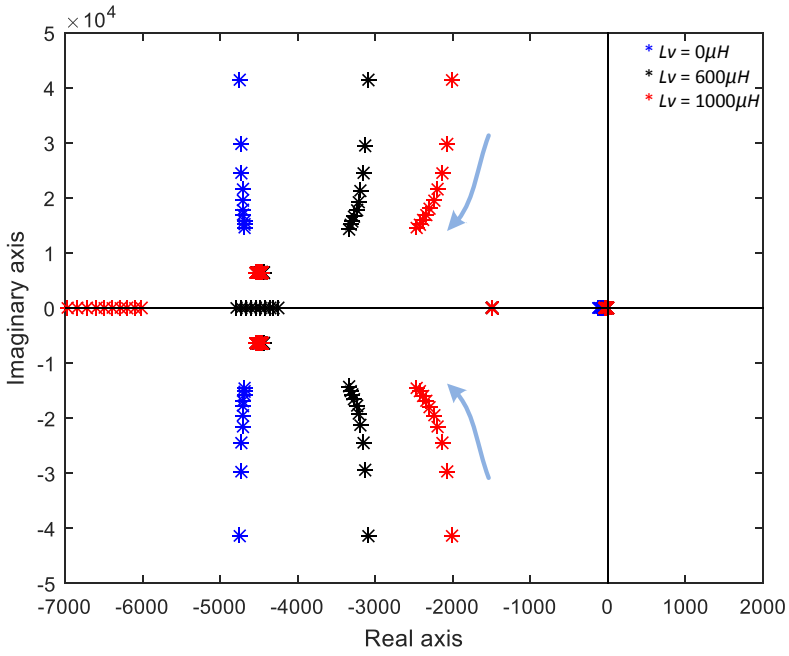

Figure 6.10. Root locus with the proposed controller as the virtual inductance and cables length varies from 10-100 m

Figure 6.10 illustrates the effect of the proposed controller on stability. The root locus now shows that the system is stable for the range of virtual inductance values and cable lengths.

Figure 6.11 illustrates the locus of $G_P(s)$ when k_{cd} varies from 0 to 0.1 where $\tau_d = 0.02$. As shown, it shifts the oscillated components far away from the imaginary axis thus increasing stability.

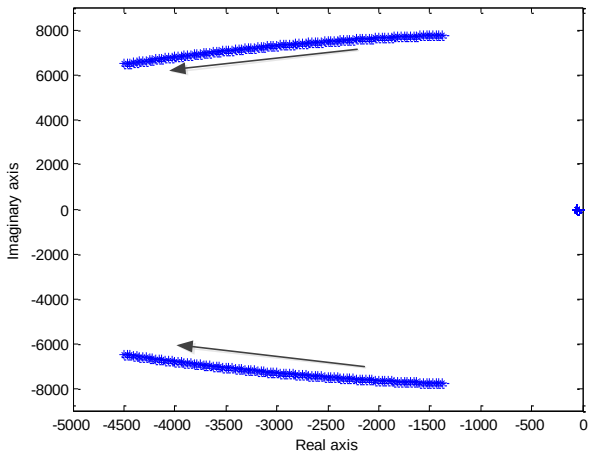

Figure 6.11. Root locus of the voltage controller when k_{cd}varies from 0 to 0.1

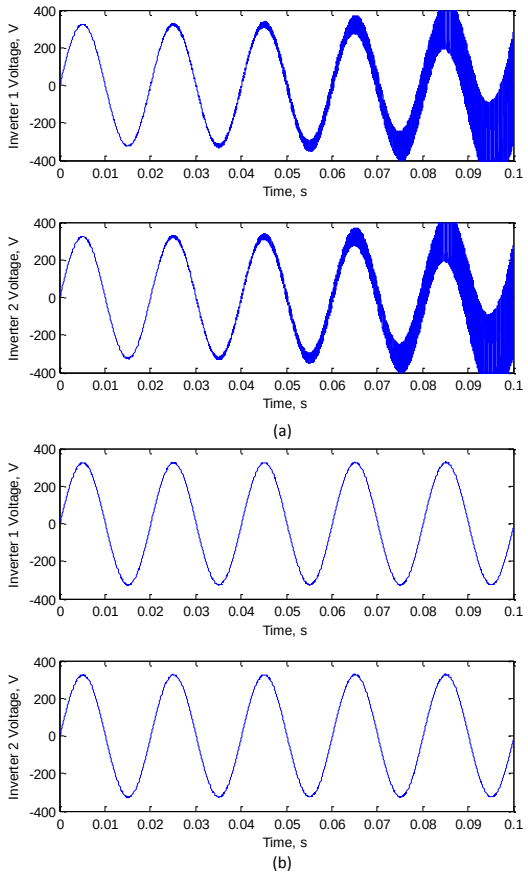

Figure 6.12. Output voltages of the two inverters without (a) and with (b) the proposed control loop

6.5. Simulation results

Matlab model was built, as shown in Figure 6.5, including two single-phase inverters modelled by two-leg IGBT bridge and voltage controller with capacitor voltage and current as feedback signals. They are connected via cables lengths 10m and 20m respectively. The model parameters are listed in Table 6.1. The voltages of the inverters are shown in Figure 6.12 with and without the proposed controller. As shown, the system without the proposed controller is unstable as expected from the previous analysis while the stability is achieved with the proposed controller.

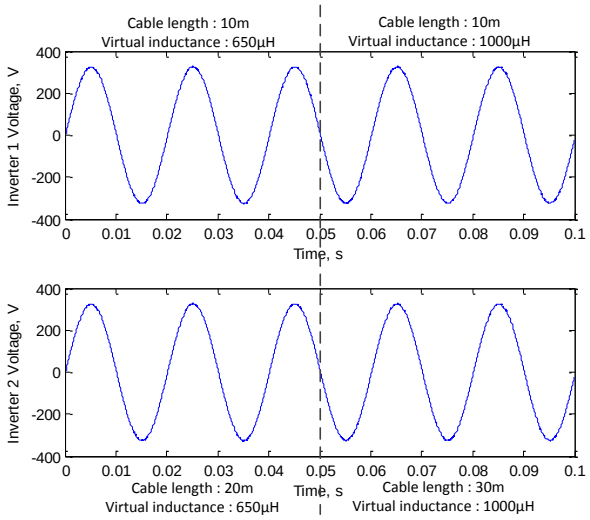

Figure 6.13. Output voltages of the two inverters with the proposed control loop when the cable length and virtual inductance vary

More results are obtained with the proposed controller shown in Figure 6.13. The cable length of the second inverter has changed from 20m to 30m at t= 0.05 sec concurrently with an increment step of the virtual inductance from

650µH to 1000µH. The results confirm the stability and illustrate the robustness of the proposed controller against different network and controller conditions.

6.6. Discussion

Recalling equations (121) and (122), it can be noted that the gain k_c has a tandem effect gain on the s^2 term as k_{cd}. However, it influences the s term also. This could damp the resonance and save the stability for some limit but it introduces more phase shift in the voltage controller loop that affects the tracking ability as shown in Figure 6.14. The figure depicts the closed loop voltage controller bode plot when high k_c is compared with lower k_c with the presence of k_{cd}. Although the values are adjusted to give the same bandwidth, the phase shift is less when k_{cd} is adopted.

If the discretising process is included as all signals should be sampled, this will present another term of comparison. When the sample and hold operation is taken into account by merging the ZOH process in the transfer function, the advantage of the derivative term clearly appears in Figure 6.15 that shows the root locus of the discretised system. A high value of k_c destabilizes the system while it is stable in the case of k_{cd} and low k_c. These values again are chosen to give the same voltage controller bandwidth.

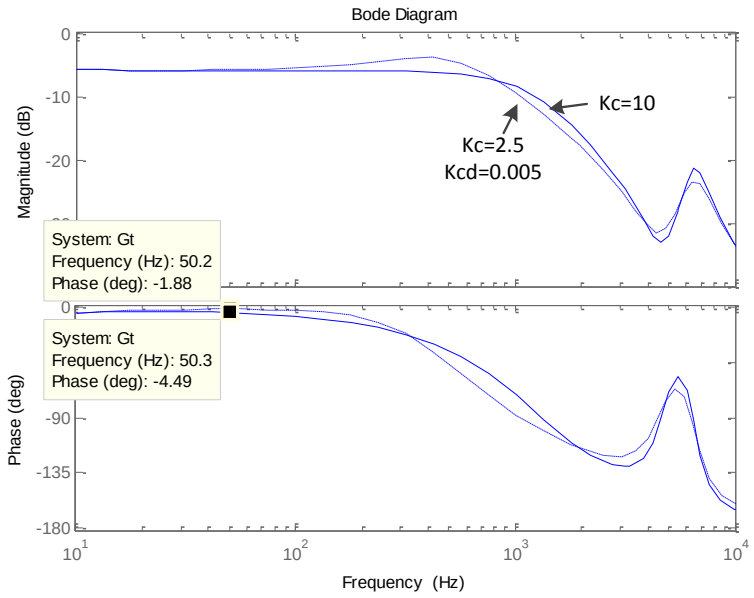

Figure 6.14. Bode plot of the closed loop of the voltage controller

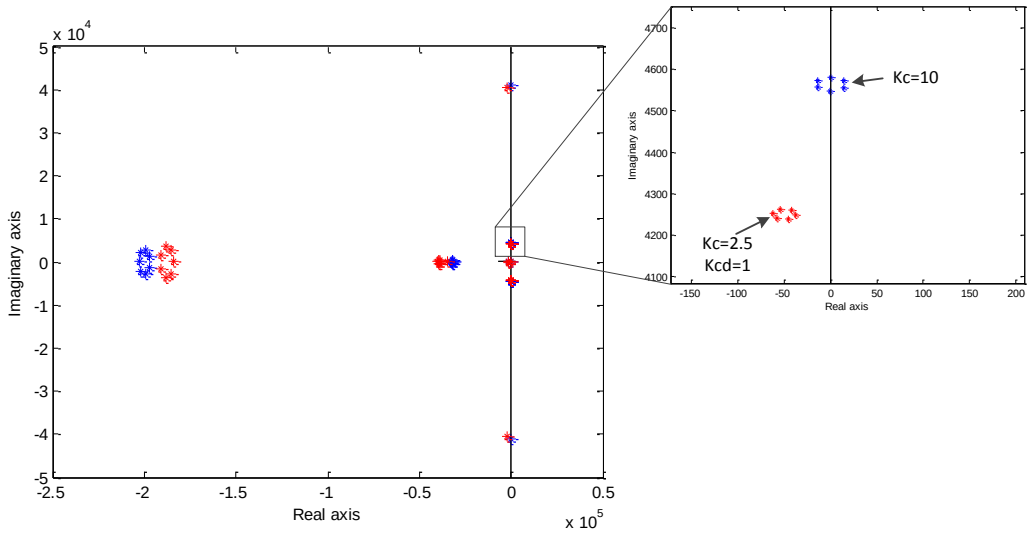

Figure 6.15. Root locus of a discretized system

6.7. Conclusion

This chapter studies the interaction between the output impedance of microgrid inverters and the network impedance including interconnecting cables and the impedance of other parallel inverters. This interaction can destabilize the whole system. A novel controller that uses a feedback loop of the second derivative of the inverter's output voltage has been proposed to enhance the system stability. Matlab simulation results have verified the theoretical analysis and the validity of the proposed controller.

CHAPTER 7 CONCLUSIONS AND FUTURE WORK

7.1. Conclusions

In both modes of microgrid operation, it is important to ensure the stability of each unit as well as the whole lumped system. Furthermore, the mode switching should be seamless under all different loading and system conditions. In this thesis, we present advanced control strategies for smart microgrids with detailed analysis and methodologies. Some of these have not been addressed in the literature to date. The general conclusions of this thesis can be summarized as:

1. State of the art renewable energy interfacing technology and microgrid control techniques in both modes have been reviewed. The literature revealed that the droop control is a common recent used technique for wireless power sharing. However, it suffers from several disadvantages which the researches are going to improve. The review also illustrated additional problems that haven't been addressed like unintentional islanding issues.
2. Analysis has been carried out to study the interaction between island parallel inverters when they transfer from grid-connected mode to island mode unintentionally, particularly, in the case of low load and different power set-points. This clarified the action of the droop control, and how it shifts the frequency of the microgrid leading some inverters to import power, and then converting this power to a voltage rise across the DC link capacitor.

3. A small signal model of two islanded inverter, which used for studying the unintentional islanding effect on the power flow between the inverters and the issue of a DC link voltage rise that decreases the system reliability, has been developed. It is obtained by perturbing the states of the system around equilibrium points and constructing a state space matrix that represents the inverter's dynamics. This model is utilized as an analysis and a design tool to evaluate the parameters of the system and its effect on the stability besides selecting the proposed controller parameters to satisfy the system responses requirements.
4. A model validation has been implemented using a Matlab/Simulink model and a practical setup model. The validation emphasized the accuracy of the small signal model to predict the system states behaviour around the equilibrium points.
5. A new control strategy for droop-based inverters, that reduces the circulating currents and limits the DC link voltage rising during unintentional islanding, has been proposed. This controller increases the reliability of the system as it prevents the DC link voltage to trip an inverter. In addition, it contributes into a seamless transfer from grid-connected mode to island mode and saves the system against a grid loss. It is better to take DC link capacitance into account during the design process of the inverter hardware. Low capacitance value can cause the overvoltage to reach the trip point faster which will limit the controller performance.
6. An enhanced reactive power sharing controller for islanded inverters, which decreases the dependency on the communication links between

each unit and the MGCC, has been proposed. This mitigates the risk of the system instability if the link has been lost. The controller uses the voltage at PCC via communications to share the reactive power accurately among the inverters. Concurrently, it estimates the dominant inductive output impedance and then calculates new voltage droop gains. These gains improve the power sharing without using the PCC voltage anymore. Consequently, using this controller, each inverter wirelessly enhances the sharing accuracy compared to the traditional droop controller. The performance of the controller has been validated by simulation and practical work under different load conditions. The performance of the controller can deteriorate if the output impedance has a non-negligible resistive value because the estimation process assumes inductive impedance of the interconnecting cables. An alternative estimation process needs to be used in this case.

7. The effect of cable impedance on the stability of a microgrid containing many parallel-connected inverters has been studied. An impedance model has been developed to study the interaction between each inverter with the rest of the network including the cables and other parallel inverters. A stability study has been presented in terms of the length of the cables which revealed a resonance generation in some cases due to the impedance interaction of an inverter with the distribution cables impedances. In addition, a controller, based on the second derivative of the capacitor voltage that increases the stability margins of the entire system and mitigate the resonance, has been proposed. Because the controller uses a derivative action, its practical

implementation might cause noise amplification. Therefore, good care should be taken in the practical implementation.

7.2. Future Work

The current major grid transformation and the increasing penetration of the renewable energy sources is leading the research to produce more advanced control techniques to ensure the robustness of microgrid operation. Based on the outcomes obtained in this thesis, a number of areas for further development of this research are proposed as follows:

1. Based on the model developed in Chapter 4, the same strategy might be adopted to develop a multi-inverter model to study the issue of unintentional islanding and the transient's variations against the number of integrated units and the power set-point differences.
2. Based on the model and the proposed controller for the multi-inverter microgrid, a practical validation of the model and the performance of the PD controller might be implemented.
3. A constant impedance load is considered in the study of unintentional islanding issue in Chapter 4. Other load types, i.e. constant power or constant current loads, could be addressed as well.
4. Validating the new controller developed in Chapter 6 with experimental results.
5. The interactions between AC and DC microgrids (Hybrid microgrids), during both types of operation and its effect on the power flow between all units, might be studied. This work will expose new challenges of modelling and practical work.

6. A supervisory control development might be introduced to govern the amount of power of each unit, in particular, when solar, wind or battery energy sources are used. The different geographical and weather conditions present several challenges also which require the control algorithms to be flexible.

APPENDIX

Appendix A: Inverter Module input and output signals

1. IGBTs

The IGBT switches are utilized to convert the DC voltage applied on the DC link bus to an AC power signal. The DC Link bus bars have a film capacitor incorporated in the module, which eliminates the need for high frequency snubber capacitors.

2. Sensors

The SKAI module has integrated magneto resistive current sensors that are used by an integrated circuit for protection purposes but they can also be used by the user for control. The measured current is the filter inductor current I_{L1}. However, this is not used in this setup because the controller used in this research is adopting the filter capacitor current I_c as the inner feedback loop instead of I_{L1}. Thus, the filter capacitor current I_c is measured by an external current sensor.

3. Driver Board

The SKAI driver board provides all the necessary interface circuitry for gate drives, voltage, current, and temperature measurements, fault protection, and isolation so that the user only needs to provide logic level PWM signals for each switch. The SKAI uses a standard D-sub 25 pin connector and the pin-out of it is shown in Table A.1.

D-sub 25 pin	Signal	Remark
1	BOT HB 1 IN	+5 – 15V CMOS logic
14	ERROR OUT	Fault monitoring – Low = No Error , Open collector output
2	TOP HB 1 IN	+5 – 15V CMOS logic
15	BOT HB 2 IN	+5 – 15V CMOS logic
3	ERROR OUT	Fault monitoring – Low = No Error , Open collector output
16	TOP HB 2 IN	+5 – 15V CMOS logic
4	BOT HB 3 IN	+5 – 15V CMOS logic
17	ERROR OUT	Fault monitoring – Low = No Error , Open collector output
5	TOP HB 3 IN	+5 – 15V CMOS logic
18	Over Temp OUT	Over temperature monitoring – Low = No Error , Open collector output
6	GND	Signal reference
19	U_{DC} analogue OUT	Analogue voltage proportional to the DC link voltage
7	PWR	+24 V IN
20	PWR	+24 V IN
8	+15 VDC OUT	+15 V OUT
21	+15 VDC OUT	+15 V OUT
9	GND	Supply & Signals reference
22	GND	Supply & Signals reference
10	Temp analogue OUT	Analogue voltage proportional to the heat sink temperature
23	REF 1	Reference for phase 1 current sensor, GND
11	I analogue OUT HB 1	Analogue voltage proportional to phase 1 current
24	REF 2	Reference for phase 2 current sensor, GND
12	I analogue OUT HB 2	Analogue voltage proportional to phase 2 current
25	REF 3	Reference for phase 3 current sensor, GND
13	I analogue OUT HB 3	Analogue voltage proportional to phase 3 current

Table A.1 Pin-out of SKAI module

The 6 input signals TOP1, BOT1, TOP2, BOT2, TOP3, and BOT3 drive the 6 IGBT switches. Since all the switches are controlled independently, the module

can be configured as single phase H-bridge DC/AC converter, DC/DC buck or boost converter.

4. Inputs - Drive Signals

The PWM input signals, BOT HB 1, TOP HB 1, BOT HB 2, TOP HB 2, BOT HB 3, and TOP HB 3, generate the switch commands for the 6 switches. The high voltage level should be either 5 or 15V CMOS logic and the low voltage level is 0V. Logic High turns the switch on while logic low turns the switch off.

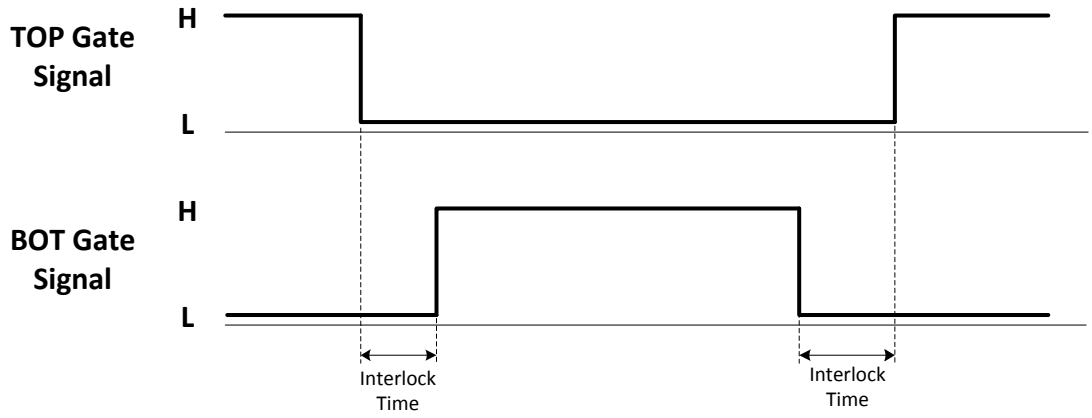

Figure A.1 Interlocked time pulse pattern

5. Interlock Time

The driver board prevents switch cross conduction by only allowing one switch in a phase to be on at a time and ensuring an interlock time between the turn-off of one switch and the turn-on of the other switch in a phase as in Figure A.1. The default interlock time between TOP and BOT turn on is set to 2 us. The interlock time is not simply added to the TOP and BOT signals. If the TOP and BOT signals have greater than the set minimum interlock time then the TOP

and BOT signal propagate through with no timing change. The interlock protection only guarantees a minimum interlock time.

6. Outputs – Analogue

The driver board provides analogue signals representing the DC link voltage, the heat sink temperature and phase currents.

a. UDC analogue OUT

Pin 19 of the interface connector is the UDC analogue OUT pin. It is an analogue signal proportional to the DC link voltage. The maximum analogue signal is 9 V and it has a scaling factor of 100.

b. Temp analogue OUT

Pin 10 of the interface connector is the Temp analogue OUT pin. It is an analogue signal proportional to the temperature of the SKAI heat sink. The temperature sensor range is from 20^{o}C to 120^{o}C and generates a 0 to 10 V signal proportionally.

7. Phases currents

Pins 11, 12, and 13 of the interface connector are the current analogue OUT of each bridge leg. They are the analogue signals proportional to the current in each half bridge phase.

8. Driver Board Power Supply

The SKAI driver board requires a supply of DC input voltage between 8 – 30VDC and 16W.This is supplied to the PWR and GND pins. An integrated power supply provides all necessary voltages for the driver and generates a regulated +15V for external circuits usage.

9. Error Signals

Pins 3, 14, and 17 of the interface connector are tied together to give an ERROR OUT signal in case of inverter fault such as over current, over voltage, or over temperature. This is an open collector output that must be pulled high by an external pull-up resistor. LOW equals no error. This signal reports an error for a VCE fault on any switch, over current on any phase, over voltage of the DC link, under voltage of the +15 V supply, and over temperature of the heat sink. When an error is detected and reported all switching is inhibited and all switches are turned off. In order to reset the control board and start switching again all fault conditions must be removed and all TOP and BOT input signals must be low for at least 9 us. The different causes for the ERROR signal are explained below.

a. VCE Fault

If the switch current is excessive, the switch will come out of saturation and be detected as a VCE fault and report an error on the ERROR pins.

b. Over Current

If the current through a phase is excessive, an over current event from the current sensor will be detected and report an error on the ERROR pins.

c. DC Link Over Voltage

If the DC Link voltage exceeds 102% of its maximum rating, an over voltage event will be detected and report an error on the ERROR pins.

d. +15 V Supply Under-Voltage Lockout

If the +15 V on the SKAI board falls below 13 V, an under voltage event will be detected and report an error on the ERROR pins.

e. Overtemp OUT

Pin 18 of the interface connector is the Overtemp OUT pin. It is an open collector output that must be pulled high by an external pull up resistor. LOW equals no error. This signal reports an over temperature condition of 115^{o}C on the SKAI heat sink. If there is an over temperature error, both this pin and the ERROR OUT pins will indicate an error.

Control of Transient Power during Unintentional Islanding of Microgrids

Walid Issa, Mohammad Abusara and Suleiman Sharkh, IEEE Member

Abstract – In inverter-based microgrids, the paralleled inverters need to work in grid-connected mode and stand-alone mode and to transfer seamlessly between the two modes. In grid-connected mode, the inverters control the amount of power injected into the grid. In stand-alone mode, however, the inverters control the island voltage while the output power is dictated by the load. This can be achieved using the droop control. Inverters can have different power set-points during grid-connected mode but in stand-alone mode they all need their power set-points to be adjusted according to their power ratings. However, during sudden unintentional islanding (due to loss of mains), transient power can flow from inverters with high power set-points to inverters with low power set-points, which can raise the DC link voltage of the inverters causing them to shut down. This paper investigates the transient circulating power between paralleled inverters during unintentional islanding and proposes a controller to limit it. The controller monitors the DC link voltage and adjusts the power set-point in proportion to the rise in the voltage. A small signal model of an islanded microgrid is developed and used to design the controller. Simulation and experimental results are presented to validate the design.

Index Terms – microgrid, droop control, power sharing, unintentional islanding.

NOMENCLATURE

P^*, Q^*	Active and reactive power set-points
P, Q	Instantaneous active and reactive power
R	Load resistance
X	Inverter output inductance
k_ω, k_a	Frequency and voltage drooping gains
V_o, ω_o	Voltage and frequency set points
τ	Measurement filter time constant
V^*_{DClink}	Nominal DC link voltage
C_{DC}	DC link capacitor
V_{eq}, θ_{eq}	Voltage and phase equilibrium points

I. INTRODUCTION

The concept of the microgrid has emerged in response to the increased penetration of renewable energy systems. In a microgrid, distributed generation (DG) units, energy storage systems (ESS), and loads are aggregated as one unit connected to the grid via a Static Transfer Switch (STS), as illustrated in Fig. 1. Due to their controllability, microgrids will become the building blocks of future smart grids. Compared to a single DG unit, a microgrid has more capacity and control flexibility, which can improve system reliability and power quality. A microgrid can operate in grid-connected mode or in stand-alone mode. In grid-connected mode, DG units can export power to the grid (when the price is advantageous for example) or import power and store it in ESS for later use. During a power outage, the microgrid works autonomously and provides power to local load. ESS can be used to balance any mismatch between load demand and the power available from renewable sources. To avoid power supply interruption, it is necessary for the microgrid to be able to transfer seamlessly from grid-connected mode to island mode and vice-versa. Low speed communication between the supervisory controller and all units, can be also used for power management and monitoring beside decision-making outcomes transfer.

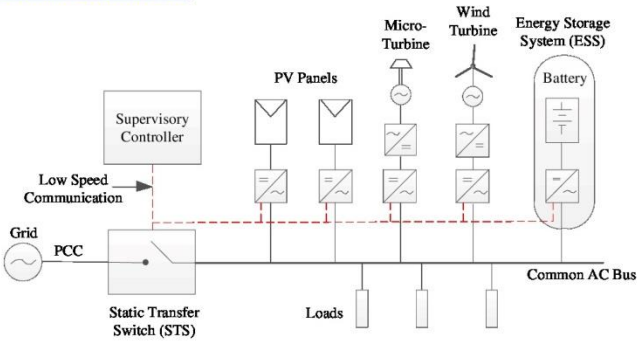

Fig. 1. Microgrid Structure

There are a number of publications on the control of grid interactive PWM inverters [1]-[7]. Chandorkar et al. [8] proposed a grid interactive PWM inverter based on P-ω and Q-V droop control where the inverter frequency and voltage amplitude are drooped linearly with the inverter output active and reactive power, respectively. Inverters can operate in parallel and load sharing is achieved without the need for communication signals between the inverters. Using droop control it is possible for the inverter to transfer from the grid-connected mode to the stand-alone mode seamlessly [11]. During grid-connected mode, the frequency is stiff and maintained by the power grid. Hence, the power set-point of the droop controller can be used to control the power output of the inverter. This power set-point can be adjusted by an energy management system implemented inside the supervisory controller. In stand-

Walid Issa and Mohammad Abusara are with the Renewable Energy Research Group, College of Engineering, Mathematics, and Physical Sciences, University of Exeter, Cornwall Campus, Penryn, TR10 9EZ, U.K. (e-mail: wrmi201@exeter.ac.uk , m.abusara@exeter.ac.uk).
S. M. Sharkh is with the Electro-Mechanical Engineering Research Group, Faculty of Engineering and the Environment, University of Southampton, Highfield Campus, Southampton, SO17 1BJ, U.K. (e-mail: suleiman@soton.ac.uk)

alone mode, however, the frequency can deviate from its nominal value depending on the amount of power drawn by the local load and the power set-point can be used to reduce this deviation.

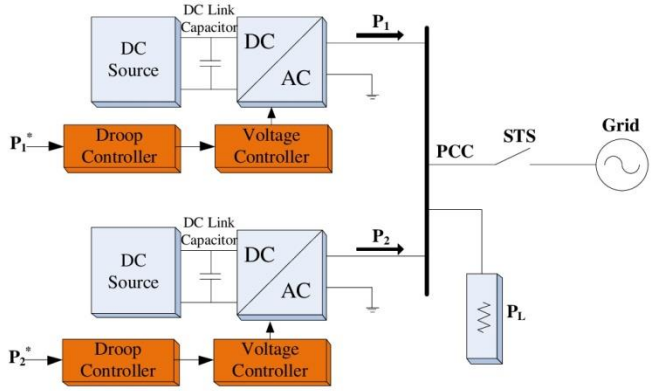

Fig. 2. Two inverters in microgrid

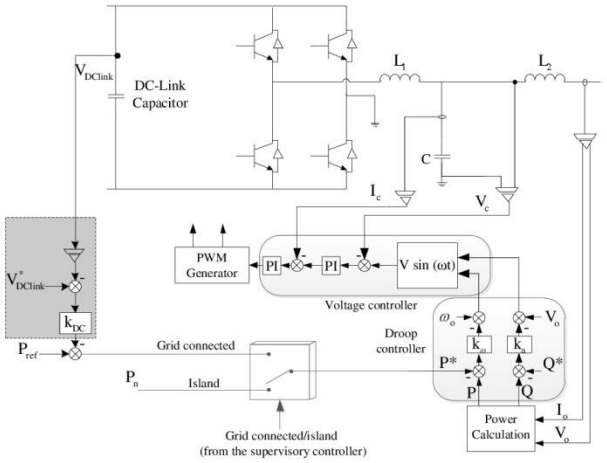

Fig. 3. Inverter circuit diagram

In the case of multiple inverters operating in stand-alone mode, each set-point has to be adjusted according to the power rating of the inverter, i.e. according to the drooping gain. Therefore, the power set-point has two different purposes depending on the mode of operation: 1) in grid-connected mode, power set-point is set to control the output power. 2) In stand-alone mode, it is used to reduce the frequency deviation. Before changing from grid-connected to stand-alone mode the supervisory controller needs to bring all the power set-points of all paralleled inverters to their nominal values before disconnecting from the grid. However, if unintentional islanding occurs, it is not possible to adjust the power set-points to match the load demand instantaneously. As a result circulating power can flow from the inverters with higher power set-points to inverters with lower set-points. It is important to note that by using common anti-islanding strategy, the period from grid failure until the opening of the STS may vary depending on the mismatch between the power generated by the microgrid and the local distributed load. If the mismatch is large, islanding detection will be quite quick. However, if the mismatch is small, it will take longer for the anti-islanding controller to detect grid power loss. In the worst case scenario of perfect mismatch between the power generated and the load, the anti-islanding controller should not take more than 2 seconds according to the IEEE Standard 1547 [10]. If one inverter imports power during this period, the DC link voltage will rise and might exceed the maximum limit. This will cause the inverter to shut down to prevent damage. Even though there has been a number of publications recently on seamless transfer of microgrids [11],[9], and [12], the effect of different power set-points on the transient power between inverters has not yet been discussed.

This paper investigates the issue of transient power between parallel inverters during unintentional islanding. This circulating power can raise the DC link voltage of the inverters causing the inverter to shut down if the voltage level exceeds its maximum limit. The paper also proposes a controller to limit this circulating power by adjusting the power set-point according to the rise in the DC link voltage. A small signal model of a microgrid consisting of two inverters in island mode is developed and used to design the controller. Simulation and experimental results are presented to validate the design. The main contributions of this paper are: 1) Analysis of a microgrid during unintentional islanding and the effect of this on the DC link voltage, 2) Using small signal perturbation to develop a model of an island microgrid of two parallel-connected inverters, 3) The design of a controller that limits the rise of the DC link voltage during unintentional islanding.
The rest of the paper is organized as follows. Section II discusses the droop control operation and analysis of unintentional islanding. Section III presents a small signal model of a microgrid consisting of two inverters. The proposed controller is presented in section IV. Simulation and Experimental results are presented in Section V.

II. DROOP CONTROL

In this paper, a microgrid consisting of two inverters as shown in Fig. 2 is considered. The circuit diagram of each inverter and its LCL filter and controller is illustrated in Fig. 3. The system parameters are listed in Table I. The frequency and voltage droop control laws of an inverter operating in a microgrid is given by

$$\omega = \omega_o^* - k_\omega (P - P^*) \quad (1)$$

$$V = V_o^* - k_a (Q - Q^*) \quad (2)$$

where ω_o^*, V_o^* are the nominal frequency and nominal voltage references, k_ω, and k_a are the frequency proportional drooping coefficient and voltage proportional drooping coefficient, respectively. The droop slopes are determined according to the power rating of the inverter and according to the maximum allowable variations in output frequency and voltage [13]. In grid-connected mode the active and reactive power set-points P^* and Q^* are adjusted to be equal to the reference power values, P_{ref} and Q_{ref}. In stand-alone mode, however, they are set to nominal active and reactive power values, P_n and Q_n, to improve frequency and voltage regulation [11]. The inverter controller receives a signal from the supervisory controller about the status of the STS, and the set-points $P^*$and Q^* are set accordingly as shown in Fig. 3.

represent the closed loop and output impedance transfer functions, respectively [14].The response time of G(s) is quite fast with respect to that of the outer droop control and hence it will be assumed as unity [11].

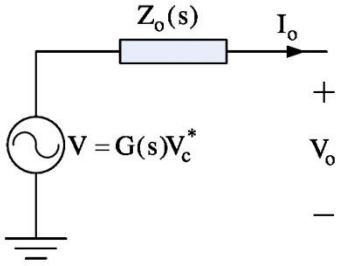

Fig. 6. Inverter equivalent circuit

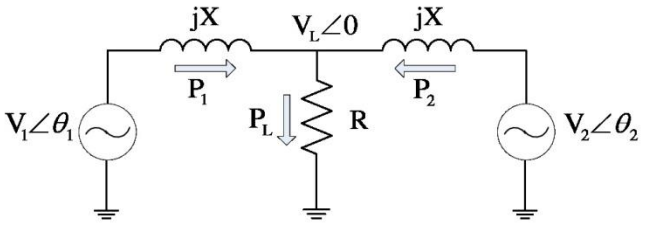

Fig. 7. Equivalent circuit of two inverters in island mode

The output impedance $Z_o(s)$ is predominantly inductive around the fundamental frequency [4],[5],[14] and hence $Z_o(s)$ can be approximated such as $Z_o(s) \approx sL_o$. The inductance L_o can be determined by the slope of $Z_o(s)$ around the fundamental frequency and in the experimental setup used in this paper it is 2500μH. Fig. 7 shows the equivalent circuit for the two inverters operating in island mode. For simplicity, it is assumed that both inverters have identical output impedance $X = \omega L_o$ and they supply a local resistive load.

A. Power flow equations and power measurement

The current that flows from each inverter can be described as follows:

$$I_n = \frac{V_n\angle\theta_n - V_L}{X\angle 90}, \quad n = 1,2 \tag{10}$$

Applying Kirchhoff current law at the load node gives

$$\frac{V_L - V_1\angle\theta_1}{X\angle 90} + \frac{V_L}{R} + \frac{V_L - V_2\angle\theta_2}{X\angle 90} = 0 \tag{11}$$

Rearranging (11), the load voltage is given by

$$V_L = \frac{R(V_1\angle\theta_1 + V_2\angle\theta_2)}{2R + X\angle 90} \tag{12}$$

The apparent power of each inverter is given by

$$P_n + jQ_n = V_n.I_n^*, \quad n = 1,2 \tag{13}$$

Substituting (12) in (10) and the result into (13), the instantaneous active and reactive powers (in the time domain) for the two inverters are given by

$$P_1 = \frac{\frac{XV_1^2}{R} + 2V_1V_2\sin(\theta_1-\theta_2) + \frac{XV_1V_2}{R}\cos(\theta_1-\theta_2)}{4X + \frac{X^3}{R^2}} \tag{14}$$

$$Q_1 = \frac{(\frac{X^2}{R^2}+2)V_1^2 - 2V_1V_2\cos(\theta_1-\theta_2) + \frac{XV_1V_2}{R}\sin(\theta_1-\theta_2)}{4X + \frac{X^3}{R^2}} \tag{15}$$

$$P_2 = \frac{\frac{XV_2^2}{R} + 2V_1V_2\sin(\theta_2-\theta_1) + \frac{XV_1V_2}{R}\cos(\theta_2-\theta_1)}{4X + \frac{X^3}{R^2}} \tag{16}$$

$$Q_2 = \frac{(\frac{X^2}{R^2}+2)V_2^2 - 2V_1V_2\cos(\theta_2-\theta_1) + \frac{XV_1V_2}{R}\sin(\theta_2-\theta_1)}{4X + \frac{X^3}{R^2}} \tag{17}$$

When practically implementing the droop control, average active and reactive powers need to be measured and thus the droop control equations described in (1) and (2) become

$$\omega = \omega_o^* - k_\omega(P_{avg} - P^*) \tag{18}$$

$$V = V_o^* - k_a(Q_{avg} - Q^*) \tag{19}$$

The average power can be obtained by passing the instantaneous powers through a low pass filter as it common and easier to be programmed in a DSP. Hence, the average power P_{avg}, and Q_{avg} in the s-domain, are given by

$$P_{avg} = F(s)P(s) \tag{20}$$

$$Q_{avg} = F(s)Q(s) \tag{21}$$

where P(s) and Q(s) are the instantaneous active power and reactive power, respectively as described in equation (14)-(17). F(s) is the transfer function of the LPF and is given by

$$F(s) = \frac{1}{\tau s + 1} \tag{22}$$

where τ is the filter time constant.

B. State Space Equations

By perturbing the power flow equations (14)–(17) we obtain,

$$\Delta P_1 = a_1\Delta V_1 + b_1\Delta V_2 + c_1\Delta\theta_1 + d_1\Delta\theta_2 \tag{23}$$

$$\Delta P_2 = a_2\Delta V_1 + b_2\Delta V_2 + c_2\Delta\theta_1 + d_2\Delta\theta_2 \tag{24}$$

$$\Delta Q_1 = a_3\Delta V_1 + b_3\Delta V_2 + c_3\Delta\theta_1 + d_3\Delta\theta_2 \tag{25}$$

$$\Delta Q_2 = a_4\Delta V_1 + b_4\Delta V_2 + c_4\Delta\theta_1 + d_4\Delta\theta_2 \tag{26}$$

where Δ means a small perturbation around the equilibrium points. The coefficients a,b,c,d (with the different subscripts) are obtained by calculating the corresponding partial derivatives and they are given in Appendix A.1.
By perturbing (18) and (19) we obtain,

$$\Delta\omega_n = -k_\omega\Delta P_{avgn} \tag{27}$$

$$\Delta V_n = -k_a\Delta Q_{avgn} \tag{28}$$

Substituting (22) in (20) and (21) the average power is related to the instantaneous power by

$$\Delta P_{avgn} = \frac{1}{\tau s + 1}\Delta P_n \tag{29}$$

$$\Delta Q_{avgn} = \frac{1}{\tau s + 1}\Delta Q_n \tag{30}$$

Substituting (23) in (29) and rearranging gives,

Without losing generality, it is assumed that the two inverters in Fig. 2 have the same power ratings and hence they have the same drooping gains $k_{\omega 1} = k_{\omega 2} = k_{\omega}$. In grid-connected mode, the inverters are assumed to have different power set-points such as $P_1^* \neq P_2^*$.

Fig. 4 shows the droop control of the two inverters with different power set-points. During grid-connected mode, the frequency is fixed by the stiff grid to be ω_{grid} which equals the nominal frequency ω_o and the two inverters generate different power values $P_{grid(1)}$ and $P_{grid(2)}$. When the microgrid transfers to island mode (due to unintentional islanding) the island frequency ω_{island} deviates from its nominal value ω_o and inverters 1 and 2 generate $P_{island(1)}$ and $P_{island(2)}$, respectively. In this case, $P_{island(2)}$ is negative and hence inverter 2 is importing power. In the event of unintentional islanding and from (1), the system will reach as steady state frequency value of

$$\begin{aligned} \omega_{\text{island}} &= \omega_o^* - k_{\omega 1} P_1 + k_{\omega 1} P_1^* \\ &= \omega_o^* - k_{\omega 2} P_2 + k_{\omega 2} P_2^* \end{aligned} \tag{3}$$

Knowing that the two inverters have the same drooping gain $k_{\omega 1} = k_{\omega 2} = k_{\omega}$, (3) leads to

$$P_1 = P_1^* + P_2 - P_2^* \tag{4}$$

The total power dissipated by the load should equal the output power generated by the two inverters i.e.,

$$P_L = P_1 + P_2 \tag{5}$$

Substituting (4) and (5) in (3) the steady state island frequency is given by

$$\omega_{\text{island}} = \omega_o^* - \frac{k_{\omega}}{2}(P_L - P_1^* - P_2^*) \tag{6}$$

Equation (6) shows that the deviation from the nominal frequency depends on the local load and the power set-points of the inverters. Substituting, (5) in (4), the steady state output power of inverter 1 in island mode is given by

$$P_1 = \frac{1}{2}(P_L + P_1^* - P_2^*) \tag{7}$$

Similarly, the steady state output power of inverter 2 is given by

$$P_2 = \frac{1}{2}(P_L + P_2^* - P_1^*) \tag{8}$$

Equations (7) and (8) show that the two inverters will only share the load equally if $P_1^* = P_2^*$. They also show that if the load power is less than the difference between the two set-points, i.e.,

$$P_L < \left| P_1^* - P_2^* \right| \tag{9}$$

then one of the inverters will import power. Consider for example the case where $P_1^* = 30\text{kW}$ and $P_2^* = 10\text{kW}$, Fig. 5 shows how the inverters output power varies with respect to local load. If islanding happens when the load is less than 20kW, i.e., $P_L < P_1^* - P_2^*$, the power output P_2 will be negative hence inverter 2 will import power. This power will cause the DC link voltage (see Fig. 3) to rise and if the voltage exceeds the maximum allowed limit, the inverter will shut down. This phenomenon will reduce the reliability of the microgrid. In normal operation and after unintentional islanding is detected by the supervisory controller, a signal is sent to all inverters updating them with the status of the microgrid (grid-connected or stand-alone) so that the inverters local controller changes the set-points. However, this signal is sent via a relatively slow communication protocol (such as CAN-bus or Ethernet).

TABLE I
DC/AC CONVERTER PARAMETER VALUES

Symbol	Value	Description
L_1	1350μH	Inverter-side filter inductor
C	240μF	Filter capacitor
L_2	300μH	Grid-side filter inductor
C_{dc}	2000μF	DC link capacitor

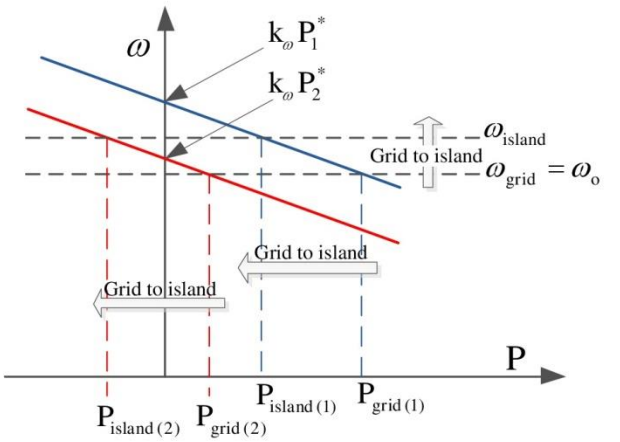

Fig. 4. Droop control of two inverters in microgrid

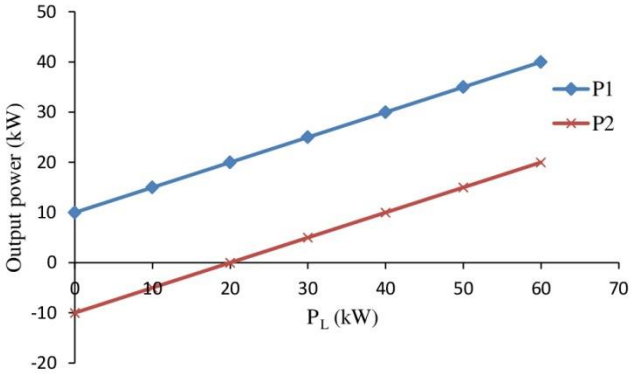

Fig. 5. Output power versus load power, $P_1^* = 30kW, P_2^* = 10kW$

Regardless of the speed of the communication protocol, there can be some delay between when the islanding happens and until islanding is detected by the supervisory controller and an update signal is sent and received. During this transitional period, the dynamic of the microgrid is important in determining the amount of energy imported by an inverter.

III. SMALL SIGNAL MODEL

In this section, a small signal model is developed to analyze the system's behavior during unintentional islanding. The model will be developed for two inverters in island mode. An inverter can be modeled by a two-terminal Thevenin equivalent circuit as shown in Fig. 6 where G(s) and $Z_o(s)$

$$s.\Delta P_{avgn} = \frac{1}{\tau}(a_n \Delta V_1 + b_n \Delta V_2 + c_n \Delta \theta_1 + d_n \Delta \theta_2) - \frac{1}{\tau}\Delta P_{avgn} \quad n = 1,2 \tag{31}$$

Substituting (25) in (30) and rearranging gives

$$s.\Delta Q_{avgn} = \frac{1}{\tau}(a_{n+2} \Delta V_1 + b_{n+2} \Delta V_2 + c_{n+2} \Delta \theta_1 + d_{n+2} \Delta \theta_2) - \frac{1}{\tau}\Delta Q_{avgn} \quad n = 1,2 \tag{32}$$

The inverter power angle is related to the frequency by,

$$s\Delta\theta_n = \Delta\omega_n, \quad n = 1,2 \tag{33}$$

Equations (23)-(33) can be combined into a homogenous state space equation such as,

$$[sX_1] = [A_1][X_1] \tag{34}$$

where $[X_1]$ contains the state variables and is given by

$$[X_1] = \begin{bmatrix} \Delta\theta_1 \\ \Delta\theta_2 \\ \Delta\omega_1 \\ \Delta\omega_2 \\ \Delta V_1 \\ \Delta V_2 \\ \Delta P_{avg1} \\ \Delta P_{avg2} \\ \Delta Q_{avg1} \\ \Delta Q_{avg2} \end{bmatrix}$$

The state variable matrix $[A_1]$ is given in Appendix A.2. Equation (34) represents a stats space model of the two inverters in island mode.

IV. DC LINK VOLTAGE CONTROLLER

A. DC link modeling

As explained earlier, the imported power may raise the DC link voltage to an unacceptable limit. In this section, the state space model developed in III will be extended to include the DC link voltage. Fig. 8(a) shows the DC link capacitor when the inverter is importing power during the transient period. The energy E absorbed by the capacitor is related to the capacitor voltage V_{DClink} by,

$$E = \int P(t)dt = \frac{1}{2} C_{dc} V_{DClink}^2 \tag{35}$$

where P is the absorbed power and C_{dc} is the DC link capacitance. In order to have a linear relationship between ΔP and V_{DClink}, the square root relation needs to be linearized. Let $x = V_{DClink}^2$ and $y(x) = \sqrt{x}$, a small change in y is given by:

$$\Delta y = \Delta x . \left.\frac{dy}{dx}\right|_{x=x_o} \tag{36}$$

where Δx is a small change in x and x_o is the equilibrium point. Given that the DC link voltage needs to be around X_o, Δy becomes

$$\Delta y = m.\Delta x \tag{37}$$

where $m = \left.\frac{dy}{dx}\right|_{x=x_o} = \left.\frac{1}{2\sqrt{x}}\right|_{x=X_o^2}$

Therefore, as shown in Fig. 8(b), the linear relationship between the DC link voltage and the power is given by

$$\Delta V_{DClinkn} = \frac{2m}{C_{dc} s} . \Delta P_n \tag{38}$$

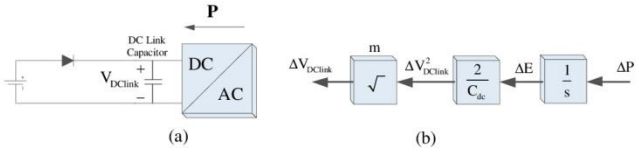

Fig. 8. DC link capacitor (a) when DC/AC inverter is importing power, (b) small signal model.

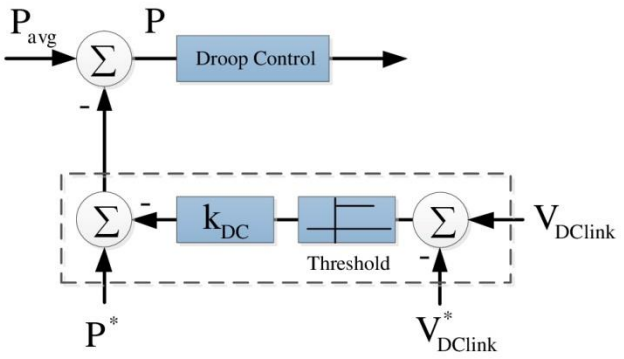

Fig. 9. Proposed Controller based on DC link voltage

Substituting (23) and (24) in (38) gives the state equation for $\Delta V_{DClink1}$ and $\Delta V_{DClink2}$. This can then be integrated with (34) to give (39) such as

$$[sX_2] = [A_2][X_2] \tag{39}$$

where,

$$[X_2] = \begin{bmatrix} X_1 \\ \Delta V_{DClink1} \\ \Delta V_{DClink2} \end{bmatrix}$$

$$[A_2] = \begin{bmatrix} A_1 & [0]_{10\times 2} \\ A_3 & [0]_{2\times 2} \end{bmatrix}$$

A_3 is given in appendix A.2

Equation (39) represents the state space equation for the complete model of the two inverters in island mode including the dynamics of the DC link voltages.

B. Design of DC link voltage controller to limit transient power

In this section, a controller is proposed to limit the amount of imported power during the transitional period so the inverters carry on working without interruption until they receive the update signal from the supervisory controller as explained earlier. The controller reduces the power set-points if the DC link voltage exceeds a certain limit. The proposed controller is illustrated in Fig. 9.

During normal operation when the power flows out of the inverter, the DC link voltage is regulated by a DC/DC

boost converter. The reference V^*_{DCLink} is the nominal DC voltage such that it only becomes effective if the DC link voltage exceeds a threshold which means the inverter is importing power. In this case, the controller will change the reference power set-point until the DC voltage difference is minimized.

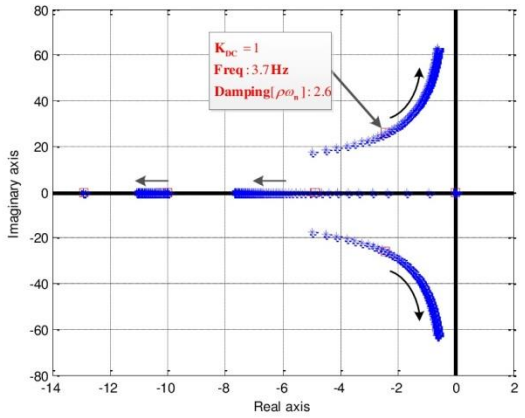

Fig. 10. Root locus of the system when $0 < k_{DC} < 10$

TABLE II
SIMULATION AND EXPERIMENTAL PARAMETERS

Symbol	Description	Value
P_1^*	Active Power set-point for inverter 1	20 W
P_2^*	Active Power set-point for inverter 2	0 W
Q_1^*	Reactive Power set-point for inverter 1	0 VAR
Q_2^*	Reactive Power set-point for inverter 2	0 VAR
P_L	Load power	0
X	Inverter output inductance (small signal and detailed simulation model)	2500 µH
k_ω	Frequency drooping gain	0.05 rad/s/W
k_a	Voltage drooping gain	0.01 V/W
V_o	Voltage set point	23 Vrms
f_o	Frequency set point	50 Hz
τ	Measurement filter time constant	0.1 sec
V^*_{DClink}	Nominal DC link voltage	40 V
$V^*_{DClink\_max}$	Maximum DC link voltage	120 V
m	Linearization factor relating V^2_{DClink} to V_{DClink}	0.0125

The controller gain k_{DC} must be selected carefully to guarantee good stability and good reduction in imported energy. In order to analyze stability, the small signal model described by (39) will be slightly modified to include the DC link voltage controller. If the proposed controller is implemented for inverter 1, then from Fig. 9 we can write,

$$P_1 = P_{avg1} - P^* + k_{DC}(V_{DClink1} - V^*_{DClink1}) \quad (40)$$

By perturbing (40) around the equilibrium points we get:

$$\Delta P_1 = \Delta P_{avg1} + k_{DC}\Delta V_{DClink1} \quad (41)$$

Substituting (41) in (27) gives,

$$\Delta\omega = -k_\omega(\Delta P_{avg1} + k_{DC}\Delta V_{DClink1}) \quad (42)$$

The state variable "s. $\Delta\omega$" becomes

$$s\Delta\omega = -k_\omega s\Delta P_{avg1} - k_\omega k_{DC} s\Delta V_{DClink1} \quad (43)$$

The state space equation of (39) can be modified to include this control loop. It can be done by modifying the 3rd row of the state matrix of A_2 according to (43). If the controller is implemented for inverter 2 then the 4th row of A_2 is also modified.

In order to analyze the effect of k_{DC} on the stability of the system, the locus of the eigenvalues of A_2 is plotted as shown in Fig. 10. The eigenvalues of the system are plotted for $0 < k_{DC} < 10$. They are in the left half plane for the selected gain range. The arrows depict the evolution of the eigenvalues when the gain value increases, which show that the system becomes faster with higher overshoot by increasing the gain since the complex poles become the dominant poles whilst the effect of the real poles decreases, which could result in the DC link voltage exhibiting greater oscillations and even instability if the gain is increased further.

Increasing the gain k_{DC} decreases the absorbed energy and so the DC voltage is minimized. However, it will increase the oscillatory components resulting in higher overshoot. Thus, by choosing k_{DC} to 1, a compromise between stability and absorbed energy is achieved.

V. SIMULATION AND EXPERIMENTAL RESULTS

The simulation results of the state space model developed earlier are compared with that of a detailed model developed using Matlab/SimPowerSystems and the results obtained from an experimental setup. The two inverters have been modeled as ideal voltage sources in Simulink as shown in Fig. 7. The simulation parameters are shown in Table II. A laboratory-scale microgrid, where the AC voltages and power ratings are scaled down by a factor of 10, was built. It consists of two DG units connected in parallel. Each DG is interfaced to the microgrid by a VSI with LCL filter. The experimental setup is shown in Fig. 11. The setup parameters are listed in Table I. A circuit breaker is used to connect each unit to the PCC. Two Semikron SKAI IGBT blocks are used. The dSPACE 1103 control unit is used to implement and realize the proposed controller scheme in real time. The dSPACE interfacing board is equipped with eight analog to digital channels (ADC) to interface the measured signals. The software code is generated by the Real-Time-Workshop under Matlab/Simulink environment. The switching and sampling frequencies used are 10KHz and 20kHz, respectively. Because the AC voltages are scaled down, a step-up transformer is used on the grid side.

Results of case 2

In this case, the two inverters are initially operating in grid connected mode. At time t = 2.1 seconds, the grid is isolated so the two inverters operate in island mode. Fig. 15 shows the responses of the average active power (instantaneous power after being filtered by the LPF) of both inverters using the detailed and the small signal model and the experimantal setup.

TABLE III
EQUILIBRIUM POINTS AND INITIAL DEVIATIONS FOR THE SMALL SIGNAL MODEL

State Variable	X_{eq}	Case 1 (starting in island mode)		Case 2 (unintentional islanding)	
		$X(0)$	$\Delta X(0)$	$X(0)$	$\Delta X(0)$
$\Delta\theta_1$	0.019 rad	0 rad	-0.019 rad	0.034 rad	0.015 rad
$\Delta\theta_2$	-0.019 rad	0 rad	0.019 rad	-0.004 rad	0.015 rad
$\Delta\omega_1$	314.66 rad/s	315.16 rad/s	0.5 rad/s	314.16 rad/s	-0.5 rad/s
$\Delta\omega_2$	314.66 rad/s	314.16 rad/s	-0.5 rad/s	314.16 rad/s	-0.5 rad/s
ΔV_1	23 Vrms	23 Vrms	0	23 Vrms	0
ΔV_2	23 Vrms	23 Vrms	0	23 Vrms	0
ΔP_{avg1}	10W	0	-10 W	20 W	10 W
ΔP_{avg2}	-10W	0	10 W	0 W	10 W
ΔQ_{avg1}	0	0	0	0	0
ΔQ_{avg2}	0	0	0	0	0

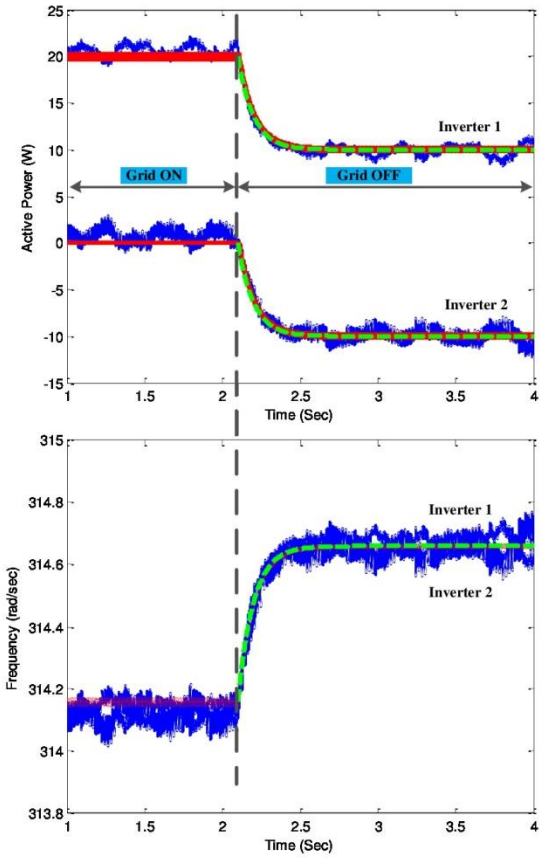

Fig. 15. Average measured active power (above) and frequency (below) of inverters 1 and 2 after grid loss- unintentional islanding (case 2)

Again, the theoretical and exmperimental results are all in full agreement. Fig. 15 also shows the frequency responses of both inverters. The behavior of the second inverter, which is importing 10W, develops high voltage across the DC link capacitor resulting in a power trip as shown in Fig. 16, which depicts the experimental DC link voltage of inverter 2 before and after islanding. When the DC link exceeds the max limit, a trip signal is generated.

C. Results of the proposed DC Controller

Fig. 17 shows the simulation and experimental results of the unintentional islanding case (case 2) with P_L=0. The first inverter was generating 20W while the second

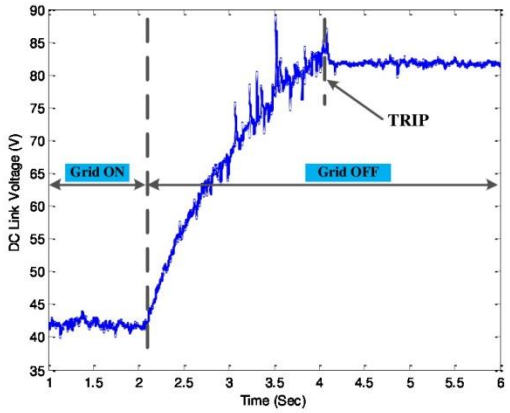

Fig. 16. DC Link voltage across the capacitor of inverter 2

inverter was generating 0W in grid-connected mode. When the islanding occurs at t=3 sec the output powers become P_1 = 10W and P_2 = -10W which agree with (7) and (8). The DC link voltage of inverter 2 starts to rise, and when it reaches 100V the DC Link controller is activated. The active powers are then reduced to zero and the DC voltage is reduced to 60V. The charging time in simulation and practical results are slightly different due the dynamics of the practical DC source (applied on the DC link capacitor), the simulation and the theoretical calculations assume ideal sources and the discussion of this is beyond the scope of this paper. The effectiveness of proposed controller is clear, as it has prevented the DC link voltage from reaching the trip limit by quickly adjusting the power demand and the inverters kept working waiting for an update signal to be received from the supervisory controller.

According to the eigenvalues of the DC link controller of Fig. 10, the predicted transient response of the DC voltage is $c(t) = e^{-2.6t}\sin(2\pi 3.7t)$. The magnified portion in Fig. 17 shows the transient oscillation of the

DC voltage. The oscillation frequencies of the detailed model and the experimental setup are 3.57Hz and 3.125Hz, respectively. The small signal model has provided good prediction of the transient response. The exponential decaying term also agrees with the eigenvalues of Fig. 10.

To test the controller at high voltages and power, Fig. 18 shows the simulation results of unintentional islanding of two inverters operating at high voltages (nominal AC voltage V_o = 230Vrms and nominal DC link voltage V^*_{Dclink} = 400V). Controllers' parameters have been scaled according to this voltage level. One inverter was injecting 10kW and the second inverter was injecting 0kW into the grid before islanding. The simulation is carried out for two different values of DC link capacitance (2200µF and 4400µF). As expected from equation (38), the DC link voltage peak deviation is inversely proportional to the capacitance value but in both cases the controller was able to prevent the DC link voltage from reaching the trip limit of 1000V. The response with the low value of DC link capacitance is quite oscillatory. Choosing a larger capacitance value will give better transient response but it will also increase cost. Choosing a smaller capacitance value can either lead to instability (if a high k_{DC} value is used) or inverter shutdown by the overvoltage protection system. It is worth mentioning here that the DC link capacitance value has traditionally been selected to satisfy certain requirements such as filtering rectifier output ripple. However, if the inverter is to be used in a microgrid, the effect of unintentional islanding on the rise of the DC link voltage needs to be taken into account when selecting the DC link capacitance. The analysis method and the controller proposed in this paper can assist the designer in choosing the required value of DC link capacitance. The small signal model can be used to firstly evaluate the rise in the DC link voltage during unintentional islanding (using the original value of DC link capacitance) and secondly to select a suitable value of k_{DC}.

If a compromise between stability and limiting DC link voltage could not be reached, and hence the proposed controller is not able to prevent the DC link voltage from reaching its trip limit with acceptable transient performance, an increase in the DC link capacitance becomes essential. The designer then needs to increase the DC link capacitance just enough to give a safe performance during unintentional islanding. The root locus graph can be used to optimize the selection of the DC link capacitance and the controller gain k_{DC}.

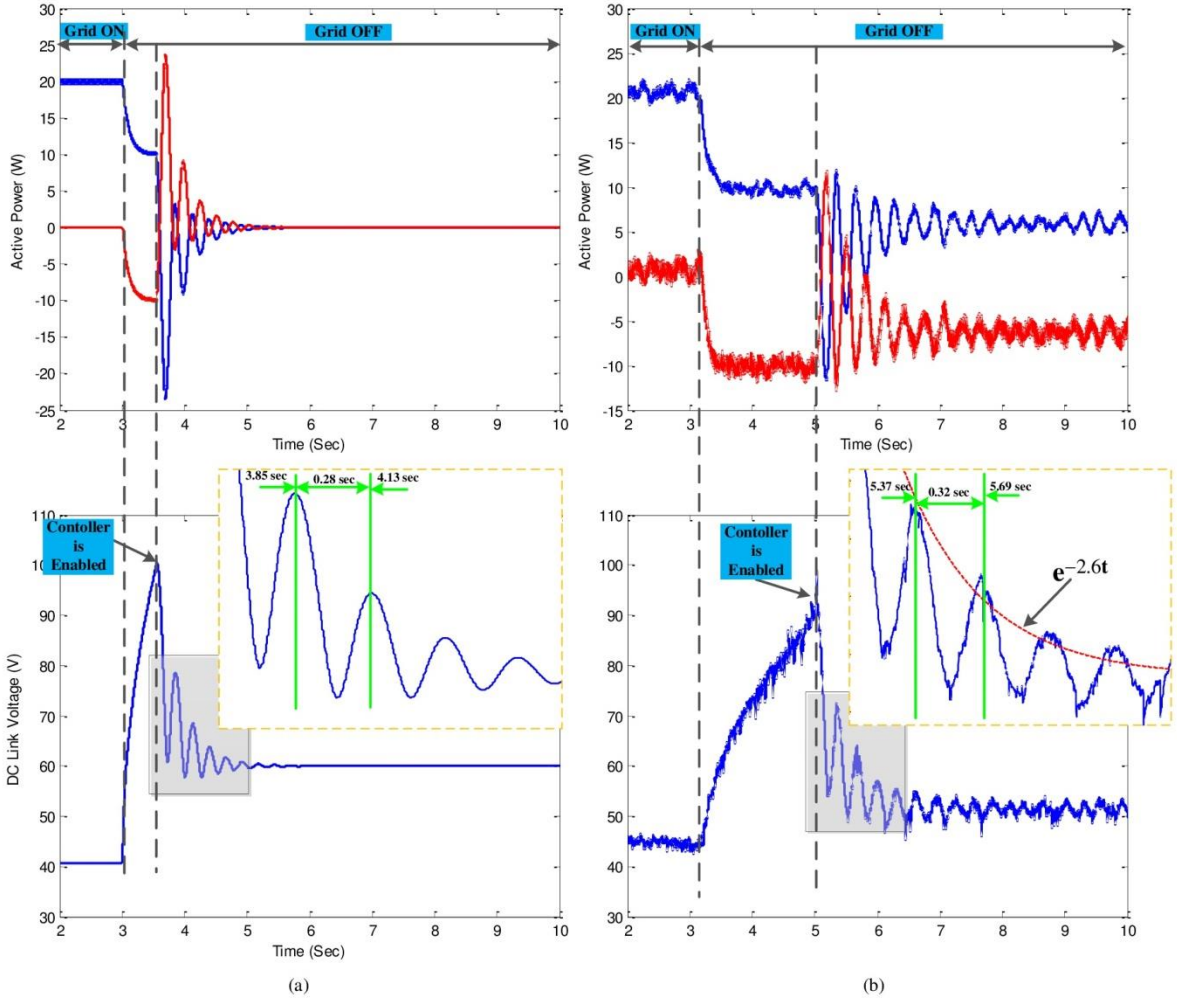

Fig. 17. Average measured active power of both inverters and DC link voltage of inverter 2 with proposed controller (k_{DC}= 1) (a) Simulink detailed model, (b) experimental setup

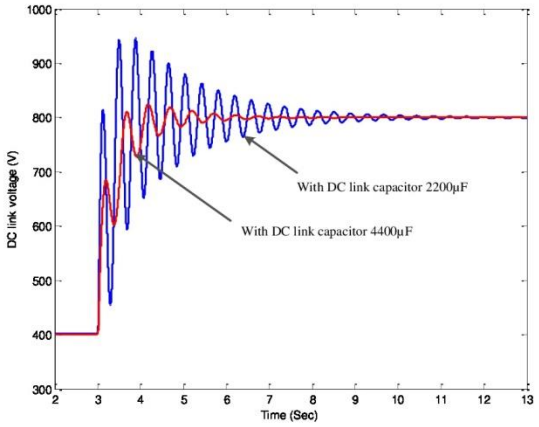

Fig. 18. DC link voltage responses in case of different values of DC link capacitor

VI. CONCLUSION

This paper has investigated the transient power between paralleled inverter during unintentional islanding and a controller to limit this circulating power has been proposed. The controller monitors the DC link voltage and if the voltage rises above a specific limit, due to power being imported, the controller adjusts the power set-point in proportion to the rise in the voltage. A small signal model of a microgrid consisting of two inverters in island mode has been developed and used to design the controller. Simulation and experimental confirmed the accuracy of the developed model and the validity of the design.

REFERENCES

[1] R. Tirumala, N. Mohan, and C. Henze, "Seamless transfer of grid-connected PWM inverters between utility-interactive and stand-alone modes," in Seventeenth Annual IEEE of Applied Power Electronics Conference and Exposition, Dallas, TX, 2002, pp. 1081-1086

[2] F. S. Pai and S. J. Huang, "A novel design of line-interactive uninterruptible power supplies without load current sensors," IEEE Transactions on Power Electronics, vol. 21, pp. 202-210, Jan 2006.

[3] H. Tao, J. L. Duarte, and M. A. M. Hendrix, "Line-interactive UPS using a fuel cell as the primary source," IEEE Transactions on Industrial Electronics, vol. 55, pp. 3012-3021, Jul 2008.

[4] M. A. P. de Azpeitia, A. Fernández, D. G. Lamar, M. Rodriguez, and M. M. Hernando, "Simplified voltage-sag filler for line-interactive uninterruptible power supplies," IEEE Transactions on Industrial Electronics, vol. 55, pp. 3005-3011, Aug 2008.

[5] H. Kim, T. Yu, and S. Choi, "Indirect current control algorithm for utility interactive inverters in distributed generation systems," IEEE Transactions on Power Electronics, vol. 23, pp. 1342-1347, May 2008.

[6] W. J. Ho, J. B. Lio, and W. S. Feng, "A line-interactive UPS structure with built-in vector-controlled charger and PFC," in International Conference on Power Electronics and Drive Systems,, 1997, pp. 127-132.

[7] Y. Okui, S. Ohta, N. Nakamura, H. Hirata, and M. Yanagisawa, "Development of line interactive type UPS using a novel control system," in The 25th International Telecommunications Energy Conference, Yokohama, Japan, 2003, pp. 796-801.

[8] M. C. Chandorkar, D. M. Divan, and R. Adapa, "Control of parallel connected inverters in standalone ac supply systems," IEEE Transactions on Industry Applications, vol. 29, pp. 136-143, Aug 1993.

[9] J. M. Guerrero, J. C. Vasquez, J. Matas, L. G. de Vicuña, and M. Castilla, "Hierarchical control of droop-controlled AC and DC microgrids—a general approach toward standardization," IEEE Transactions on Industrial Electronics, vol. 58, pp. 158-172, Jan 2011.

[10] "IEEE Standard for Interconnecting Distributed Resources with Electric Power Systems, IEEE Standard 1547, p. 16.," 2003.

[11] M. Abusara, J. M. Guerrero, and S. Sharkh, "Line Interactive UPS for Microgrids," IEEE Transactions on Industrial Electronics, pp. 1-8, Mar 2014.

[12] F. Luo, Y. Lai, C. K. Tse, and K. Loo, "A triple-droop control scheme for inverter-based microgrids," in IECON 2012-38th IEEE Annual Conference on Industrial Electronics Society, 2012, pp. 3368-3375.

[13] Y. R. Mohamed, H. H. Zeineldin, M. Salama, and R. Seethapathy, "Seamless formation and robust control of distributed generation microgrids via direct voltage control and optimized dynamic power sharing," IEEE Transactions on Power Electronics, vol. 27, pp. 1283-1294, Mar 2012.

[14] H. Tao, J. L. Duarte, and M. A. Hendrix, "Line-interactive UPS using a fuel cell as the primary source," IEEE Transactions on Industrial Electronics, vol. 55, pp. 3012-3021, Jul 2008.

Walid R. Issa received his B.Sc. and M.Sc. degrees in electrical engineering from Islamic University of Gaza (IUG), Palestine, in 2007 and 2011, respectively. He is currently

working towards his PhD at University of Exeter, UK. He worked as a teaching assistant at IUG, 2007-2010. In addition, he was a lecturer at University College of Applied Science, Palestine, 2009-2011. His main research interests include power electronics, digital control, DC/AC converters and microgrids.

Mohammad A. Abusara received his BEng degree from Birzeit University, Palestine, in 2000 and his PhD degree from the University of Southampton, UK, in 2004, both in Electrical Engineering.
He is currently a Senior Lecturer in Renewable Energy at the University of Exeter, UK. He has over ten years of industrial experience with Bowman Power Group, Southampton, UK, in the field of research and development of digital control of power electronics. During his years in industry, he designed and prototyped a number of commercial products that include grid and parallel connected inverters, microgrid, DC/DC converters for hybrid vehicles, and sensorless drives for high speed permanent magnet machines.

Suleiman M. Sharkh obtained his BEng and PhD degrees in Electrical Engineering from the University of Southampton in 1990 and 1994, respectively.
He is currently Professor of Power Electronics, Machines and Drives and Head of the Electro-Mechanical Research Group at the University of Southampton. He is also the Managing Director of HiT Systems Ltd and a Director of HiT Power Ltd. He has published over 140 papers in academic journals and conferences.
Professor Sharkh is a member of the IEEE and the IET and a Chartered Engineer. He was the 2008 winner of The Engineer Energy Innovation Award for his work on rim driven thrusters and marine turbine generators.

APENDIX A

1. State space equations coefficients

$$a_1 = \frac{\partial P_1}{\partial V_1} = \frac{+2V_{2eq}\sin(\theta_{1eq}-\theta_{2eq}) + \frac{X}{R}V_{2eq}\cos(\theta_{1eq}-\theta_{2eq})}{M}$$

$$b_1 = \frac{\partial P_1}{\partial V_2} = \frac{(\theta_{1eq}-\theta_{2eq}) + \frac{X}{R}V_{1eq}\cos(\theta_{1eq}-\theta_{2eq})}{M}$$

$$c_1 = \frac{\partial P_1}{\partial \theta_1} = \frac{2V_{1eq}V_{2eq}\cos(\theta_{1eq}-\theta_{2eq}) - \frac{X}{R}V_{1eq}V_{2eq}\sin(\theta_{1eq}-\theta_{2eq})}{M}$$

$$d_1 = \frac{\partial P_1}{\partial \theta_2} = -c_1$$

$$a_3 = \frac{\partial Q_1}{\partial V_1} = \frac{2(\frac{X^2}{R^2}+2)V_{1eq} - 2V_{2eq}\cos(\theta_{1eq}-\theta_{2eq}) + \frac{X}{R}V_{2eq}\sin(\theta_{1eq}-\theta_{2eq})}{M}$$

$$b_3 = \frac{\partial Q_1}{\partial V_2} = \frac{-2V_{1eq}\cos(\theta_{1eq}-\theta_{2eq}) + \frac{X}{R}V_{1eq}\sin(\theta_{1eq}-\theta_{2eq})}{M}$$

$$c_3 = \frac{\partial Q_1}{\partial \theta_1} = \frac{2V_{1eq}V_{2eq}\sin(\theta_{1eq}-\theta_{2eq}) + \frac{X}{R}V_{1eq}V_{2eq}\cos(\theta_{1eq}-\theta_{2eq})}{M}$$

$$d_3 = \frac{\partial Q_1}{\partial \theta_2} = -c_3$$

$$a_2 = \frac{\partial P_2}{\partial V_1} = \frac{2V_{2eq}\sin(\theta_{2eq}-\theta_{1eq}) + \frac{X}{R}V_{2eq}\cos(\theta_{2eq}-\theta_{1eq})}{M}$$

$$b_2 = \frac{\partial P_2}{\partial V_2} = \frac{2\frac{X}{R}V_{2eq} + 2V_{1eq}\sin(\theta_{2eq}-\theta_{1eq}) + \frac{X}{R}V_{1eq}\cos(\theta_{2eq}-\theta_{1eq})}{M}$$

$$c_2 = \frac{\partial P_2}{\partial \theta_1} = \frac{-2V_{1eq}V_{2eq}\cos(\theta_{2eq}-\theta_{1eq}) + \frac{X}{R}V_{1eq}V_{2eq}\sin(\theta_{2eq}-\theta_{1eq})}{M}$$

$$d_2 = \frac{\partial P_2}{\partial \theta_2} = -c_2$$

$$a_4 = \frac{\partial Q_2}{\partial V_1} = \frac{-2V_{2eq}\cos(\theta_{2eq}-\theta_{1eq}) + \frac{X}{R}V_{2eq}\sin(\theta_{2eq}-\theta_{1eq})}{M}$$

$$b_4 = \frac{\partial Q_2}{\partial V_2} = \frac{2(\frac{X^2}{R^2}+2)V_{2eq} - 2V_{1eq}\cos(\theta_{2eq}-\theta_{1eq}) + \frac{X}{R}V_{1eq}\sin(\theta_{2eq}-\theta_{1eq})}{M}$$

$$c_4 = \frac{\partial Q_2}{\partial \theta_1} = \frac{-2V_{1eq}V_{2eq}\sin(\theta_{2eq}-\theta_{1eq}) - \frac{X}{R}V_{1eq}V_{2eq}\cos(\theta_{2eq}-\theta_{1eq})}{M}$$

$$d_4 = \frac{\partial Q_2}{\partial \theta_2} = -c_4$$

where $M = 4X + \frac{X^3}{R^2}$

2. Complete state space model

$$[A_1]=\begin{bmatrix}
0 & 1 & 0 & 0 & 0 & 0 & 0 & 0 & 0 & 0\\
0 & 0 & 0 & 1 & 0 & 0 & 0 & 0 & 0 & 0\\
-\frac{k_\omega.c_1}{\tau} & -\frac{k_\omega.d_1}{\tau} & -\frac{1}{\tau} & 0 & -\frac{k_\omega.a_1}{\tau} & -\frac{k_\omega.b_1}{\tau} & 0 & 0 & 0 & 0\\
-\frac{k_\omega.c_2}{\tau} & -\frac{k_\omega.d_2}{\tau} & 0 & -\frac{1}{\tau} & -\frac{k_\omega.a_2}{\tau} & -\frac{k_\omega.b_2}{\tau} & 0 & 0 & 0 & 0\\
-\frac{k_a.c_3}{\tau} & -\frac{k_a.d_3}{\tau} & 0 & 0 & -\frac{(1+k_a.a_3)}{\tau} & -\frac{k_a.b_3}{\tau} & 0 & 0 & 0 & 0\\
-\frac{k_a.c_4}{\tau} & -\frac{k_a.d_4}{\tau} & 0 & 0 & -\frac{k_a.a_4}{\tau} & -\frac{(1+k_a.b_4)}{\tau} & 0 & 0 & 0 & 0\\
\frac{c_1}{\tau} & \frac{d_1}{\tau} & 0 & 0 & \frac{a_1}{\tau} & \frac{b_1}{\tau} & \frac{-1}{\tau} & 0 & 0 & 0\\
\frac{c_2}{\tau} & \frac{d_2}{\tau} & 0 & 0 & \frac{a_2}{\tau} & \frac{b_2}{\tau} & 0 & \frac{-1}{\tau} & 0 & 0\\
\frac{c_3}{\tau} & \frac{d_3}{\tau} & 0 & 0 & \frac{a_3}{\tau} & \frac{b_3}{\tau} & 0 & 0 & \frac{-1}{\tau} & 0\\
\frac{c_4}{\tau} & \frac{d_4}{\tau} & 0 & 0 & \frac{a_4}{\tau} & \frac{b_4}{\tau} & 0 & 0 & 0 & \frac{-1}{\tau}
\end{bmatrix}$$

$$[A_3]=\begin{bmatrix}
\frac{2mc_1}{C_{dc}} & \frac{2md_1}{C_{dc}} & 0 & 0 & \frac{2ma_1}{C_{dc}} & \frac{2mb_1}{C_{dc}} & 0 & 0 & 0 & 0 & 0 & 0 & 0 & 0\\
\frac{2mc_2}{C_{dc}} & \frac{2md_2}{C_{dc}} & 0 & 0 & \frac{2ma_2}{C_{dc}} & \frac{2mb_2}{C_{dc}} & 0 & 0 & 0 & 0 & 0 & 0 & 0 & 0
\end{bmatrix}$$

Impedance Interaction between Islanded Parallel Voltage Source Inverters and the Distribution Network

W. R. Issa*, M. A. Abusara*, and S. M. Sharkh†

*Exeter University, UK (wrmi201@exeter.ac.uk), †Southampton University, UK

Keywords: Island mode, Resonance, Output impedance

Abstract

In an islanded microgrid consisting of parallel-connected inverters, the interaction between an inverter's output impedance (dominated by the inverter's filter and voltage controller) and the impedance of the distribution network (dominated by the other paralleled inverters' output impedances and the interconnecting power cables) might lead to instability. This paper studies this phenomenon using root locus analysis. A controller based on the second derivative of the output capacitor voltage is proposed to enhance the stability of the system. Matlab simulation results are presented to confirm the validity of the theoretical analysis and the robustness of the proposed controller.

1. Introduction

Microgrids are defined as systems that have at least one distributed generation (DG) unit and associated loads, and can work in grid-connected mode as well as in island mode [1]. Due to its controllability, microgrids will become building block of future smart grids. This technology can offer improved service reliability, better economics and reduced dependency on the local utility.

When controlling a microgrid, it is important to ensure the stability of each unit as well as the microgrid as a whole under different loads and system conditions. In many practical scenarios, the DGs are located far away from each other and therefore they are connected to the network via cables with non-negligible impedance. This could cause the voltage controllers of DGs working in parallel to become unstable.

Power sharing between parallel-connected DGs can be achieved using the well-known droop control [2]-[7]. Much research has also been done to enhance droop control to improve the accuracy of the power sharing between DGs [8]-[10]. The concept of the virtual impedance has been widely used to overcome the problem of power coupling caused by high R/X ratio in low voltage distribution networks [11, 12]. It increases the inductive reactance of the inverter's output impedance without using additional physical inductors that would increase size and cost. Each inverter is normally controlled by a core controller that regulates the inverter's output voltage, and an outer droop controller that sets the amplitude and frequency references for the inner core controller. The core controller has much higher bandwidth and hence faster response than that of the outer droop controller and therefore the dynamic behavior of the inner core controller is normally neglected in the design and analysis of the droop controller. Consequently, the interaction between the core voltage controller and the distribution network (consisting of cables, loads and other inverters) is often discarded. However, in practice, the DGs voltage controller can become unstable due to the interaction between the output impedance of each inverter and other inverters and cable impedances that can create parallel and/or series resonance. If the resonance frequency is within the bandwidth of the voltage controller an instability could occur. Thus, designing the inverter controller as a single isolated unit does not guarantee stability in all conditions.

Different types of controller including PI, repetitive, resonant, deadbeat and many other controllers have been used in grid-connected inverters. They usually utilize dual loop control to dampen output filter resonance [13]-[16]. However, the interaction between the inverter and the network is rarely considered or addressed when designing these controllers. In [17], the interaction between uninterruptible power supplies (UPS) was investigated. The study recommended reducing the voltage controller bandwidth by manipulating the voltage and current controllers' gain to keep the system stable. In [18], the controller bandwidth was reduced by using a feedforward loop. Ref [18] also concluded that a resistive virtual impedance has no effect on the system stability. However, the effect of an inductive virtual impedance was not addressed.

In this paper, the effect of the inductive virtual impedance as well as cables' length on the stability of parallel-connected inverters is studied. A controller based on the second derivative of the output capacitor voltage is proposed to enhance the stability of the system. The proposed controller ensures stability over a range of cable impedance and virtual impedance values.

2. System modelling

Fig. 1 shows an islanded microgrid consisting of two inverters and their LC filters, cables and load. The parameters of the system considered in this paper are listed in Table 1.

Fig. 2 shows a block diagram of one inverter and its basic controller. It consists of an outer feedback loop of the capacitor voltage V_o and an inner feedback loop of the capacitor current I_c with the latter employed to provide damping to the filter resonance. In addition to the dual feedback loops of I_c and V_o, a feedforward loop of the reference voltage is also implemented to minimise the steady state error. Furthermore, a virtual impedance loop is used to make the output impedance of the inverter more inductive and hence increase the decoupling between active and reactive power. Thus, the active power is predominantly dependent on the power angle and the reactive power is predominantly dependent on the output voltage.

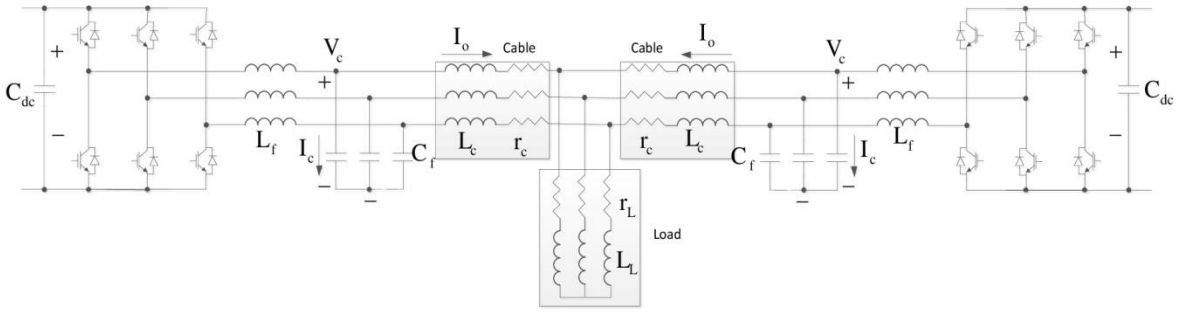

Fig. 1. Islanded Microgrid Structure

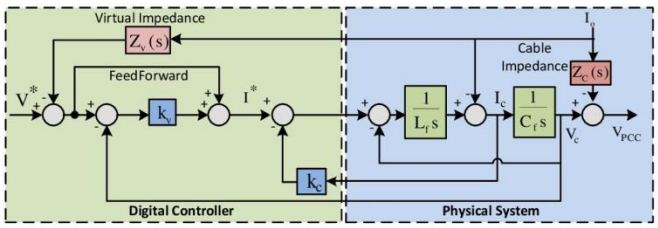

Fig. 2. The basic double-loop voltage controller of an inverter

Symbol	Description	Value
L_f	Inverter-side filter inductor	800µH
C_f	Filter capacitor	60µF
k_v	Voltage controller loop gain	2
k_c	Current controller loop gain	2.2
r_c	Cable resistance	$0.5\times10^{-3}\Omega/\mathrm{m}$
L_c	Cable inductance	$1\mu\mathrm{H}/\mathrm{m}$
L_v	Nominal virtual inductance	650µH
τ	Time constant (virtual impedance)	1/1500

Table 1. System Parameter Values

It can be shown from Fig. 2 that the output voltage is given by

$$V_o(s) = G(s)V^*(s) - Z_o(s)I_o(s) \quad (1)$$

where G(s) is the closed loop transfer function that relates V_o to V^* and Z(s) is the closed loop output impedance and they are given by

$$G(s) = \frac{k_v + 1}{L_f C_f s^2 + k_c C_f s + k_v + 1} \quad (2)$$

$$Z_o(s) = \frac{L_f s}{L_f C_f s^2 + k_c C_f s + 1 + k_v} + G(s)Z_v(s) \quad (3)$$

The virtual impedance transfer function $Z_v(s)$ in (3) is given by

$$Z_v(s) = \frac{s}{\tau s + 1} L_v \quad (4)$$

where L_v is the inductance of the virtual impedance and τ is the time constant of the high pass filter used to approximate the derivative in the transfer function of the ideal virtual inductance ($Z_v = sL_v$). Fig. 3 shows the Thévenin equivalent circuit of a simple single inverter model represented by (1). Fig. 4 shows the frequency response of the output impedance transfer function $Z_o(s)$ with L_v equals to zero and 650µH. As can be seen, the output impedance has a predominant inductive behavior in the region below the natural frequency that is important for proper droop control operation, especially, around the fundamental frequency. There is a resonance at the natural frequency but it has been damped thanks to the inner current loop.

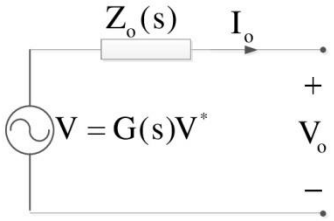

Fig. 3. Simple inverter model (Thévenin equivalent circuit)

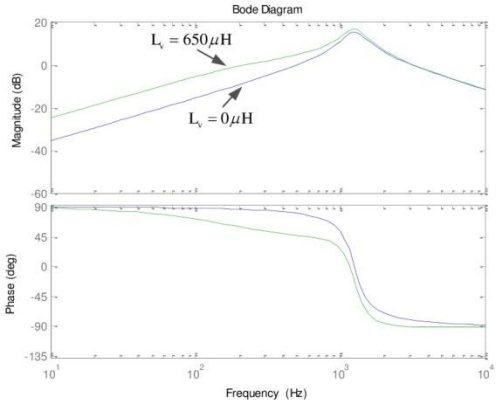

Fig. 4. Bode plot of output impedance with/without virtual impedance

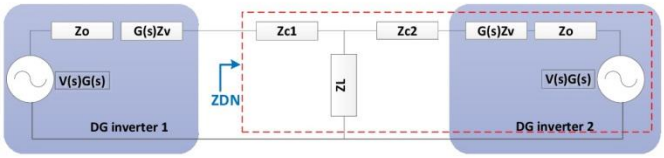

Fig. 5. General microgrid model

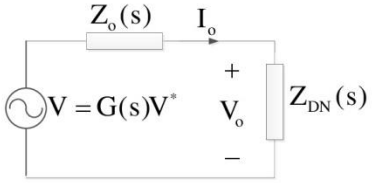

Fig. 6. Simplified Model

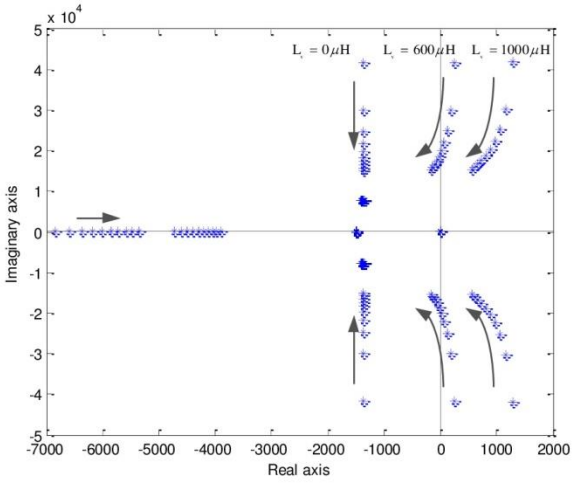

Fig. 7. Root locus when cable length varies from 10m to 100m, for value of L_v of 0, 600 and 1000µH

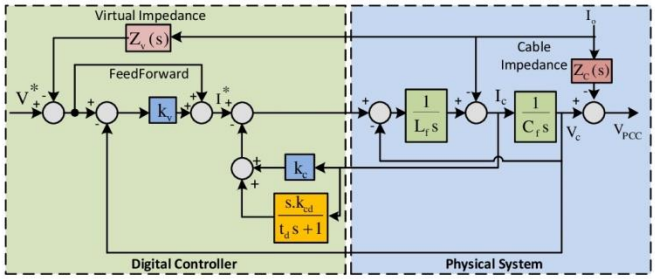

Fig. 8. The proposed voltage controller

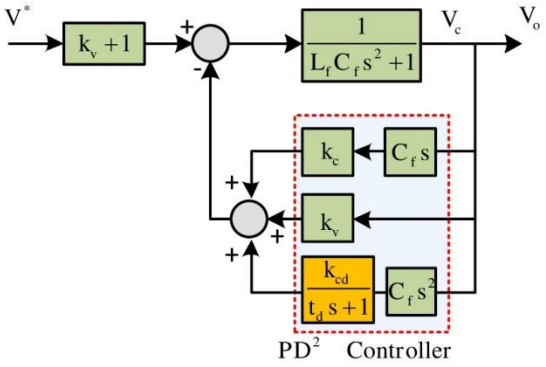

Fig. 9. The simplified proposed voltage controller loop

A circuit model for a microgrid consisting of two inverters connected through cables and supplying a common load is shown in
Fig. 5 where Z_{c1} and Z_{c2} are the impedances of the connecting cables. Using the superposition principle, i.e., by setting the voltage of the second inverter to zero, i.e., $G(s)V^*(s)=0$, the microgrid from the point of view of the first inverter can be modelled as shown in Fig. 6 where $Z_{DN}(s)$ represents the equivalent impedance of the load, cables and the output impedance of the second inverter. The load impedance in this paper will be assumed very high (i.e., open circuit). This represents the worst-case scenario for resistive loads, as the load resistivity will increase the system damping. Therefore, the equivalent impedance $Z_{DN}(s)$ is given by

$$Z_{DN}(s) = Z_{c1} + Z_{c2} + Z_o \tag{5}$$

From Fig. 6, the output voltage can be written as

$$V_o(s) = \frac{G(s)V_c^*(s) \times Z_{DN}(s)}{Z_o(s) + Z_{DN}(s)} \tag{6}$$

Equation (6) represents the closed loop transfer function relating the output voltage V_o to the reference voltage V^* taking into account the effect of the connecting cables and the impedance of the other inverters.

3. Stability Analysis

From (6), the root locus of the characteristics equation (7), can be used to analyze the system stability.

$$Z_o(s) + Z_{DN}(s) = 0 \tag{7}$$

The interaction between an inverter with the network containing cables and other inverters can be addressed using equation (7) in terms of the value of the virtual impedance and the length of cables.

The effect of the virtual impedance on stability is illustrated with the aids of the root locus as shown in Fig. 7. In this figure, the effect of cables length, change from 10m to 100m, on the closed loop poles of the system is shown for three virtual impedance values of 0, 600 and 1000µH; the arrows show the direction of increase of the cable length. As depicted, high values of virtual inductance (above 600µH) reduce the stability of the system. This can be explained to be due to the increase of the high frequency gain. The cable impedance also has a significant effect on the system. A combination of a short cable and a high virtual impedance value can destabilize the system. Increasing the length of the cable and hence its resistance improves system stability as expected.

4. Proposed controller

To improve the stability of the system we propose employing a feedback of the voltage second derivative to present more damping for the complex poles and shift them farther to the left. The new proposed controller is shown in Fig. 8.

As known, the capacitor current is given by the derivative of the voltage across it,

$$I_c = C_f \frac{dV_c}{dt} \tag{8}$$

The second derivative of voltage can be therefore used to obtain the derivative of the capacitor current as:

$$\frac{dI_c}{dt} = C_f \frac{d^2V_c}{dt^2} \quad (9)$$

Hence, the extra damping term could be realized by the first derivative of capacitor current, which presents a PD^2 controller instead of PD controller as shown in its simplified version in Fig. 9.

The PD^2 controller measures the change of rate of current change of rate that could reduce the disturbance effects on the system if proper gain is used to reject these disturbances.

The first derivative already can be measured directly by sensing the capacitor current. However, the second derivative needs to be calculated. Differentiation of the high-frequency capacitor current may cause serious noise multiplication problems that could lead to instability. Therefore, a low pass filter is added after the derivative term to minimize the effect of the high frequency on system stability. The full derivative followed by low pass filter is stated as:

$$s.I_c.\frac{1}{\tau_d s+1} \quad (10)$$

where τ_d is the time constant of the filter.

The new version of the voltage closed loop transfer function is calculated as stated in (11), where k_{cd} is the derivative gain of the capacitor current.

The new output impedance is obtained from Fig. 8, with considering the virtual and cable impedances, as in equation (12).

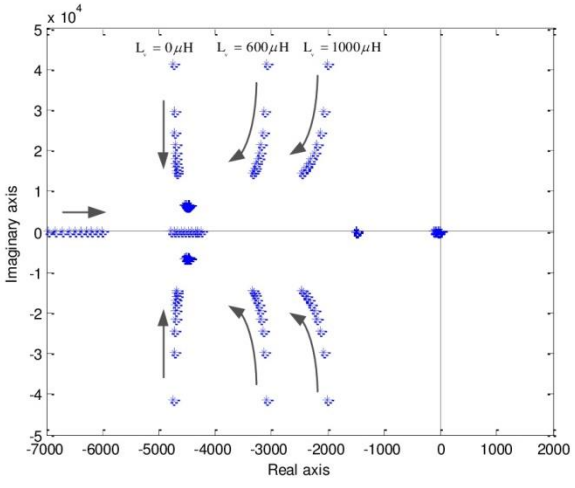

Fig. 10. Root locus with the proposed controller as the virtual inductance and cables length varies from 10-100 m

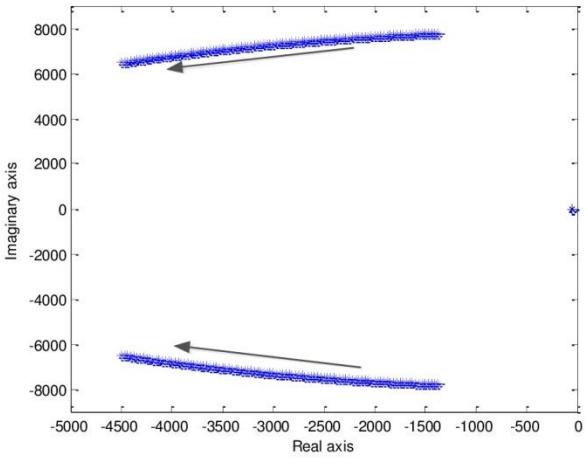

Fig. 11. Root locus of the voltage controller when k_{cd} varies from 0 to 0.1

Fig. 10 illustrates the effect of the proposed controller on stability. The root locus now shows that the system is stable for the range of virtual inductance values and cable lengths.

Fig. 11 illustrates the locus of $G_p(s)$ when k_{cd} varies from 0 to 0.1 where $\tau_d = 0.02$. As shown, it shifts the oscillated components far away from the imaginary axis thus increasing stability.

5. Simulation results

Matlab model was built, as shown in Fig. 5 , including two single-phase inverters modeled by two-leg IGBT bridge and voltage controller with capacitor voltage and current as feedback signals. They are connected via cables lengths 10m and 20m respectively. The model parameters are listed in Table 1. The voltages of the inverters are shown in Fig. 12 with and without the proposed controller. As shown, the system without the proposed controller is unstable as expected from the previous analysis while the stability is achieved with the proposed controller.

More results are obtained with the proposed controller shown in Fig. 13. The cable length of the second inverter has changed from 20m to 30m at t= 0.05 sec concurrently with an increment step of the virtual inductance from 650μH to 1000μH. The results confirm the stability and illustrate the robustness of the proposed controller against different network and controller conditions.

$$G_p(s) = \frac{(k_v+1)\tau_d s + k_v + 1}{L_f.C_f.\tau_d s^3 + (L_f.C_f + C_f.k_c.\tau_d + C_f.k_{cd})s^2 + (k_c.C_f + \tau_d(k_v+1))s + k_v + 1} \quad (11)$$

$$Z_{op}(s) = \frac{L_f\tau_d s^2 + L_f s}{L_f.C_f.\tau_d s^3 + (L_f.C_f + C_f.k_c.\tau_d + C_f.k_{cd})s^2 + (k_c.C_f + \tau_d(k_v+1))s + k_v + 1} + G_p(s)Z_v(s) + Z_C(s) \quad (12)$$

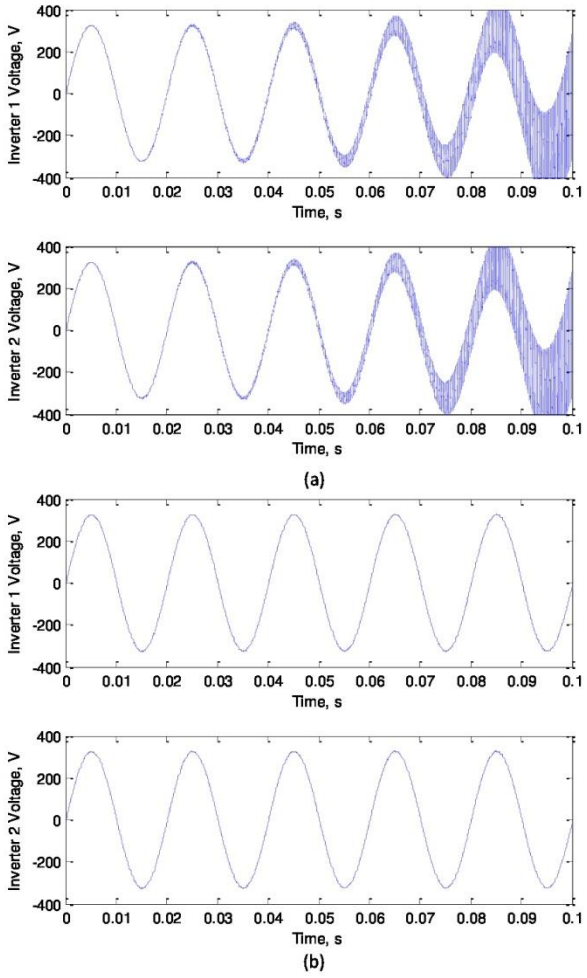

Fig. 12. Output voltages of the two inverters without (a) and with (b) the proposed control loop

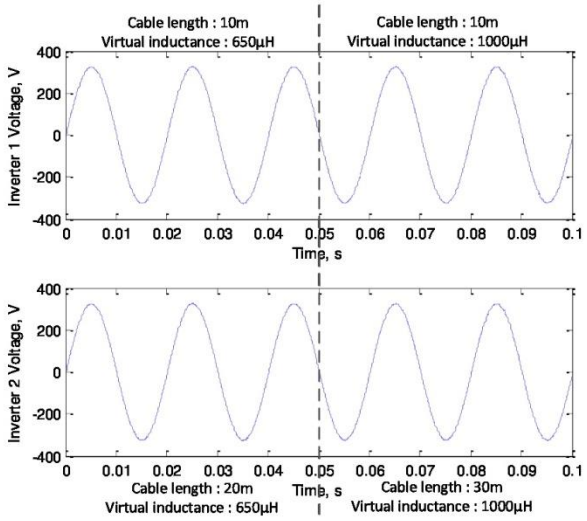

Fig. 13. Output voltages of the two inverters with the proposed control loop when the cable length and virtual inductance vary

6. Conclusion

This paper studies the interaction between the output impedance of microgrid inverters and the network impedance including interconnecting cables and the impedance of other parallel inverters. This interaction can destabilize the whole system. A novel controller that uses a feedback loop of the second derivative of the inverter's output voltage has been proposed to enhance stability. Matlab simulation results have verified the theoretical analysis and the validity of the proposed controller.

References

[1] B. Kroposki, R. Lasseter, T. Ise, S. Morozumi, S. Papatlianassiou, and N. Hatziargyriou, "Making microgrids work," IEEE Power and Energy Magazine, vol. 6, pp. 40-53, 2008.

[2] B. B. K. Brabandere, J. Keybus, A. Woyte, J. Driesen, and R.Belmans, "A voltage and frequency droop control method for parallel inverters," IEEE Trans. Ind. Eelectron., vol. 22, pp. 1107-1115, 2007.

[3] J. C. Vasquez, J. M. Guerrero, A. Luna, P. Rodríguez, and R. Teodorescu, "Adaptive droop control applied to voltage-source inverters operating in grid-connected and islanded modes," IEEE Transactions on Industrial Electronics, vol. 56, pp. 4088-4096, 2009.

[4] H. J. Avelar, W. A. Parreira, J. B. Vieira, L. C. G. de Freitas, and E. A. A. Coelho, "A State Equation Model of a Single-Phase Grid-Connected Inverter Using a Droop Control Scheme With Extra Phase Shift Control Action," IEEE Transactions on Industrial Electronics, vol. 59, pp. 1527-1537, 2012.

[5] F. Luo, Y. Lai, C. K. Tse, and K. Loo, "A triple-droop control scheme for inverter-based microgrids," in IECON 2012-38th IEEE Annual Conference on Industrial Electronics Society, 2012, pp. 3368-3375.

[6] M. Abusara and S. Sharkh, "Control of line interactive UPS systems in a Microgrid," in IEEE International Symposium on Industrial Electronics (ISIE), 2011, pp. 1433-1440.

[7] J. M. Guerrero, J. C. Vasquez, J. Matas, M. Castilla, and L. G. de Vicuna, "Control strategy for flexible microgrid based on parallel line-interactive UPS systems," IEEE Transactions on Industrial Electronics, vol. 56, pp. 726-736, 2009.

[8] J. M. Guerrero, L. G. De Vicuna, J. Matas, M. Castilla, and J. Miret, "A wireless controller to enhance dynamic performance of parallel inverters in distributed generation systems," IEEE Transactions on Power Electronics, vol. 19, pp. 1205-1213, 2004.

[9] H. Z. Xiaotian Zhang, Josep M. Guerrero, Xikui Ma, "Reactive Power Compensation for Parallel

Inverters without Control Interconnections in Microgrid," IECON 2008. 34th Annual Conference of IEEE Industrial Electronics, 2008.

[10] M. C. Wei Yao, José Matas, Josep M. Guerrero, Zhao-Ming Qian, "Design and Analysis of the Droop Control Method for Parallel Inverters Considering the Impact of the Complex Impedance on the Power Sharing," IEEE Transactions on Industrial Electronics, vol. 58, 2011.

[11] M. Abusara, J. M. Guerrero, and S. Sharkh, "Line Interactive UPS for Microgrids," IEEE Transactions on Industrial Electronics, pp. 1-8, 2013.

[12] J. Kim, J. M. Guerrero, P. Rodriguez, R. Teodorescu, and K. Nam, "Mode Adaptive Droop Control With Virtual Output Impedances for an Inverter-Based Flexible AC Microgrid," IEEE Transactions on Power Electronics, vol. 26, pp. 689-701, 2011.

[13] R. Ortega, E. Figueres, G. Garcerá, C. L. Trujillo, and D. Velasco, "Control techniques for reduction of the total harmonic distortion in voltage applied to a single-phase inverter with nonlinear loads: Review," Renewable and Sustainable Energy Reviews, vol. 16, pp. 1754-1761, 2012.

[14] M. A. Abusara, M. Jamil, and S. M. Sharkh, "Repetitive current control of an interleaved grid-connected inverter," in IEEE International Symposium on Power Electronics for Distributed Generation Systems (PEDG), 2012 3rd, 2012, pp. 558-563.

[15] G. Escobar, P. Mattavelli, A. M. Stankovic, A. A. Valdez, and J. Leyva-Ramos, "An adaptive control for UPS to compensate unbalance and harmonic distortion using a combined capacitor/load current sensing," IEEE Transactions on Industrial Electronics vol. 54, pp. 839-847, 2007.

[16] P. Mattavelli, "An improved deadbeat control for UPS using disturbance observers," IEEE Transactions on Industrial Electronics, vol. 52, pp. 206-212, 2005.

[17] L. Corradini, P. Mattavelli, M. Corradin, and F. Polo, "Analysis of Parallel Operation of Uninterruptible Power Supplies Loaded through Long Wiring Cables," in Twenty-Fourth Annual IEEE Applied Power Electronics Conference and Exposition, 2009, pp. 1276-1282.

[18] X. Wang, F. Blaabjerg, Z. Chen, and W. Wu, "Resonance analysis in parallel voltage-controlled Distributed Generation inverters," in Twenty-Eighth Annual IEEE Applied Power Electronics Conference and Exposition (APEC), 2013, pp. 2977-2983.

BIBLIOGRAPHY

[1] P. M. Carvalho, P. F. Correia, and L. Ferreira, "Distributed reactive power generation control for voltage rise mitigation in distribution networks," *IEEE Transactions on Power Systems,* vol. 23, pp. 766-772, 2008.

[2] N. D. Hatziargyriou and A. S. Meliopoulos, "Distributed energy sources: technical challenges," in *Power Engineering Society Winter Meeting, 2002. IEEE*, 2002, pp. 1017-1022.

[3] B. Hussain, Sharkh, S.M. and Hussain, S, "Impact studies of distributed generation on power quality and protection setup of an existing distribution network," presented at the 20th International Symposium on Power Electronics, Electrical Drives, Automation and Motion (SPEEDAM 2010), Pisa, 2010.

[4] C. Masters, "Voltage rise: the big issue when connecting embedded generation to long 11 kV overhead lines," *Power Engineering Journal,* vol. 16, pp. 5-12, 2002.

[5] M. Abusara and S. Sharkh, "Control of line interactive UPS systems in a Microgrid," in *IEEE International Symposium on Industrial Electronics (ISIE)*, 2011, pp. 1433-1440.

[6] J. Liang, T. Green, G. Weiss, and Q. C. Zhong, "Hybrid control of multiple inverters in an island-mode distribution system," in *IEEE 34th Annual Power Electronics Specialist Conference, 2003. PESC '03.*, 2003, pp. 61-66 vol. 1.

[7] C. L. Chen, Y. Wang, J. S. Lai, Y. S. Lee, and D. Martin, "Design of parallel inverters for smooth mode transfer microgrid applications," *IEEE Transactions on Power Electronics,* vol. 25, pp. 6-15, 2010.

[8] M. Abusara, J. M. Guerrero, and S. Sharkh, "Line Interactive UPS for Microgrids," *IEEE Transactions on Industrial Electronics,* pp. 1-8, Mar 2013.

[9] R. H. Lasseter, "MicroGrids," in *IEEE Power Engineering Society Winter Meeting, 2002*, 2002, pp. 305-308 vol. 1.

[10] F. Katiraei and M. Iravani, "Power management strategies for a microgrid with multiple distributed generation units," *IEEE Transactions on Power Systems,* vol. 21, pp. 1821-1831, 2006.

[11] J. A. P. Lopes, C. Moreira, and A. Madureira, "Defining control strategies for microgrids islanded operation," *IEEE Transactions on Power Systems,* vol. 21, pp. 916-924, 2006.

[12] A. Mohd, E. Ortjohann, D. Morton, and O. Omari, "Review of control techniques for inverters parallel operation," *Electric Power Systems Research,* vol. 80, pp. 1477-1487, 2010.

[13] M. A. Pedrasa and T. Spooner, "A survey of techniques used to control microgrid generation and storage during island operation," in *The Australian Universities Power Engineering Conf*, 2006, pp. 10-13.

[14] M. N. Marwali, J. W. Jung, and A. Keyhani, "Control of distributed generation systems-Part II: Load sharing control," *IEEE Transactions on Power Electronics,* vol. 19, pp. 1551-1561, 2004.

[15] J. C. Vasquez, R. Mastromauro, J. M. Guerrero, and M. Liserre, "Voltage support provided by a droop-controlled multifunctional inverter," *IEEE Transactions on Industrial Electronics,* vol. 56, pp. 4510-4519, 2009.

[16] J. M. Guerrero, L. G. De Vicuna, J. Matas, M. Castilla, and J. Miret, "A wireless controller to enhance dynamic performance of parallel inverters in distributed generation systems," *IEEE Transactions on Power Electronics,* vol. 19, pp. 1205-1213, 2004.

[17] J. M. Guerrero, J. C. Vasquez, J. Matas, L. G. de Vicuña, and M. Castilla, "Hierarchical control of droop-controlled AC and DC microgrids—a general approach toward standardization," *IEEE Transactions on Industrial Electronics,* vol. 58, pp. 158-172, Jan 2011.

[18] L. Xinchun, F. Feng, D. Shanxu, K. Yong, and C. Jian, "The droop characteristic decoupling control of parallel connected UPS with no control interconnection," in *IEEE International Electric Machines and Drives Conference, 2003. IEMDC'03*, 2003, pp. 1777-1780 vol. 3.

[19] A. E. a. N. Soultanis, "Droop control in LV-grids," in *2005 International Conference on Future Power Systems*, 2005, pp. 6-11.

[20] J. C. V. Josep M. Guerrero, José Matas, Jorge L. Sosa Luis, García de Vicuña, "Parallel Operation of Uninterruptible Power Supply Systems in MicroGrids," presented at the European Conference on Power Electronics and Applications, 2007, 2006.

[21] G. Yajuan, W. Weiyang, G. Xiaoqiang, and G. Herong, "An improved droop controller for grid-connected voltage source inverter in microgrid," in *2nd IEEE International Symposium on Power Electronics for*

Distributed Generation Systems (PEDG), 2010, Hefei, China, 2010, pp. 823-828.

[22] B. C. Ritwik Majumder, Arindam Ghosh,Rajat Majumder, Gerard Ledwich and Firuz Zare, "Improvement of Stability and Load Sharing in an Autonomous Microgrid Using Supplementary Droop Control Loop," *IEEE TRANSACTIONS ON POWER SYSTEMS,* vol. 25, May 2010.

[23] R. Mastromauro, M. Liserre, A. Dell'Aquila, J. Guerrero, and J. Vasquez, "Droop control of a multifunctional pv inverter," in *IEEE International Symposium on Industrial Electronics, 2008. ISIE 2008*, Cambridge, 2008, pp. 2396-2400.

[24] H. J. Avelar, W. A. Parreira, J. B. Vieira, L. C. G. de Freitas, and E. A. A. Coelho, "A State Equation Model of a Single-Phase Grid-Connected Inverter Using a Droop Control Scheme With Extra Phase Shift Control Action," *IEEE Transactions on Industrial Electronics,* vol. 59, pp. 1527-1537, 2012.

[25] E. A. A. Coelho, P. C. Cortizo, and P. F. D. Garcia, "Small-signal stability for parallel-connected inverters in stand-alone AC supply systems," *IEEE Transactions on Industry Applications,* vol. 38, pp. 533-542, 2002.

[26] L. Xinchun, F. Feng, D. Shanxu, K. Yong, and C. Jian, "Modeling and stability analysis for two paralleled UPS with no control interconnection," in *IEEE International Electric Machines and Drives Conference, 2003. IEMDC'03*, 2003, pp. 1772-1776.

[27] J. M. Josep M. Guerrero, Luis García de Vicuña, Miguel Castilla, and Jaume Miret, "Wireless-Control Strategy for Parallel Operation of

Distributed-Generation Inverters," *IEEE TRANSACTIONS ON INDUSTRIAL ELECTRONICS,* vol. 53, OCTOBER 2006.

[28] A. Tavakoli, M. Sanjari, M. Kohansal, and G. Gharehpetian, "An innovative power calculation method to improve power sharing in VSI based Micro Grid," in *2nd Iranian Conference on Smart Grids (ICSG), 2012* 2012, pp. 1-5.

[29] M.-z. Gao, M. Chen, C. Jin, J. M. Guerrero, and Z.-m. Qian, "Analysis, design, and experimental evaluation of power calculation in digital droop-controlled parallel microgrid inverters," *Journal of Zhejiang University SCIENCE C,* vol. 14, pp. 50-64, 2013.

[30] Y. W. Li and C. N. Kao, "An accurate power control strategy for power-electronics-interfaced distributed generation units operating in a low-voltage multibus microgrid," *IEEE Transactions on Power Electronics,* vol. 24, pp. 2977-2988, 2009.

[31] S.-J. A. Hyun-Koo Kang, and Seung-Il Moon, "A New Method to Determine the Droop of Inverter-based DGs," presented at the IEEE Power & Energy Society General Meeting, 2009. PES '09, 2009.

[32] M. C. Wei Yao, Mingzhi Gao, Zhaoming Qian, "A Wireless Load Sharing Controller to Improve the Performance of Parallel-Connected Inverters," in *Twenty-Third Annual IEEE in Applied Power Electronics Conference and Exposition*, TX, 2008, pp. 1628 - 1631.

[33] A. Haddadi, A. Shojaei, and B. Boulet, "Enabling high droop gain for improvement of reactive power sharing accuracy in an electronically-interfaced autonomous microgrid," in *Energy Conversion Congress and Exposition (ECCE), 2011*, 2011, pp. 673-679.

[34] B. B. K. Brabandere, J. Keybus, A. Woyte, J. Driesen, and R.Belmans, "A voltage and frequency droop control method for parallel inverters," *IEEE Trans. Ind. Eelectron.,* vol. 22, pp. 1107-1115, 2007.

[35] J. C. Vásquez, J. M. Guerrero, E. Gregorio, P. Rodríguez, R. Teodorescu, and F. Blaabjerg, "Adaptive droop control applied to distributed generation inverters connected to the grid," in *IEEE International Symposium on Industrial Electronics, 2008. ISIE 2008*, 2008, pp. 2420-2425.

[36] J. M. G. JUAN C. VASQUEZ, JAUME MIRET, MIGUEL CASTILLA, and LUIS GARCI´A DE VICUN˜ A. (2010, DECEMBER) Hierarchical control of intelligent microgrids. *IEEE INDUSTRIAL ELECTRONICS MAGAZINE*.

[37] A. G. Ritwik Majumder, Gerard Ledwich, Firuz Zare, "Power System Stability and Load Sharing in Distributed Generation," presented at the Joint International Conference on Power System Technology, 2008.

[38] R. Majumder, A. Ghosh, G. Ledwich, and F. Zare, "Operation and control of hybrid microgrid with angle droop controller," in *IEEE Region 10 Conference TENCON 2010 - 2010* 2010, pp. 509-515.

[39] P. W. L. C.K. Sao, "Autonomous load sharing of voltage source converters," *IEEE Trans. on Power Delivery,* vol. 20, pp. 1009-1016, Feb 2005.

[40] J. Kim, J. M. Guerrero, P. Rodriguez, R. Teodorescu, and K. Nam, "Mode Adaptive Droop Control With Virtual Output Impedances for an Inverter-Based Flexible AC Microgrid," *IEEE Transactions on Power Electronics,* vol. 26, pp. 689-701, 2011.

[41] N. B. Josep M. Guerrero, José Matas, Luis García de Vicuña, Jaume Miret, "Decentralized Control for Parallel Operation of Distributed Generation Inverters in Microgrids Using Resistive Output Impedance," *IEEE Industrial Electronics,* 2006.

[42] M. C. Wei Yao, José Matas, Josep M. Guerrero, Zhao-Ming Qian, "Design and Analysis of the Droop Control Method for Parallel Inverters Considering the Impact of the Complex Impedance on the Power Sharing," *IEEE Transactions on Industrial Electronics,* vol. 58, 2011.

[43] N. B. Josep M. Guerrero, Luis García de Vicuña, José Matas, Jaume Miret and Miguel Castilla, "Droop Control Method for the Parallel Operation of Online Uninterruptible Power Systems Using Resistive Output Impedance," presented at the Applied Power Electronics Conference and Exposition, 2006.

[44] A. S. T. Skjellnes, L. Norum, "Load Sharing for parallel inverters without communication," in *Nordic Workshop on power and industrial Electronics*, Sweden, 2002.

[45] N. Pogaku, M. Prodanovic, and T. C. Green, "Modeling, Analysis and Testing of Autonomous Operation of an Inverter-Based Microgrid," *IEEE Transactions on Power Electronics,* vol. 22, pp. 613-625, 2007.

[46] L. Corradini, P. Mattavelli, M. Corradin, and F. Polo, "Analysis of Parallel Operation of Uninterruptible Power Supplies Loaded through Long Wiring Cables," in *Twenty-Fourth Annual IEEE Applied Power Electronics Conference and Exposition*, 2009, pp. 1276-1282.

[47] X. Wang, F. Blaabjerg, Z. Chen, and W. Wu, "Resonance analysis in parallel voltage-controlled Distributed Generation inverters," in *Twenty-*

Eighth Annual IEEE Applied Power Electronics Conference and Exposition (APEC), 2013, pp. 2977-2983.

[48] P. F. S. R. M. Santos Filho, P. C. Cortizo, Guillaume Gateau, Ernane A. A. Coelho, "Power System Stabilizer for Comunicationless Parallel Connected Inverters," presented at the IEEE International Symposium on Industrial Electronics (ISIE), 2010, 2010.

[49] F. Luo, Y. Lai, C. K. Tse, and K. Loo, "A triple-droop control scheme for inverter-based microgrids," in *IECON 2012-38th IEEE Annual Conference on Industrial Electronics Society*, 2012, pp. 3368-3375.

[50] "IEEE Standard for Interconnecting Distributed Resources with Electric Power Systems, IEEE Standard 1547, p. 16.," 2003.

[51] P. Yunqing, J. Guibin, Y. Xu, and W. Zhaoan, "Auto-master-slave control technique of parallel inverters in distributed AC power systems and UPS," in *IEEE 35th Annual Conference of Power Electronics Specialists*, 2004, pp. 2050-2053.

[52] L. Woo Cheol, L. Taeck Ki, L. Sang Hoon, K. Kyung Hwan, H. Dong Seok, and S. In Young, "A master and slave control strategy for parallel operation of three-phase UPS systems with different ratings," in *the Nineteenth Annual IEEE Applied Power Electronics Conference and Exposition*, 2004, pp. 456-462 Vol.1.

[53] C. Yeong Jia and E. K. K. Sng, "A novel communication strategy for decentralized control of paralleled multi-inverter systems," *IEEE Transactions on Power Electronics,* vol. 21, pp. 148-156, 2006.

[54] T. Iwade, S. Komiyama, Y. Tanimura, M. Yamanaka, M. Sakane, and K. Hirachi, "A novel small-scale UPS using a parallel redundant operation

system," in *The 25th International Telecommunications Energy Conference* Japan, 2003, pp. 480-484.

[55] T. Jingtao, L. Hua, Z. Jun, and Y. Jianping, "A novel load sharing control technique for paralleled inverters," in *IEEE 34th Annual Power Electronics Specialist Conference*, 2003, pp. 1432-1437.

[56] W. Tsai-Fu, C. Yu-Kai, and H. Yong-Heh, "3C strategy for inverters in parallel operation achieving an equal current distribution," *IEEE Transactions on Industrial Electronics,* vol. 47, pp. 273-281, 2000.

[57] J. C. Vasquez, J. M. Guerrero, A. Luna, P. Rodríguez, and R. Teodorescu, "Adaptive droop control applied to voltage-source inverters operating in grid-connected and islanded modes," *IEEE Transactions on Industrial Electronics,* vol. 56, pp. 4088-4096, 2009.

[58] A. Tuladhar, H. Jin, T. Unger, and K. Mauch, "Control of parallel inverters in distributed AC power systems with consideration of line impedance effect," *IEEE Transactions on Industry Applications,* vol. 36, pp. 131-138, 2000.

[59] C.-C. C. C.-T. Lee, and P.-T. Cheng, "A New Droop Control Method for the Autonomous Operation of Distributed Energy Resource Interface Converters," in *Proc. of the 2010 IEEE Energy Conversion Congress and Exposition (ECCE)*, Sept. 2010, pp. 702 –709.

[60] A. Micallef, M. Apap, C. S. Staines, and J. M. Guerrero Zapata, "Secondary control for reactive power sharing and voltage amplitude restoration in droop-controlled islanded microgrids," in *3rd IEEE International Symposium on Power Electronics for Distributed Generation Systems (PEDG)*, 2012, pp. 492-498.

[61] Z. Qing-Chang, "Robust Droop Controller for Accurate Proportional Load Sharing Among Inverters Operated in Parallel," *IEEE Transactions on Industrial Electronics,* vol. 60, pp. 1281-1290, 2013.

[62] H. Jinwei and L. Yun Wei, "An Enhanced Microgrid Load Demand Sharing Strategy," *IEEE Transactions on Power Electronics,* vol. 27, pp. 3984-3995, 2012.

[63] H. Jinwei, L. Yun Wei, J. M. Guerrero, J. C. Vasquez, and F. Blaabjerg, "An islanding microgrid reactive power sharing scheme enhanced by programmed virtual impedances," in *3rd IEEE International Symposium on Power Electronics for Distributed Generation Systems (PEDG)*, 2012, pp. 229-235.

[64] H. Jinwei, L. Yun Wei, J. M. Guerrero, F. Blaabjerg, and J. C. Vasquez, "An Islanding Microgrid Power Sharing Approach Using Enhanced Virtual Impedance Control Scheme," *IEEE Transactions on Power Electronics,* vol. 28, pp. 5272-5282, 2013.

[65] M. A. Abusara, M. Jamil, and S. M. Sharkh, "Repetitive current control of an interleaved grid-connected inverter," in *IEEE International Symposium on Power Electronics for Distributed Generation Systems (PEDG), 2012 3rd*, 2012, pp. 558-563.

[66] G. Escobar, P. Mattavelli, A. M. Stankovic, A. A. Valdez, and J. Leyva-Ramos, "An adaptive control for UPS to compensate unbalance and harmonic distortion using a combined capacitor/load current sensing," *IEEE Transactions on Industrial Electronics* vol. 54, pp. 839-847, 2007.

[67] P. Mattavelli, "An improved deadbeat control for UPS using disturbance observers," *IEEE Transactions on Industrial Electronics,* vol. 52, pp. 206-212, 2005.

[68] R. Ortega, E. Figueres, G. Garcerá, C. L. Trujillo, and D. Velasco, "Control techniques for reduction of the total harmonic distortion in voltage applied to a single-phase inverter with nonlinear loads: Review," *Renewable and Sustainable Energy Reviews,* vol. 16, pp. 1754-1761, 2012.

[69] Semikron, "SKAI Module Datasheet."

[70] L. Yun Wei, "Control and Resonance Damping of Voltage-Source and Current-Source Converters With LC Filters," *IEEE Transactions on Industrial Electronics,* vol. 56, pp. 1511-1521, 2009.

[71] LEM, "Voltage transducer CV3-1000."

[72] LEM, "Current transducer LA 125-P/SP4."

[73] J. He, Y. W. Li, D. Bosnjak, and B. Harris, "Investigation and resonances damping of multiple PV inverters," in *Twenty-Seventh Annual IEEE Applied Power Electronics Conference and Exposition (APEC), 2012*, 2012, pp. 246-253.

[74] Y. R. Mohamed, H. H. Zeineldin, M. Salama, and R. Seethapathy, "Seamless formation and robust control of distributed generation microgrids via direct voltage control and optimized dynamic power sharing," *IEEE Transactions on Power Electronics,* vol. 27, pp. 1283-1294, Mar 2012.

[75] H. Tao, J. L. Duarte, and M. A. Hendrix, "Line-interactive UPS using a fuel cell as the primary source," *IEEE Transactions on Industrial Electronics,* vol. 55, pp. 3012-3021, Jul 2008.

[76] M. A. P. de Azpeitia, A. Fernández, D. G. Lamar, M. Rodriguez, and M. M. Hernando, "Simplified voltage-sag filler for line-interactive uninterruptible power supplies," *IEEE Transactions on Industrial Electronics,* vol. 55, pp. 3005-3011, Aug 2008.

[77] H. Kim, T. Yu, and S. Choi, "Indirect current control algorithm for utility interactive inverters in distributed generation systems," *IEEE Transactions on Power Electronics,* vol. 23, pp. 1342-1347, May 2008.

[78] S. V. Iyer, M. N. Belur, and M. C. Chandorkar, "A generalized computational method to determine stability of a multi-inverter microgrid," *Power Electronics, IEEE Transactions on,* vol. 25, pp. 2420-2432, 2010.

[79] M. Rasheduzzaman, J. Mueller, and J. Kimball, "An Accurate Small-Signal Model of Inverter-Dominated Islanded Microgrids Using dq Reference Frame," *IEEE Journal of Emerging and Selected Topics in Power Electronics,* 2014.

[80] W. Issa, M. Abusara, and S. Sharkh, "Control of Transient Power during Unintentional Islanding of Microgrids," *IEEE Transactions on Power Electronics,* vol. 30, pp. 4573 - 4584, 2014.

[81] B. M. Eid, N. A. Rahim, J. Selvaraj, and A. H. El Khateb, "Control Methods and Objectives for Electronically Coupled Distributed Energy Resources in Microgrids: A Review," *IEEE Systems Journal,* 2014.

[82] L. G. d. V. Josep M. Guerrero, José Matas, Miguel Castilla and Jaume Miret, "Output Impedance Design of Parallel-Connected UPS Inverters

With Wireless Load-Sharing Control," *IEEE TRANSACTIONS ON INDUSTRIAL ELECTRONICS,* vol. 52, AUGUST 2005.